REPUBLIQUE ALGERIENNE DEMOCRATIQUE ET POPULAIRE
MINISTERE DE L'ENSEIGNEMENT SUPERIEUR ET DE LA RECHERECHE SCIENTIFIQUE

Université Blida 1

Faculté de Technologie

Département d'Automatique et électrotechnique

THESE DE DOCTORAT

Spécialité : Energie Renouvelable

Power system stability enhancement considering the integration of renewable energy sources

Par

HATTABI Intissar

Devant le jury composé de

Nawal CHEGGAGA	Professeur, U.de Blida	Présidente
Messaoud BELAZOUG	MCA, U.de Blida	Examinateur
Karim SEBAA	Professeur, de l'Ecole polytechnique d'Alger	Examinateur
Rafik BRADAI	Professeur, U.de Blida	Directeur de thèse
Aissa KHELDOUN	Professeur, U. de Boumerdes	Co-Directeur de thèse

ملخص: الهدف الرئيسي من هذا الموضوع هو دراسة تحسين منظمات استقرار النظام الكهربائي (PSS)باستخدام خوارزميات ميتاهيرستية متقدمة لتعزيز التخميد والاستقرار في أنظمة الطاقة، وخاصة في ظل ظروف الأعطال الشديدة مثل الأعطال من النوع ثلاثي الطور إلى الأرض. يهدف البحث إلى تحسين الأداء الديناميكي لأنظمة الطاقة من خلال تحسين معلمات الـ PSS باستخدام خوارزمية "MPA"وخوارزمية "MDBO" المعدلة لتهدئة النظام. من خلال مقارنة فعالية هذه الخوارزميات في ضبط الـPSS ، يهدف البحث إلى تحقيق استقرار أفضل للنظام، وتحسين سرعة استعادة الأعطال، وتحسين الأداء العام للنظام، والذي يمكن التحقق من صحته من خلال المحاكاة واختبار الأجهزة في الحلقة.
كلمات مفتاحية :منظمات استقرار النظام الكهربائي(PSS) ,الخوارزميات الميتاهيرستية, التحسين, الاستقرار, اختبار الأجهزة في الحلقة.

Abstract:

The main objective of this topic is to study the optimization of Power System Stabilizers (PSS) using advanced metaheuristic algorithms to enhance the damping and stability of power systems, particularly under severe fault conditions such as three-phase-to-ground faults. The research aims to improve the dynamic performance of power systems by optimizing the parameters of PSS through the Marine Predator Algorithm (MPA) and the Modified Dung Beetle Optimizer (MDBO). By comparing the effectiveness of these algorithms in tuning PSS, the goal is to achieve better system stability, faster fault recovery, and improved overall system performance, which can be validated through simulations and hardware-in-the-loop testing.
Key words: Power System Stabilizers (PSS), Metaheuristic Algorithms, Optimization, Stability, Hardware-in-the-Loop Testing.

Résumé :

L'objectif principal de ce sujet est d'étudier l'optimisation des stabilisateurs de système de puissance (PSS) en utilisant des algorithmes métaheuristiques avancés pour améliorer l'amortissement et la stabilité des systèmes électriques, en particulier dans des conditions de défaut sévères telles que les défauts triphasés à la terre. La recherche vise à améliorer la performance dynamique des systèmes de puissance en optimisant les paramètres des PSS à l'aide de l'algorithme Marine Predator Algorithm (MPA) et du Modified Dung Beetle Optimizer (MDBO). En comparant l'efficacité de ces algorithmes dans le réglage des PSS, l'objectif est d'obtenir une meilleure stabilité du système, une récupération plus rapide après un défaut et une amélioration globale de la performance du système, ce qui peut être validé par des simulations et des tests en boucle matérielle.
Mots clés : Stabilisateurs de Système de Puissance (PSS), Algorithmes Métaheuristiques, Optimisation, Stabilité, Test en Boucle Matérielle.

Acknowledgment

Foremost, i would like to give my sincere gratitude to Allah Almighty for giving me ability, knowledge and strength to complete my doctoral research study. Without His continuous blessings, it would not be possible.

I would like to express my sincere and deepest appreciation to my advisor Pr. BRADAI Rafik and to my co-advisor Pr. KHELDOUN Aissa, for their help and continuous invaluable support, for their patience, and their infinite constructive guidance and advices. For their motivation and their belief in us and the final fruit we have been working on.

I also like to extent my heartfelt thanks to the members of the board of examiners for proofreading and examining my thesis.

My extended deep thanks to KHETTAB Soufian for his help during this work. Without mentioning my family and their unconditional love and support, my friends and their meaningful backup, and everyone who has believed in me.

Dedication

First of all , I would like to thank the person who never stopped to support me, to believe in me, to watch over my success from a very young age, to whom I owe what I became today, and what I will become in the future, my precious mother.

I dedicate this work

To my late father, whom I hope to be proud of me, may God welcomes him into his vast paradise.

To my brother KARIM, my confident, the person who always takes care of me, may god bless him.

To my sisters CHAYMA and NOOR who are always there for me.

To my fiancé, who has been my source of motivation and my unstoppable support through every challenge. Your patience, encouragement, and belief in me have been a push during difficult times. I am forever thankful for your steadfast presence. You have been my greatest ally, and I am truly blessed to have you by my side.

To my best friend Aya who never stopped believing in me.

Table of contents

Table of content

List of figures

List of figures

List of tables

List of tables

List of symbols and acronyms

List of symbols and acronyms

A: state or plant matrix of size n×n

AVOA: African Vulture Optimization Algorithm

B: control or input matrix of size n×r

C: output matrix of size m×n / line-to-neutral capacitance per km (contexte différent)

D: (feed forward) matrix, size m×r

DBO: Dung Beetle Optimization

EO: Equilibrium Optimizer

E_{fd}: the field voltage input (from the exciter)

FOPID: Fractional Order PID

FOFPID: Fractional Order fuzzy PID

FO-TSF-PID: Fractional Order Takagi-Sugeno Fuzzy-proportional–integral–derivative

FPA: Flower Pollination Algorithm

GOOSE: GOOSE-inspired Optimization Algorithm

H: inertia constant in sec

HIL: Hardware-in-the-Loop

I_d, I_q, I_0: stator currents in dq0 reference

I_r: current at the receiving end

I_s: current at the sending end

K_A: Regulator gain in pu

K_E: Exciter constant related to self-excited field in pu

K_f: Feedback gain in pu

K_E, K_d: fuzzy input scaling factors

K_{PD}, K_{PI}: fuzzy output scaling factors

K_D: proportional gain

K_I: integral gain

K_t: differential tilt gain

K_{tg}: shaft stiffness of the drive train

H: generator inertia

λ, μ: Fractional order of derivation and integration

L: line inductance per km

l: line length in km

LFO: Low Frequency Oscillation

MPA: Marine Predator Algorithm

MDBO: Modified Dung Beetle Optimization

N: number of eigenvalues

P_f: Participation Factor

PID: Proportional-Integral-Derivative

Pmech: mechanical power input from turbine/governor

PSO: Particle Swarm Optimization

PSS: Power System Stabilizer

R_s: armature resistance in pu

S_E: Exciter saturation function

SMIB: Single Machine Infinite Bus

S_v: state variable

σ_i: real part/damping factor of the ith eigenvalue

T_A: Regulator time constant in sec

T'_{d0}: d-axis open circuit transient time constant

T''_{d0}: d-axis open circuit sub-transient time constant

T'_{q0}: q-axis open circuit transient time constant

T''_{q0}: q-axis open circuit sub-transient time constant

T_E: Exciter time constant

T_F: Feedback time constant

TID: Tilt-Integral-Derivation

T_R: Filter time constant

u: input vector of dimension r

V_R: Regulator output voltage

V_{Rmax}: Maximum voltage regulator output in pu

V_{Rmin}: Minimum voltage regulator output in pu

V_s: voltage at the sending end

V_r: voltage at the receiving end

V_T: Generator terminal voltage

V_{dterm}, V_{qterm}, $V0_{term}$: stator voltages in dq0 reference

WHO: Wild Horse Optimization Algorithm

ω : generator rotor speed

ω_b: electrical base speed

ω_s: synchronous speed ($2\pi f$)

WOA: Whale Optimization Algorithm

WSCC: Western System Coordinating Council

x(1)...x(5): centers and widths of triangular membership functions

X_d, X_q: synchronous reactances

X'_d, X'_q: transient reactances

X''_d, X''_q:: sub-transient reactances

ζ_i: damping ratio of the ith eigenvalue

ψ_d, ψ_q, ψ_0: stator flux in dq0 reference

ψ'_d,ψ'_q: rotor flux in dq0 reference

ZOA: Zebra Optimization Algorithm

Δx: state vector of dimension n

Δy: output vector of dimension m

Δu: input vector of dimension r

$\Delta\omega$: speed deviation

$\Delta\dot{\omega}$: acceleration

T: torque

θ_{tg}: generator shaft angle twist

C_{tg}: damping coefficient of the drive train

General introduction

General introduction

In recent times, power systems have become more sophisticated due to the complexity and nonlinearity of their components. These systems encompass various elements, such as generating units, distribution and transmission lines, protective devices, transformers, and diverse loads. This complexity has rendered power systems more susceptible to a range of disturbances, including faults, load variations, lightning strikes, equipment failures, and the activation of protective devices. The electrical power output from the generator varies rapidly with the slowly varying mechanical input. With the mechanical input changing slowly, the generator produces different amounts of electrical power output. The change in shaft torque, which results in low-frequency oscillations (LFOs) in the range of 0.2–3 Hz, is caused by the imbalance between the generator's input and output powers[1].These electromechanical oscillations are of two types: local mode for 1– 3Hz or interarea mode in the range of less than 1 Hz. The LFOs are undesirable and must be damped out as quickly as possible to guarantee system stability and efficiency. The lead-lag phase compensation structure of the conventional power system stabilizer (CPSS) is employed to dampen out such oscillations in multimachine power systems (MMPS) and single machine infinite bus (SMIB) systems [2],[1].

According to the literature, Conventional PSSs (CPSS with fixed parameters) have been widely used because of their ease of use and good performance, as efficient damping controllers in power systems [2,3]. However, CPSS rely on the linearized theory of control systems. However, this approach is primarily effective in mitigating LFOs for a specific operating point. Unfortunately, the large variety of operating conditions found in non-linear power systems presents challenges for CPSS designs. Root-locus [4], frequency response [5], digital control[6], pole-placement [7], and non-linear & adaptive control methods [8], [9] are examples of classical control techniques that work well when applied to non-differentiable and non-convex problem functions, but they are not appropriate for solving them.
Different types of PSSs have been designed for their simplicity, and examples of such designs and other controllers are introduced in first chapter.

The performance of controllers is directly influenced by their parameters, and the dynamic flexibility of the controller is affected by the values of these parameters. Their exact

response is hard to detect and, in certain cases, even impossible to find using conventional mathematical methods. Meta-heuristic algorithms are used to determine the optimal or nearly optimal parameters in certain scenarios.

According to the literature, numerous research papers have investigated the application of metaheuristic algorithms for the optimal lead-lag-based PSS tuning recently. In fact numerous different metaheuristic algorithms are used like, particle swarm optimization[5]–[6] genetic algorithms,[7] -[8], Jaya algorithm,[10], gray wolf optimizer[11], bat algorithm[12], farmland fertility algorithm[13], African Vultures Optimization Algorithm[14], Salp swarm algorithm,[15] , kidney-inspired algorithm[16], whale optimization algorithm[17], cuckoo search,[18], Henry gas solubility optimization[19], collective decision optimization algorithm,[20], and slime mold algorithm[21].

A robust Power System Stabilizer (PSS) necessitates a precise design and a multitude of test scenarios for its robustness to be assured and validated. The performance of the PSS has been examined by researchers through a range of test cases and different system architectures. In the study referenced as[22], a disturbance condition was simulated by introducing a 5% step change in mechanical power across a multi-machine power system (MMPS). Various loading conditions were explored, with an increasing step load within the MMPS as described in[4],The impact of a three-phase fault was examined in [23], where the fault persisted for 0.1 seconds in a SMIB power system. A 100 ms 3-phase to ground fault was investigated using the MMPS model in[24].

Several performance indices were used in a comprehensive evaluation of the stability of improved Power System Stabilizers (PSSs) within electrical power systems, each associated with distinct objective functions to enhance the optimization process. Specifically, the Inverse Time Absolute Square of the Error (ITAE) was utilized as an objective function in[25]. Additionally, in [26], the Integral of Squared Error (ISE) and Integral of Time-weighted Squared Error (ITSE) were introduced as cost functions. On the other hand, a frequency domain cost function known as the D-shape cost function was proposed in [4] [13] to shift eigenvalues towards the left side of the complex plane. The robustness of the developed method was assessed using performance metrics such as damping ratio, overshoot, settling time, and eigenvalues.

In recent times, researchers have leveraged modern technologies and methodologies to assess the robustness of their PSS. Among the prevalent techniques are Rapid Control

Prototyping (RCP), Hardware-in-the-Loop (HIL), and Software-in-the-Loop (SIL) . As electrical power networks have grown increasingly complex over the past few decades, there has been a corresponding evolution in verification methodologies and related test tools. Compared to older techniques, real-time technology now offers benefits like faster operations, higher computation powers, high-speed processing, and improved performance. Because experimental study is more tractable and reproducible than simulation results, HIL-based verification approach enables researchers to employ it to test their developed PSS model[27].

To guarantee the stability of power systems, this study focuses on small-signal stability analysis. Different benchmark power systems were utilized to achieve this goal. The research involves the use of Power System Stabilizers (PSS) and other controllers, including both conventional and proposed topologies, aimed at damping low-frequency oscillations. The tuning of these controllers' parameters was carried out using both existing and modified metaheuristic algorithms. To ensure practical applicability, the study was validated through hardware-in-the-loop (HIL) simulations, allowing for real-world verification of the proposed methods and demonstrating their effectiveness in enhancing system stability under various operating conditions.

This thesis is organized into five chapters; they are summarized as follows:

The first chapter is dedicated to an overview of the Electrical power system by citing its different structures then, the power system stability is introduced and its main classifications are presented. The chapter is concluded with an overview of Metaheuristic algorithm.

The second chapter is devoted to the Dynamic modeling of power system. A detailed modeling of synchronous generator, excitation system, loads, transmission line, power system stabilizer and the double fed induction motor is presented.

In the third chapter, an optimization of Power System Stabilizer (PSS) Using the Marine Predator Algorithm (MPA) in Conventional Power Systems is developed. The chapter is started by presenting system tests then the problem optimization, the proposed algorithm and the fitness function used in this study. After that, the simulation results are introduced by interpreting stability analysis in time domain & frequency domain where the performance of proposed strategy is evaluated. This chapter is concluded with a Hardware in the loop of the proposed controller.

The last chapter of this thesis is dedicated to the analysis and the simulation of the stability of power system when the integration of renewable energy into power system is taken on consideration.

The general conclusion concerns a brief synthesis of the work carried out with the main obtained results and some perspectives.

Chapter one

State of the art of power system stability & tuning PSS using metaheuristic algorithms

CHAPTER ONE

I.1 Introduction

Power system stability is essential for maintaining reliable operation under various disturbances. It is generally categorized into rotor angle, voltage, and frequency stability, each influencing system performance and security. Among these, low-frequency oscillations pose a significant challenge, requiring effective damping strategies.

Traditional power system stabilizers (PSS) have been widely used but face limitations under dynamic conditions. To address these challenges, advanced controllers—such as fractional-order, fuzzy logic, and hybrid approaches—have been explored. Additionally, metaheuristic optimization techniques have gained attention for enhancing controller performance, offering adaptive solutions for stability improvement

This chapter reviews key developments in power system stability, highlighting the evolution of control strategies and optimization techniques aimed at improving system resilience and performance.

I.2 State of the art of Power system stability

Power system stability is broadly defined as the ability of a power system to remain in a state of operating equilibrium under normal conditions and to return to an acceptable equilibrium state after being subjected to a disturbance.

Instability in a power system can manifest in various ways, depending on the configuration and operating mode of the system. Traditionally, stability issues have primarily focused on maintaining synchronous operation. Since power systems rely heavily on synchronous machines for electricity generation, a key condition for stable operation is that all synchronous machines remain synchronized—or "in step." This aspect of stability is influenced by the dynamics of generator rotor angles and power-angle relationships.

However, instability can also occur without the loss of synchronism. For instance, in a system where a synchronous generator feeds an induction motor load through a transmission line, instability may arise due to load voltage collapse. In such cases, the concern shifts from

maintaining synchronism to ensuring voltage stability and control. This type of instability is particularly relevant for large systems supplying extensive areas with distributed loads.

In stability evaluations, the focus is on the behavior of the power system when subjected to transient disturbances. These disturbances can range from small, continuous load changes to large, severe events such as short circuits, loss of major generators, or subsystem disconnections. For the system to function properly, it must handle these disturbances while maintaining a reliable energy supply. System responses to disturbances involve numerous components, including:

- Protective relays, which isolate faults and mitigate further damage.
- Voltage regulators, which adjust voltage variations across generators and transmission systems.
- Prime mover governors, which control speed variations in the system.
- Generation control systems, which respond to tie-line loading changes.

Changes in system voltage and frequency can also impact loads, which respond differently depending on their characteristics. Protective devices used for specific equipment may react to variations in system variables, thereby affecting overall system performance.

Given the complexity of these interactions, stability analyses often make assumptions to simplify the problem, focusing on factors most relevant to the specific type of stability being studied. This approach allows for a clearer understanding and classification of stability issues across various categories.

I.2.1 Classification of power system stability

The suggested power system stability categorization is based on the following considerations:

- The physical nature of the resulting instability [28].
- The size of the disturbance considered [28].

- The devices, processes, and time span that must be taken into consideration in order to determine stability [28].

- The most appropriate method of calculation and prediction of stability [28].

The diagram in **Figure I.1** depicts the overall picture of the power system stability problem, identifying its categories and subcategories. The descriptions of the corresponding forms of stability phenomena are as follows.

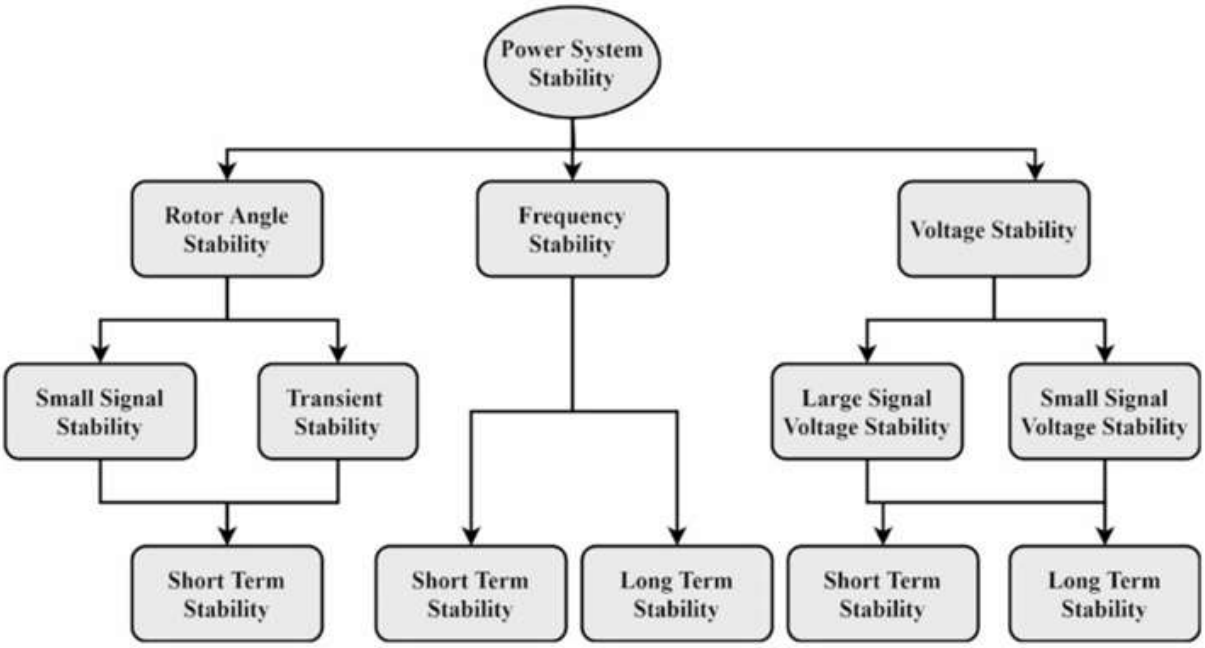

Figure I-1: Classification of power system stability [28].

Perturbations in the power system can be categorized into two types: small-signal stability and transient stability. While small signal stability deals with deviations (whose magnitude is small and with a longer duration), transient stability deals with large disturbances sustaining for a shorter duration. On the other hand, if the physical quantity that alters during instability is considered, power system stability is broadly classified into three types: voltage stability; Frequency stability, and; Rotor angle stability [29].

During heavily loaded conditions of long transmission lines, the reactive power consumption increases manifolds [30]. Hence, the voltage profile of that transmission lines is not maintained within predefined limits. This can be demarcated by observing a gradual decrease in the receiving end voltage over a prolonged period, followed by an accelerated

descend in the voltage profile [31]. It can ultimately lead to a complete blackout of the power system grid. There is a similar challenge to maintaining the frequency of the complete power system within specified limits, i.e., to maintain the overall synchronism of the power system.

This stability issue occurs mainly due to an imbalance between supply and demand [32]. The frequency instability will generate fluctuations in the receiving end voltage due to partially destructive interference between voltages of different frequencies due to the use of renewable energies [32]. Similarly, rotor angle stability is caused by large disturbances, e.g., outage of tie lines, large load fluctuations, loss of generating units, etc. [33] This may lead to machines falling out of synchronism, i.e., frequency instability, and, finally, the collapse of synchronous machines. This will lead to a steep decrease in voltage and voltage instability. One of the aspects of rotor angle instability is the low-frequency oscillations, caused by small disturbances and, therefore, challenging the small-signal stability of the power system. These oscillations are small in magnitude and remain undetected by the traditional monitoring and controlling devices. They keep growing in magnitude, and being, in some cases, not possible to bring back the system to the normal operating conditions.

I.2.2 Synchronization and Damping: Key Factors in Power System Stability

Several power system controllers have been proposed to deal with these problems of instability. They employ methods for optimal tuning of their parameters to obtain maximum efficiency with the controllers [34],[35]. Various protecting devices are available to avoid large perturbations, but small ones can be undetected and lead to LFO.

LFOs are caused mainly due to lack of fine adjustment of AVRs to control oscillations, electrical load dependency on frequency, negative interaction of controllers, and characteristics of the network. These factors mainly depend upon the ability of the power system in maintaining equilibrium between mechanical and electromagnetic torques for individual alternators. Following a perturbation, deviation in electromagnetic torque can be solved into synchronizing and damping torques according to equation,

$$\Delta \mathrm{Te} = T_S \Delta\delta + T_D \, \Delta S_m \qquad \text{(I. 1)}$$

where, ΔTe is the change in the electromagnetic torque, T_S is the synchronizing torque coefficient, T_D is the damping torque coefficient, Δδ is the deviation in the rotor angle, $\Delta S_m$is the deviation in the synchronous speed, $T_S\Delta\delta$ is the synchronizing torque component, $T_D \, \Delta S_m$ is the damping torque component.

Figure I. 2 shows the synchronizing torque is in the direction of deviation in rotor angle, whereas the damping torque component lies in the direction of deviation in synchronizing torque.

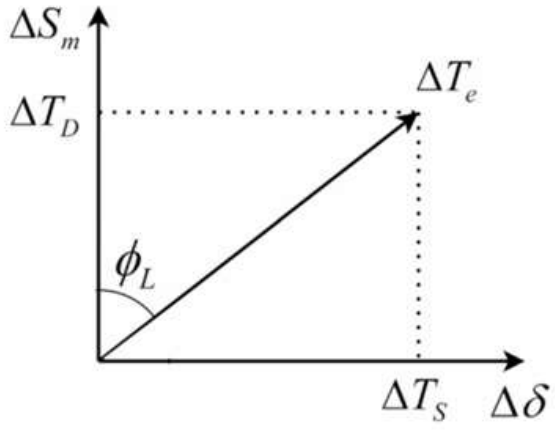

Figure I-2: Synchronizing and Damping Torques[36]

If either, or both, of these quantities, is negative, then the system is unstable because the negative synchronizing torque creates 'aperiodic' non-oscillatory instability, whereas negative damping torque creates LFOs [37]. There is a balance between mechanical torque and electromagnetic torque of any synchronous machine in operating at equilibrium conditions. Nowadays, the electromagnetic torque varies due to uncertain variations in operating conditions. It can be resolved into two components after a perturbation: the synchronizing torque, and the damping torque. Synchronizing torque helps in maintaining synchronism followed by a disturbance, whose deficiency can lead to non-oscillatory instability, whereas lack of damping torque leads to LFO Depending upon the location of oscillations, LFO can be classified as [1]; local mode for 1– 3Hz and interarea mode in the range of less than 1 Hz..

According to the literature, Conventional PSSs (CPSS with fixed parameters) have been widely used because of their ease of use and good performance, as efficient damping controllers in power systems [2],[3]. However, CPSS rely on the linearized theory of control systems. However, this approach is primarily effective in mitigating LFOs for a specific operating point. [2] established the relationship of damping capability of the power system and stability of synchronous generator during small perturbations with its field excitation. A PSS was

designed to control the field excitation of a synchronous generator by providing a supplementary feedback signal that stabilizes the system [39];[40].

I.2.3 Progressions in Power System Stabilizer

The PSS is the most employed controller in power systems, created in 1967 [41]. Studies had established the relation between the damping capacity and the alternator excitation system. Since then, many improvements have been made according to its design, there is a different version of PSS as compared to the conventional PSS (CPSS). The basic model (block diagram) of a PSS is shown in **Figure I.3** According to this diagram, a PSS works on the feedback mechanism, where the angular velocity of the rotor of the alternator is taken as an input signal of PSS. Based on this deviation, an appropriate signal is generated as output and given as the excitation control signal to adjust the excitation to damp out the oscillations.

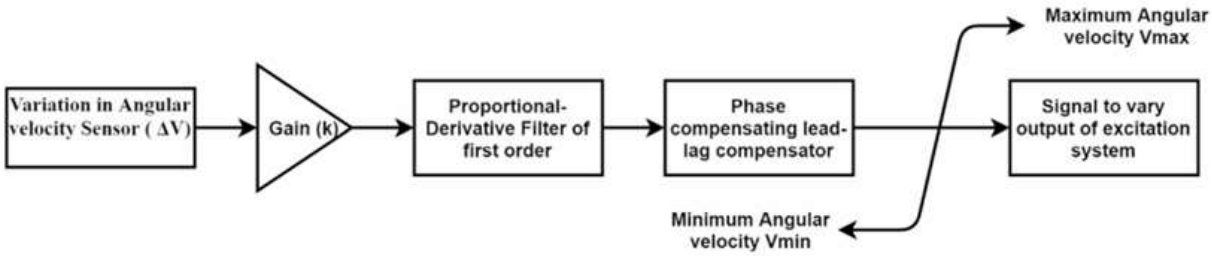

Figure I-3: Bloc diagram of CPSS

In addition to conventional PSS designs, the IEEE standard PSS2B stabilizer offers an alternative approach to improving power system stability. Unlike traditional PSS, which relies solely on rotor speed deviations, the PSS2B utilizes two input signals—angular velocity deviations ($\Delta\omega$) and generator active power (Pe). This stabilizer enhances damping performance by incorporating a transformer at the input stage and employing components such as a sensor, washout filter, gain, and output limiter. The block diagram of PSS2B is shown in Figure I.4, while Figure I.5 illustrates its input transformer.

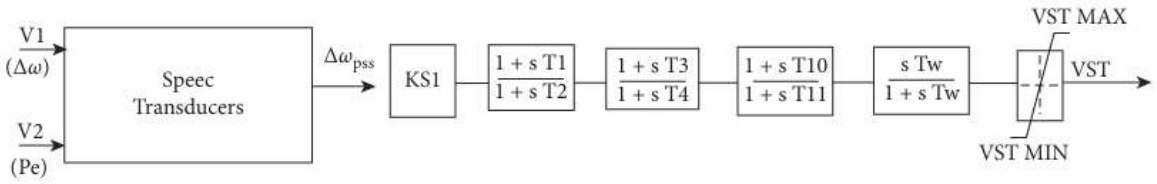

Figure I-4: Block diagram of a PSS2B

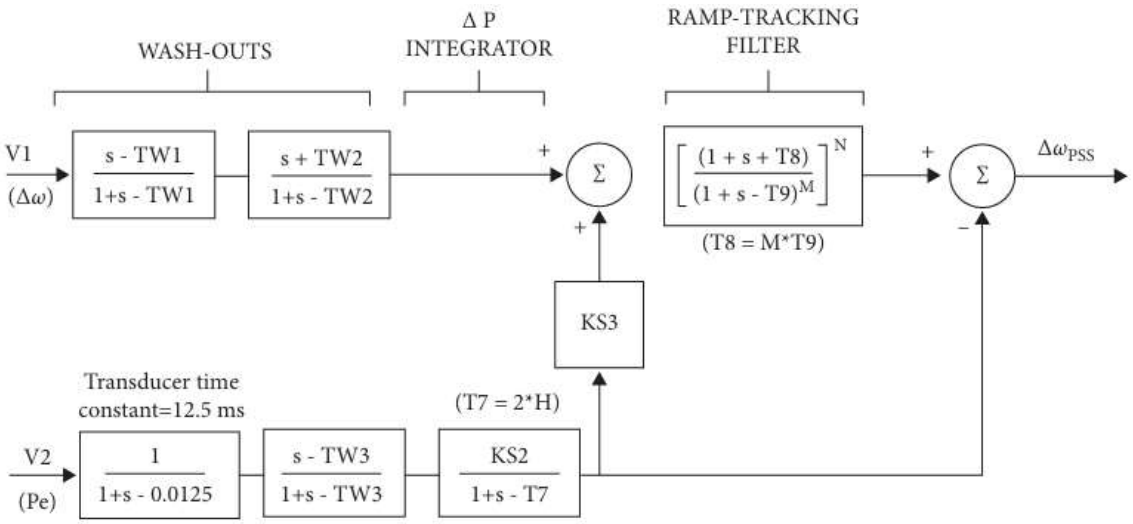

Figure I-5: Block diagram of speed transformer of PSS2B stabilizer[33].

Nonetheless, previous studies have demonstrated that the CPSS's effectiveness deteriorates during continuous and large disturbances [1],[4]. PSSs based on proportional integral derivatives (PIDs) have also been used to improve stability in power system [10],[11] due to their simple structure and fewer parameters. Because fractional order controllers offer greater freedom and flexibility than traditional proportional integral (PI) or PID controllers, researchers have also employed them for power system stability studies[12], [13] and [14]. However, due to the trial-and-error techniques used to choose and adjust their gain parameters, the PID/fractional order PID (FOPID) controllers might not offer the required performance under changing operating conditions. Thus, fuzzy logic control-based approaches have been suggested to improve the power system's dynamic stability[15]. To improve the transient stability in a SMIB power system, a hybrid of fuzzy logic type 2 based PSS and the FOPID controller has been proposed in [16].

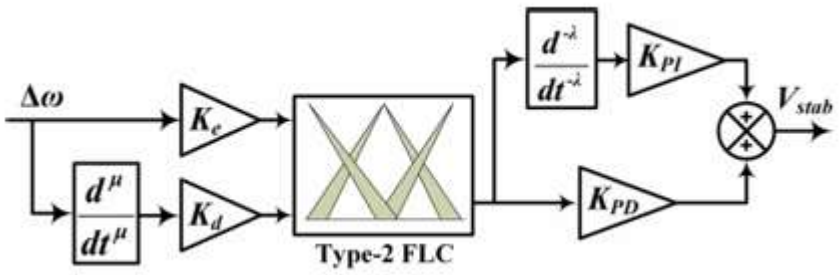

Figure I-6: Block diagram of hybrid of fuzzy logic type 2 based PSS and the FOPID controller[5].

It can be concluded that there is a great evolution of the concept of designing PSS. The research works of many authors have been produced in a timeline way.

I.3 PSS Controller Parameter Tuning using Metaheuristic Algorithms

The performance of devices is directly dependent upon their parameters, and its dynamic response would be affected by the values of these parameters. They are complex, given by dynamic and nonlinear state equations, finding their exact solution is complicated and, in some cases, not even possible by using classical mathematical methods. In these cases, meta-heuristic algorithms are being used for finding the optimal, or close to the optimal, parameter. They became successful in one condition, but they fail in others. [39] utilized Particle Swarm Optimization (PSO) technique to find optimal values of parameters of PSS, using eigenvalues analysis in three-machine nine-bus and 10-machine 39-bus (New England) systems for damping low-frequency oscillations. This was also of decentralized nature, i.e., based on local measurements. The designed con troller could work well over a wide range of operating conditions and system configurations. The novel Orthogonal Learning Artificial Bee Colony (OLABC) algorithm-based PSS was studied by [42]. The selected test system was SMIB, where the performance was measured through performance indices IAE, ITAE, ISE and ITSE for light, normal and heavy loading conditions. The results obtained were better than Artificial Bee Colony PSS (ABCPSS) having less overshoot and short settling time, that was tested on SMIB system with IEE DC1 exciter. In comparison to PSO-PI-PSS and PSO-PID-PSS, a better damping ratio was obtained by using ISE as a performance index. [34] proposed an FOPID-PSS and evaluated its robustness on a Single Machine Infinite Bus (SMIB) system under different disturbances and operating conditions. The study compared the performance of FOPID-PSS with conventional PID-PSS and PSS controllers. Furthermore, the proposed FOPID-PSS, optimized using the Bat Algorithm (BA), was compared with a Firefly Algorithm (FFA)-based FOPID-PSS. Simulation results demonstrated the effectiveness of BA in tuning FOPID-PSS, achieving superior robustness and improved power system stability across different scenarios. [5] proposed a hybrid Firefly Algorithm-Particle Swarm Optimization (FAPSO) approach for tuning an Interval Type-2 Fractional Order Fuzzy PID (IT2FOFPID)-based power system stabilizer (PSS) to mitigate low-frequency oscillations. The IT2FOFPID-PSS was designed using speed deviation and acceleration as input signals. To evaluate its effectiveness, simulations were conducted on both a Single Machine Infinite Bus (SMIB) system and the New England 10-machine 39-bus system, demonstrating improved damping performance compared to conventional methods.

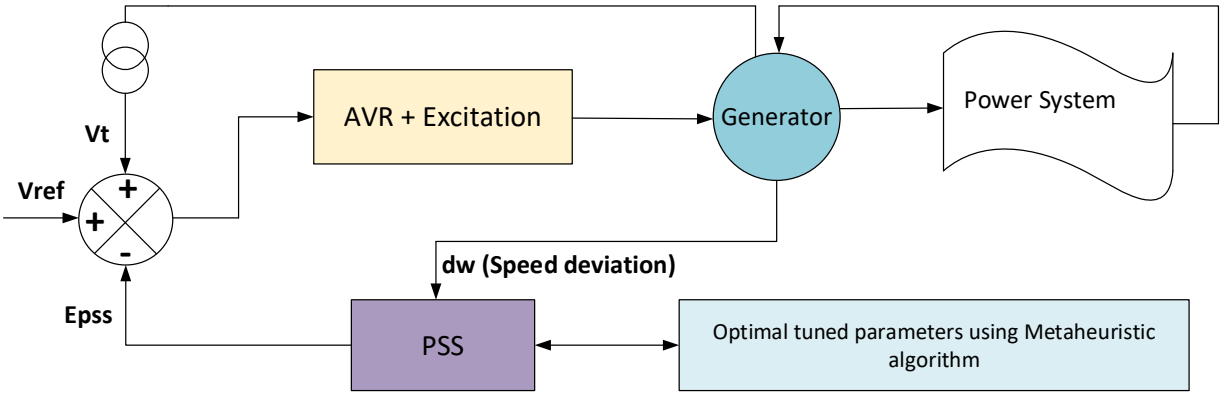

Figure I-7: Block Diagram of optimal tuned Power system stabilizer in power system

I.4 Conclusion

The continuous evolution of power systems necessitates robust and adaptive control strategies to ensure stability under various operating conditions. While conventional stabilizers remain widely used, their performance can be improved through advanced control techniques such as fractional-order, fuzzy logic, and hybrid approaches.

Metaheuristic optimization has emerged as a powerful tool for tuning these controllers, offering flexibility and improved dynamic response. Despite significant advancements, challenges remain in developing more efficient, scalable, and real-time applicable solutions. Future research should focus on integrating these techniques with modern power grids, considering the growing penetration of renewable energy sources and the need for enhanced resilience.

Chapter two

Dynamic Modelling of Power System

CHAPTER TWO

II.1 Introduction

Dynamic modeling is a fundamental step in analyzing and understanding the behavior of power systems under varying conditions. This chapter delves into the mathematical representation of key components of the power system, enabling the study of their interactions and dynamic responses. The synchronous generator, as the backbone of power generation, is modeled in detail, along with its excitation system that governs voltage regulation. Additionally, the dynamic behavior of loads, transmission lines, power system stabilizers, and the double-fed induction motor is examined, highlighting their roles in maintaining system stability and performance. These models serve as the foundation for advanced analysis and controller design.

II.2 Generator's model

The synchronous generators are the main source of the electrical energy in power systems. They are at the heart of any power system, therefor, a necessary condition for a system to operate properly is that all synchronous machines remain in synchronism (in step) [1].

Synchronous generator consists of two parts rotor and stator. The rotor part consists of field windings and stator part consists of armature conductors. The field winding is excited by direct current. The rotation of field poles in the presence of armature conductors induces an alternating voltage which results in electrical power generation [43]. The frequency of the stator electrical quantities is thus synchronized with the rotor mechanical speed: hence the designation "synchronous machine". [1]

As shown in Fig II.1, the armature windings which are located on stator, are the three phase windings (a, b, c) which are distributed 120° apart in space so that, with uniform rotation of the magnetic field, voltages displaced by 120° in time phase will be produced in the windings [1]. Whereas, the four windings on the rotor are:

- The field winding connected to the exciter (fd).

- The d-axis damper (1d):

  d: direct axis, which is a spinning axis directly in line with the "north pole" of the field winding.

- Two q-axis dampers (1q, 2q):

  q: quadrature axis, which is a spinning axis 90 degrees out of phase with the d-axis.

The damper windings (d and q axis dampers); also called amortisseur windings, are extra windings that provide start-up torque and damping for the machine, they also create a force that attempt to bring the machine to 60Hz or 50 Hz [36]. Some conventions are made in order to proceed the modeling are: q-axis leads the d-axis and the rotor angle θshaft is the angle between phase a axis and q-axis and all equations will be written for a p-pole machine (because different sources make different conventions). The equations of the model presented in this chapter are quoted from [43].

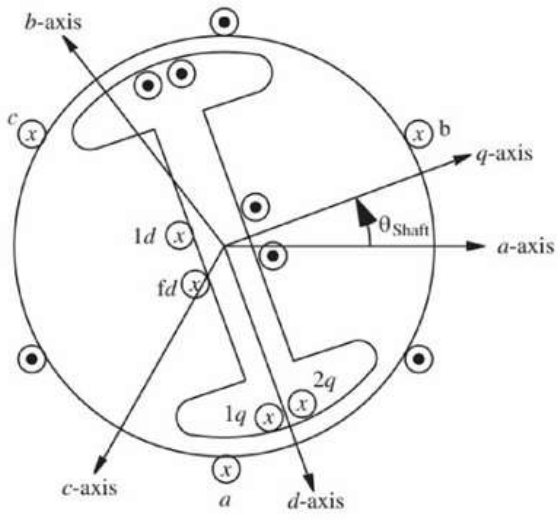

Figure II-1: Synchronous generator schematic[43]

Application of fundamental Kirchhoff's, Faraday's and Newton's laws give the following equations for the stator, the rotor, and the shaft:

Stator:	Rotor:	Shaft:
$v_a = i_a r_s + \frac{d\lambda_a}{dt}$ $(II.1)$	$v_{fd} = i_{fd} r_{fd} + \frac{d\lambda_{fd}}{dt}$ $(II.4)$	$\frac{d\theta_{shaft}}{dt} = \frac{2}{p} w$ $(II.8)$
	$v_{1d} = i_{1d} r_{1d} + \frac{d\lambda_{1d}}{dt}$ $(II.5)$	$J\frac{2}{p}\frac{dw}{dt} = T_m - T_e - T_{fw}$ $(II.9)$
$v_b = i_b r_s + \frac{d\lambda_b}{dt}$ $(II.2)$	$v_{1q} = i_{1q} r_{1q} + \frac{d\lambda_{1q}}{dt}$ $(II.6)$	
$v_c = i_c r_s + \frac{d\lambda_c}{dt}$ $(II.3)$	$v_{2q} = i_{2q} r_{2q} + \frac{d\lambda_{2q}}{dt}$ $(II.7)$	

Where λ is flux linkage, r is winding resistance, J is the inertia constant, P is the number of magnetic poles per phase, T_m is the mechanical torque applied to the shaft, T_e is the torque of electrical origin, and T_{fw} is a friction-windage torque.

Special transformations are done to transform the *abc* phase quantities into another reference frame Called the *dq0* transformation. The transformation is very similar to that of symmetrical components when dealing with fault analysis [9].

$$V_{dq0} = \begin{bmatrix} V_d \\ V_q \\ V_0 \end{bmatrix} = T_{dq0}\, V_{abc} = T_{dq0} \begin{bmatrix} V_a \\ V_b \\ V_c \end{bmatrix} \qquad (II.10)$$

$$V_{abc} = \begin{bmatrix} V_a \\ V_b \\ V_c \end{bmatrix} = T_{dq0}^{-1}\, V_{dq0} = T_{dq0}^{-1} \begin{bmatrix} V_d \\ V_q \\ V_0 \end{bmatrix} \qquad (II.11)$$

The same is applied for the current i and for the flux.

The matrix Tdq0 defined as:

$$T_{dq0} \triangleq \frac{2}{3} \begin{bmatrix} \sin\left(\frac{P}{2}\,\theta_{shaft}\right) & \sin\left(\frac{P}{2}\,\theta_{shaft} - \frac{2\pi}{3}\right) & \sin\left(\frac{P}{2}\,\theta_{shaft} + \frac{2\pi}{3}\right) \\ \cos\left(\frac{P}{2}\,\theta_{shaft}\right) & \cos\left(\frac{P}{2}\,\theta_{shaft} - \frac{2\pi}{3}\right) & \cos\left(\frac{P}{2}\,\theta_{shaft} + \frac{2\pi}{3}\right) \\ \frac{1}{2} & \frac{1}{2} & \frac{1}{2} \end{bmatrix} \qquad (II.12)$$

The inverse T_{dq0}^{-1} is then calculated:

$$T_{dq0}^{-1} = \begin{bmatrix} \sin(\frac{P}{2}\theta_{shaft}) & \cos(\frac{P}{2}\theta_{shaft}) & 1 \\ \sin(\frac{P}{2}\theta_{shaft} - \frac{2\pi}{3}) & \cos(\frac{P}{2}\theta_{shaft} - \frac{2\pi}{3}) & 1 \\ \sin(\frac{P}{2}\theta_{shaft} + \frac{2\pi}{3}) & \cos(\frac{P}{2}\theta_{shaft} + \frac{2\pi}{3}) & 1 \end{bmatrix} \quad (II.13)$$

After evaluation, the system in dq0 coordinates has the form

Stator:

$$v_d = r_s i_d - w\lambda_q + \frac{d\lambda_d}{dt} \quad (II.14)$$

$$v_q = r_s i_q + w\lambda_q + \frac{d\lambda_q}{dt} \quad (II.15)$$

$$v_0 = r_s i_0 + \frac{d\lambda_0}{dt} \quad (II.16)$$

Rotor:

$$v_{fd} = r_{fd} i_{fd} + \frac{d\lambda_{fd}}{dt} \quad (II.17)$$

$$v_{1d} = r_{1d} i_{1d} + \frac{d\lambda_{1d}}{dt} \quad (II.18)$$

$$v_{1q} = r_{1q} i_{1q} + \frac{d\lambda_{1q}}{dt} \quad (II.19)$$

$$v_{2q} = r_{2q} i_{2q} + \frac{d\lambda_{2q}}{dt} \quad (II.20)$$

Shaft:

$$\frac{d\theta_{shaft}}{dt} = \frac{2}{p} w \quad (II.21)$$

$$J\frac{2}{p}\frac{dw}{dt} = T_m - T_e - T_{fw} \quad (II.22)$$

The expression of T_e is derived after considering the overall energy or power balance for the machine. This is an electromechanical system that can be divided into an electrical system, a mechanical system, and a coupling field [43]. Figure II-2 shows a diagram for such power balance for a single machine.

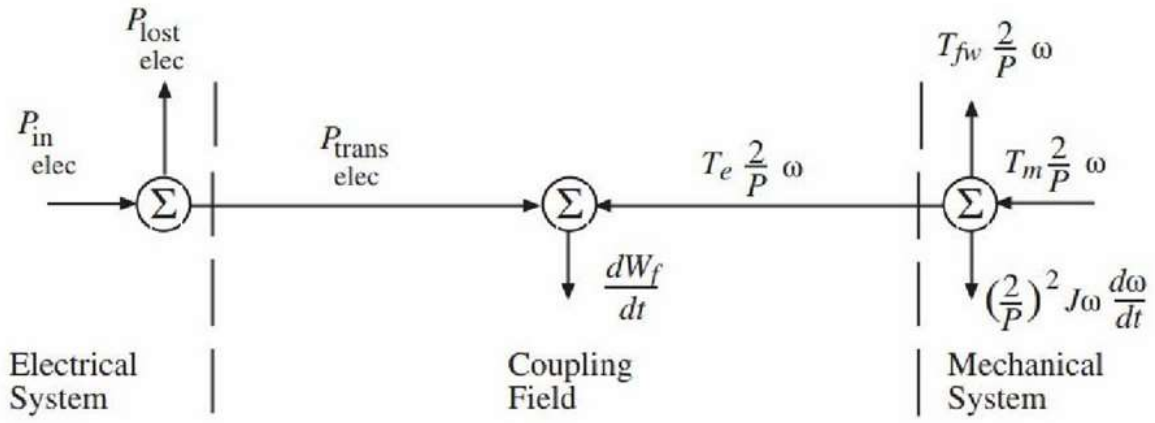

Figure II-2: Synchronous machine power balance[43]

The expression of electrical torque $T_e$is derived after considering that the electrical system losses are in the form of resistance and the mechanical system losses are in the form of friction. The coupling field is assumed to be lossless, hence the movement of energy between the electrical and mechanical systems can be tracked easily[36].

$$T_{elec} = -\frac{3}{2}\frac{P}{2}\left(\lambda_d I_q - \lambda_q I_d\right) \qquad (II.23)$$

To complete the dynamic model in the transformed variables it desirable to define an angle that is constant for constant shaft speed. It is defined as follows [10]:

$$\delta \triangleq \frac{P}{2}\theta_{shaft} - w_s t \qquad (II.24)$$

where w_s is a constant normally called rated synchronous speed in electrical radians per second, giving:

$$\frac{d\delta}{dt} = \omega - \omega_s \qquad (II.25)$$

$$J\frac{2}{P}\frac{dw}{dt} = T_m + \frac{3}{2}\frac{P}{2}\left(\lambda_d i_q - \lambda_q i_d\right) - T_{f\omega} \qquad (II.26)$$

The model of the per-unitized equations is presented as follows (keeping in mind that the coupling field is assumed to be lossless): Mechanical dynamic equations:

$$\frac{d\delta}{dt} = \Delta\omega_{Pu} * \omega_s \quad \text{(II. 27)}$$

$$2H\frac{d\omega}{dt} = \frac{P_{mech}}{1+\Delta\omega_{Pu}} - \left(\psi_d I_q - \psi_q I_d\right) - T_{f\omega} \quad \text{(II. 28)}$$

Stator dynamic equations:

$$\frac{1}{w_s}\frac{d\psi_d}{dt} = R_s I_d + (1+\Delta\omega_{Pu})\psi_q + V_{dterm} \quad \text{(II. 29)}$$

$$\frac{1}{w_s}\frac{d\psi_q}{dt} = R_s I_q - (1+\Delta\omega_{Pu})\psi_d + V_{qterm} \quad \text{(II. 30)}$$

$$\frac{1}{w_s}\frac{d\psi_0}{dt} = R_s I_0 + V_{0term} \quad \text{(II. 31)}$$

Rotor dynamic equations:

$$T'_{d0}\frac{dE'_q}{dt} = E_{fd} - E'_q - (X_d - X'_d)\left(I_d - \frac{X'_d - X''_d}{(X'_d - X_l)^2}\left(+\psi'_d + (X'_d - X_l)I_d - E'_q\right)\right) \quad \text{(II. 32)}$$

$$T'_{q0}\frac{dE'_d}{dt} = -E'_d - \left(X_q - X'_q\right)\left(I_q - \frac{X'_q - X''_q}{\left(X'_q - X_l\right)^2}\left(-\psi'_q + \left(X'_q - X_l\right)I_q - E'_d\right)\right) \quad \text{(II. 33)}$$

$$T''_{d0}\frac{d\psi'_d}{dt} = -\psi'_d - (X'_d - X_l)I_d + E'_q \quad \text{(II. 34)}$$

$$T''_{q0}\frac{d\psi'_q}{dt} = -\psi'_q - \left(X'_q - X_l\right)I_q + E'_d \quad \text{(II. 35)}$$

Algebraic relationship between stator and rotor fluxes:

$$\psi_d = -I_d X''_d + E'_q\frac{X''_d - X_l}{X'_d - X_l} + \psi'_d\frac{X'_d - X''_d}{X'_d - X_l} \quad \text{(II. 36)}$$

$$\psi_q = -I_q X''_q + E'_d\frac{X''_q - X_l}{X'_q - X_l} + \psi'_q\frac{X'_q - X''_q}{X'_q - X_l} \quad \text{(II. 37)}$$

In the stator differential equations, regardless of what the derivative of these fluxes are, they are multiplied by a very small number ($\frac{1}{\omega_s}$) and thus the left-hand side is near zero anyway, so an approximation is made:

$$\frac{1}{\omega_s}\frac{d\psi_d}{dt} \approx 0 = R_s I_d + (1 + \Delta\omega_{Pu})\psi_q + V_{dterm} \quad (II.38)$$

$$\frac{1}{\omega_s}\frac{d\psi_q}{dt} \approx 0 = R_s I_q - (1 + \Delta\omega_{Pu})\psi_d + V_{qterm} \quad (II.39)$$

$$\frac{1}{\omega_s}\frac{d\psi_0}{dt} \approx 0 = R_s I_0 + V_{0term} \quad (II.40)$$

This gives the following:

$$V_{dterm} = -R_s I_d - (1 + \Delta\omega_{Pu})\psi_q \quad (II.41)$$

$$V_{qterm} = -R_s I_q + (1 + \Delta\omega_{Pu})\psi_d \quad (II.42)$$

Replacing equations (II.37) and (II.36) in equations (II.43) and (II.44) respectively gives:

$$V_{dterm} = -R_s I_d - (1 + \Delta\omega_{Pu})\left(-I_q X''_q + E'_d \frac{X''_q - X_l}{X'_q - X_l} + \psi'_q \frac{X'_q - X''_q}{X'_q - X_l}\right) \quad (II.43)$$

$$V_{qterm} = -R_s I_q + (1 + \Delta\omega_{Pu})\left(-I_d X''_d + E'_q \frac{X''_d - X_l}{X'_d - X_l} + \psi'_d \frac{X'_d - X''_d}{X'_d - X_l}\right) \quad (II.44)$$

This implies:

$$V_{dterm} = -R_s I_d + (1 + \Delta\omega_{Pu})I_q X''_q + (1 + \Delta\omega_{Pu})\left(+E'_d \frac{X''_q - X_l}{X'_q - X_l} + \psi'_q \frac{X'_q - X''_q}{X'_q - X_l}\right) \quad (II.45)$$

$$V_{qterm} = -R_s I_q - (1 + \Delta\omega_{Pu})I_d X''_d + (1 + \Delta\omega_{Pu})\left(+E'_q \frac{X''_d - X_l}{X'_d - X_l} + \psi'_d \frac{X'_d - X''_d}{X'_d - X_l}\right) \quad (II.46)$$

Setting:

$$E''_d = +E'_d \frac{X''_q - X_l}{X'_q - X_l} + \psi'_q \frac{X'_q - X''_q}{X'_q - X_l} \quad (II.47)$$

$$E''_q = +E'_q \frac{X''_d - X_l}{X'_d - X_l} + \psi'_d \frac{X'_d - X''_d}{X'_d - X_l} \quad (II.48)$$

Gives the following:

$$V_{dterm} = -R_s I_d + (1 + \Delta\omega_{Pu}) I_q X''_q + (1 + \Delta\omega_{Pu}) E''_d \quad (II.49)$$

$$V_{qterm} = -R_s I_q - (1 + \Delta\omega_{Pu}) I_d X''_d + (1 + \Delta\omega_{Pu}) E''_q \quad (II.50)$$

The term $(1 + \Delta w_{Pu})$ is removed because multiplying all the transmission line X values by per unit frequency to scale the network impedances as system frequency changes cannot be done in stability studies [36].

$$V_{dterm} = E''_d (1 + \Delta\omega_{Pu}) - R_s I_d + I_q X''_q \quad (II.51)$$

$$V_{qterm} = E''_q (1 + \Delta\omega_{Pu}) - R_s I_q - I_d X''_d \quad (II.52)$$

The final complete model of per-unitized equations is:

Algebraic relationships:

$$E''_d = +E'_d \frac{X''_q - X_l}{X'_q - X_l} + \psi'_q \frac{X'_q - X''_q}{X'_q - X_l} \quad (II.53)$$

$$E''_q = +E'_d \frac{X''_d - X_l}{X'_d - X_l} + \psi'_d \frac{X'_d - X''_d}{X'_d - X_l} \quad (II.54)$$

$$\psi_d = -I_d X''_d + E''_d \quad (II.55)$$

$$\psi_q = -I_q X''_q + E''_q \quad (II.56)$$

$$V_{dterm} = E''_d (1 + \Delta\omega_{Pu}) - R_s I_d + I_q X''_q \quad (II.57)$$

$$V_{qterm} = E''_q (1 + \Delta\omega_{Pu}) - R_s I_q - I_d X''_d \quad (II.58)$$

Differential equations:

$$\frac{d\delta}{dt} = \Delta\omega_{Pu} * \omega_s \quad (II.59)$$

$$2H\frac{d\omega}{dt} = \frac{P_{mech}}{1+\Delta\omega_{Pu}} - \left(\psi_d I_q - \psi_q I_d\right) \quad \text{(II. 60)}$$

$$T'_{d0}\frac{dE'_q}{dt} = E_{fd} - E'_q - (X_d - X'_d)\left(I_d - \frac{X'_d - X''_d}{(X'_d - X_l)^2}\left(+\psi'_d + (X'_d - X_l)I_d - E'_q\right)\right) \quad \text{(II. 61)}$$

$$T'_{q0}\frac{dE'_d}{dt} = -E'_d - \left(X_q - X'_q\right)\left(I_q - \frac{X'_q - X''_q}{\left(X'_q - X_l\right)^2}\left(-\psi'_q + \left(X'_q - X_l\right)I_q - E'_d\right)\right) \quad \text{(II. 62)}$$

$$T''_{d0}\frac{d\psi'_d}{dt} = -\psi'_d - (X'_d - X_l)I_d + E'_q \quad \text{(II. 63)}$$

$$T''_{q0}\frac{d\psi'_q}{dt} = -\psi'_q - \left(X'_q - X_l\right)I_q + E'_d \quad \text{(II. 64)}$$

The field voltage E_{fd} is an input from the exciter. The equation of the product of the field current and the mutual inductance $L_{ab}I_{fd}$ is given as follows:

The transformation is done as follows:

$$\begin{bmatrix} V_D \\ V_Q \\ V_0 \end{bmatrix} = T_{sync}V_{abc} = T_{sync}\begin{bmatrix} V_a \\ V_b \\ V_c \end{bmatrix} \quad \text{(II. 67)}$$

$$T_{sync} = \frac{2}{3}\begin{bmatrix} \cos(\omega_s t) & \cos\left(\omega_s t - \frac{2\pi}{3}\right) & \cos\left(\omega_s t + \frac{2\pi}{3}\right) \\ -\sin(\omega_s t) & -\sin\left(\omega_s t - \frac{2\pi}{3}\right) & -\sin\left(\omega_s t + \frac{2\pi}{3}\right) \\ \frac{1}{2} & \frac{1}{2} & \frac{1}{2} \end{bmatrix} \quad \text{(II. 68)}$$

$$T^{-1}_{sync} = \frac{2}{3}\begin{bmatrix} \cos(\omega_s t) & -\sin(\omega_s t) & 1 \\ \cos\left(\omega_s t - \frac{2\pi}{3}\right) & -\sin\left(\omega_s t - \frac{2\pi}{3}\right) & 1 \\ \cos\left(\omega_s t + \frac{2\pi}{3}\right) & -\sin\left(\omega_s t + \frac{2\pi}{3}\right) & 1 \end{bmatrix} \quad \text{(II. 69)}$$

$$\begin{bmatrix} V_a \\ V_b \\ V_c \end{bmatrix} = \begin{bmatrix} V_t\cos(\omega_s t + \alpha) \\ V_t\cos\left(\omega_s t + \alpha - \frac{2\pi}{3}\right) \\ V_t\cos\left(\omega_s t + \alpha + \frac{2\pi}{3}\right) \end{bmatrix} \quad (II.70)$$

is chosen an input for the system, the result is going to be:

$$\begin{bmatrix} V_D \\ V_Q \\ V_0 \end{bmatrix} = \begin{bmatrix} +V_t\cos(\alpha) \\ +V_t\sin(\alpha) \\ 0 \end{bmatrix} \quad (II.71)$$

It can be easily remarqued that all the ($w_s t$) terms cancel out. This means that the new reference frame can be treated like a complex number:

$$V_D + jV_Q = V_t\cos(\alpha) + j\,V_t\sin(\alpha) = V_t e^{j\alpha} \quad (II.72)$$

The abc quantities are converted to machine reference frame (dq0 reference), there is a need for the dqo quantities to be transformed to the network reference:

$$\begin{bmatrix} V_a \\ V_b \\ V_c \end{bmatrix} = {T^{-1}}_{dq0i} \begin{bmatrix} V_{di} \\ V_{qi} \\ V_{0i} \end{bmatrix} \quad (II.73)$$

$$\begin{bmatrix} V_D \\ V_Q \\ V_0 \end{bmatrix} = T_{sync} \begin{bmatrix} V_a \\ V_b \\ V_c \end{bmatrix} = T_{sync} {T^{-1}}_{dq0i} \begin{bmatrix} V_{di} \\ V_{qi} \\ V_{0i} \end{bmatrix} \quad (II.74)$$

Therefore, a direct conversion from the machine reference frame into the network reference frame without passing by the abc phase reference.

$$Network\ refrence\ frame \rightarrow \begin{bmatrix} V_D \\ V_Q \\ V_0 \end{bmatrix} = T_{sync} {T^{-1}}_{dq0i} \begin{bmatrix} V_{di} \\ V_{qi} \\ V_{0i} \end{bmatrix} \leftarrow Machine\ refrence\ frame \quad (II.75)$$

As mentioned in (II.13) and in (II.24) that:

$$T_{dq0}{}^{-1} = \frac{2}{3}\begin{bmatrix} \sin\left(\frac{P}{2}\theta_{shaft}\right) & \cos\left(\frac{P}{2}\theta_{shaft}\right) & 1 \\ \sin\left(\frac{P}{2}\theta_{shaft} - \frac{2\pi}{3}\right) & \cos\left(\frac{P}{2}\theta_{shaft} - \frac{2\pi}{3}\right) & 1 \\ \sin\left(\frac{P}{2}\theta_{shaft} + \frac{2\pi}{3}\right) & \cos\left(\frac{P}{2}\theta_{shaft} + \frac{2\pi}{3}\right) & 1 \end{bmatrix} \quad \text{(II. 76)}$$

This makes the inverse matrix $T_{dq0i}{}^{-1}$ for a particular machine "i" looks like the following:

$$T_{dq0i}{}^{-1} = \frac{2}{3}\begin{bmatrix} \sin(\omega_s t + \delta_i) & \cos(\omega_s t + \delta_i) & 1 \\ \sin\left(\omega_s t + \delta_i - \frac{2\pi}{3}\right) & \cos\left(\omega_s t + \delta_i - \frac{2\pi}{3}\right) & 1 \\ \sin\left(\omega_s t + \delta_i + \frac{2\pi}{3}\right) & \cos\left(\omega_s t + \delta_i + \frac{2\pi}{3}\right) & 1 \end{bmatrix} \quad \text{(II. 77)}$$

The matrix $T_{sync}T_{dq0i}{}^{-1}$ multiplication end up as follows:

$$T_{sync}T_{dq0i}{}^{-1} = \begin{bmatrix} +\sin(\delta_i) & +\cos(\delta_i) & 0 \\ -\cos(\delta_i) & +\sin(\delta_i) & 0 \\ 0 & 0 & 1 \end{bmatrix} \quad \text{(II. 78)}$$

The conversion from network to machine reference frame also can be done by the matrix:

$$T_{dq0i}T_{sync}{}^{-1} = \left(T_{sync}T_{dq0i}{}^{-1}\right)^{-1} = \begin{bmatrix} +\sin(\delta_i) & -\cos(\delta_i) & 0 \\ +\cos(\delta_i) & +\sin(\delta_i) & 0 \\ 0 & 0 & 1 \end{bmatrix} \quad \text{(II. 79)}$$

The subscript "i" for all variables and parameters to denote machine i. The final relation between the machine reference frame and the network reference frame, after omitting the zero values will look like this:

$$\begin{bmatrix} V_{dnetwork} \\ V_{qnetwork} \end{bmatrix} = \begin{bmatrix} +\sin(\delta_i) & +\cos(\delta_i) \\ -\cos(\delta_i) & +\sin(\delta_i) \end{bmatrix} \begin{bmatrix} V_{dmachine} \\ V_{qmachine} \end{bmatrix} \quad \text{(II. 80)}$$

$$\begin{bmatrix} V_{dmachine} \\ V_{qmachine} \end{bmatrix} = \begin{bmatrix} +\sin(\delta_i) & -\cos(\delta_i) \\ +\cos(\delta_i) & +\sin(\delta_i) \end{bmatrix} \begin{bmatrix} V_{dnetwork} \\ V_{qnetwork} \end{bmatrix} \quad \text{(II. 81)}$$

As a result, the dq values can be treated as real and imaginary numbers and the conversion is then simple complex number rotation:

$$\left(V_{dnetwork} + jV_{qnetwork}\right) = \left(V_{dmachine} + jV_{qmachine}\right)e^{+j\left(\delta-\frac{\pi}{2}\right)} \quad \text{(II. 82)}$$

$$\left(V_{dmachine} + jV_{qmachine}\right) = \left(V_{dnetwork} + jV_{qnetwork}\right)e^{-j\left(\delta-\frac{\pi}{2}\right)} \quad \text{(II. 82)}$$

The equations that model the connection of the generator to network are

$$V_{dterm} = E''_d\left(1 + \Delta\omega_{Pu}\ \right) - R_s I_d + I_q X''_q \quad \text{(II. 83)}$$

$$V_{qterm} = E''_q(1 + \Delta\omega_{Pu}) - R_s I_q - I_d X''_d \quad \text{(II. 84)}$$

After making the assumption that $jX''_d = X''_q$, it gives a simple circuit equation:

$$V_{dterm} + jV_{qterm} = (1 + \Delta w_{Pu})\left(E''_d + jE''_q\right) - \left(R_s + jX''_d\right)\left(I_d + jI_q\right) \quad \text{(II. 85)}$$

Converting from the "dq" reference to the network reference gives:

$$V_r + jV_i = (1 + \Delta\omega_{Pu})\left(E''_d + jE''_q\right)e^{+j\left(\delta-\frac{\pi}{2}\right)} \quad \text{(II. 86)}$$

$$I_r + jI_i = \left(I_d + jI_q\right)e^{+j\left(\delta-\frac{\pi}{2}\right)} \quad \text{(II. 87)}$$

$$V_{rterm} + jV_{iterm} = (V_r + jV_i) - \left(R_s + jX''_d\right)(I_r + jI_i) \quad \text{(II. 88)}$$

II.3 Excitation System

The basic function of an excitation system is to provide direct current to the synchronous machine field winding. In addition, the excitation system performs control and protective functions essential to the satisfactory performance of the power system by controlling the field voltage and thereby the field current. [44]

The control functions include the control of voltage and reactive power flow, and the enhancement of system stability. The protective functions ensure that the capability limits of the synchronous machine, excitation system, and other equipment are not exceeded. [8]

There are three distinct types of excitation systems based on the power source for exciter.

1- DC Excitation Systems (DC) which utilize a DC generator with commutator.

2- AC Excitation Systems (AC) which use alternators and either stationary or rotating rectifiers to produce the direct current needed.

3- Static Excitation systems (ST) in which the power is supplied through transformer and rectifiers. [43] The first two types of exciters are also called rotating exciters which are mounted on the same shaft as the generator and driven by the prime mover. [15]

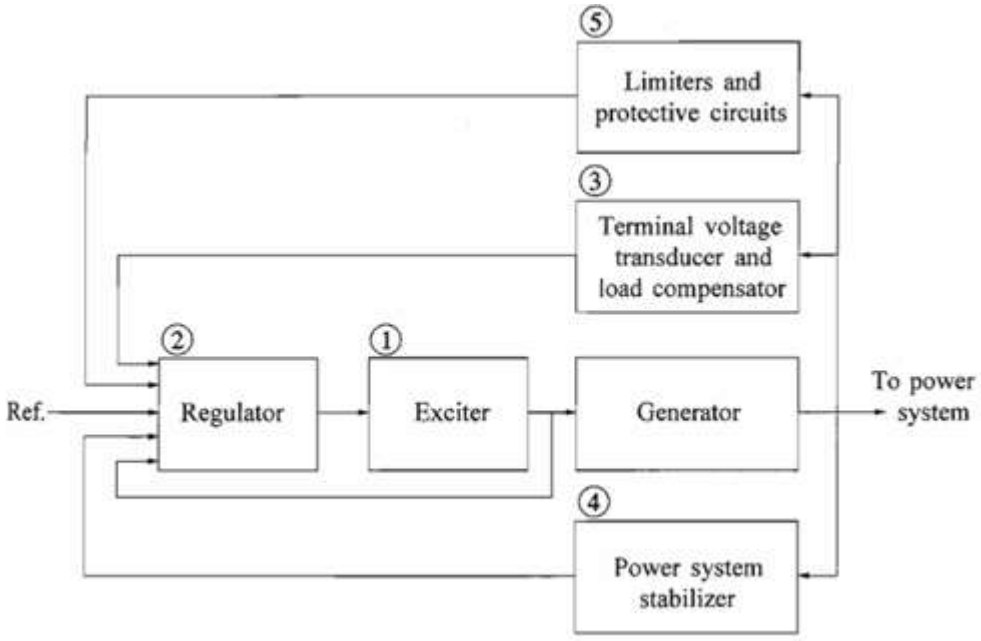

Figure II-3: Functional Block Diagram of a Synchronous Generator Excitation Control System**[44]**

The following is a brief description of the various subsystems identified in Fig. II.3:

(1) Exciter: provides dc power to the synchronous machine field winding, constituting the power stage of the excitation system. [28]

(2) Regulator: processes and amplifies input control signals to a level and form appropriate for control of the exciter. This includes both regulating and excitation system stabilizing functions. [5]

(3) Terminal voltage transducer and load compensator: senses generator terminal voltage, rectifies and filters it to dc quantity, and compares it with a reference which represents the desired terminal voltage. In addition, load compensation may be provided, if

it desired to hold constant voltage at some point electrically remote from the generator terminal. [5] Its block diagram is shown in Fig. II.4:

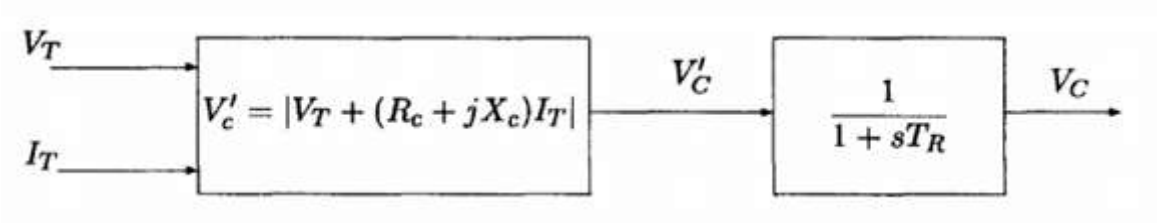

Figure II-4: Transducer and load compensator block diagram[44]

(4) Power system stabilizer: provides an additional input signal to the regulator to damp power system oscillations. Some commonly used input signals are rotor speed deviation, accelerating power, and frequency deviation. [5]

(5) Limiters and protective circuits: These include a wide array of control and protective functions which ensure that the capability limits of the exciter and synchronous generator are not exceeded. [5]

One type of the excitation system is the IEEE Type 1 Excitation System is shown in Fig. II.5.

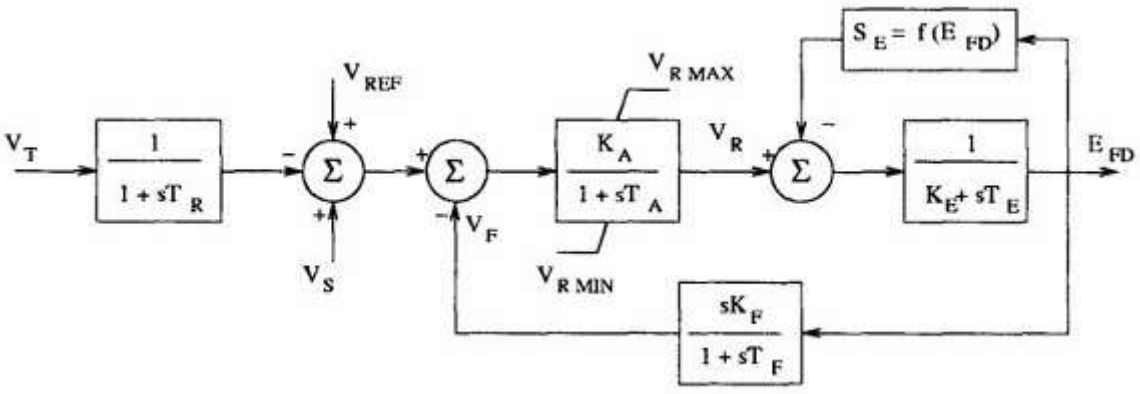

Figure II-5: IEEE Type 1 Excitation System

The state equations for the system are given below:

$$\frac{dE_{fd}}{dt} = \frac{1}{T_e}\left(\left[K_e + S_E(E_{fd})\right]E_{fd} + V_R\right) \qquad (II.89)$$

$$\frac{dV_2}{dt} = \frac{1}{T_F}\left(-V_2 + \frac{K_F}{T_F}E_{fd}\right) \quad (90)$$

$$\frac{dV_1}{dt} = \frac{1}{T_R}(-V_1 + V_T) \quad (91)$$

$$V_{ERR} = V_{REF} - V_1 \quad (92)$$

$$V_F = \frac{K_F}{T_F}E_{FD} - V_2 \quad (93)$$

$$F_R = \frac{1}{T_A}([-V_R + K_A(V_{ERR} + V_S - V_F)]) \quad (94)$$

The limiter of these state equations is a non-windup limiter and is defined as follows:

If $V_R > V_{Rmax}$ set $V_R = V_{Rmax}$

If $V_R = V_{Rmax}$ and $F_R > 0$, set $\frac{dV_R}{dt} = 0$

If $V_R < V_{Rmin}$ set $V_R = V_{Rmin}$

If $V_R = V_{Rmin}$ and $F_R < 0$, set $\frac{dV_R}{dt} = 0$

Otherwise $\frac{dV_R}{dt} = F_R$

II.4Loads

In general, to perform power system analysis, models must be developed for all pertinent system components. Inadequate modelling causing under/over-building of the system or degrading reliability between generated power and demand power by loads must be maintained to keep the system continuously in stable operation. Therefore, load characteristics are of crucial importance to be employed in system analysis as they have a significant effect on system performance and highly impact the stability results [45]. Load modeling refers to the mathematical representation of the relationship between the power

and voltage in a load bus. Load models can be classified into two main categories: static and dynamic models [46].

II.5 Transmission line modeling

Electrical power is transferred from generating stations to consumers through transmission lines, which are characterized by four parameters: series resistance R due to the conductor resistivity, shunt conductance G due to leakage current between the phases and ground, series inductance L due to magnetic field surrounding the conductors, and shunt capacitance C due to the electric field between conductors [44].

Transmission lines can be classified according to their lengths as:

Short line model: For lines less than about 80 km (50 miles), the capacitance may be ignored without causing appreciable error in calculating the voltage and current. Therefore, the short line model is obtained by multiplying the series impedance per unit length by the line length.

Where r and L are respectively the resistance and the inductance per unit of length of the transmission line. l is the line length.

The Figure below shows the short line model on a per-phase basis:

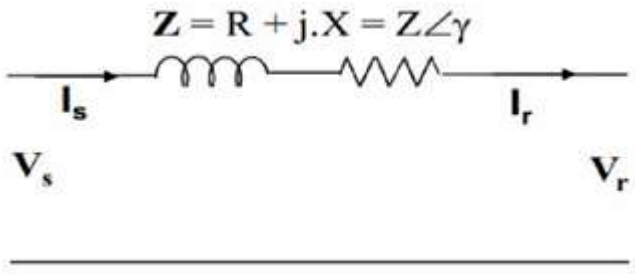

Figure II-6: The equivalent PI-circuit of short transmission line

The equations for this model are:

$$I_S = I_R \qquad (II.95)$$

$$\boldsymbol{V_S = V_r + Z.I_R} \qquad (\boldsymbol{II.96})$$

1. Medium line model: As the length of the line increases, the line charging current becomes appreciable and the shunt capacitance must be considered. Lines above 80km (50miles) and below 250 km (150miles) in length are termed as medium length lines. For medium length lines, half of the shunt capacitance may be considered to be lumped at each end of the line. This is referred as the nominal π model as shown in the following figure:

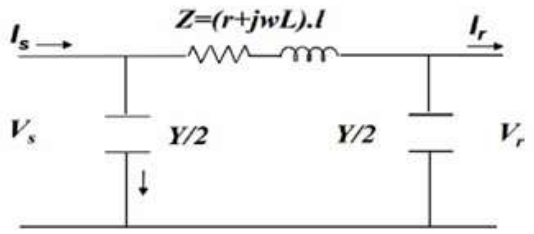

Figure II-7: The equivalent PI-circuit of medium transmission line

Equations for this model are:

$$I_S = Y.\left(1 + \frac{ZY}{4}\right)V_R + \left(1 + \frac{ZY}{2}\right)I_R \qquad (\text{II.}97)$$

$$V_S = \left(1 + \frac{ZY}{2}\right)V_R + Z.I_R \qquad (II.98)$$

$Y = (g + jCw).l = jCwl(1.106)$ as the conductance is neglected g=0.

$$Z = (r + jwl).l \qquad (\text{II.}99)$$

Long line model: For 250 km (150mile) lines and longer, the effect of distributed parameters must be considered.

The Figure below shows the equivalent PI-circuit of long Transmission line:

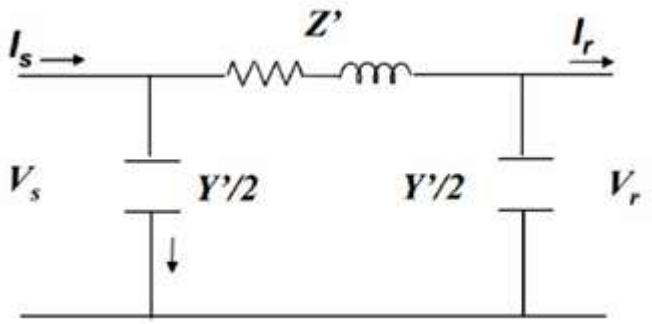

Figure II-3: The equivalent PI-circuit of long transmission line

The equations of this model are:

$$I_S = Y'.\left(1 + \frac{Z'Y'}{4}\right)V_R + \left(1 + \frac{Z'Y'}{2}\right)I_R \qquad (II.100)$$

$$V_S = \left(1 + \frac{Z'Y'}{2}\right)V_R + Z'.I_R \qquad (II.101)$$

Where:

$$Z' = Z.\frac{\sinh \gamma l}{\gamma l} \qquad (II.102)$$

$$Y' = Y.\frac{\tanh \frac{\gamma l}{2}}{\frac{\gamma l}{2}} \qquad (II.103)$$

γ Knowns as the propagation constant, is a complex expression given by :

$$\gamma = \sqrt{zy} = \sqrt{(r + JWL)(jCw)} \qquad (II.104)$$

II.6 Power system stabilizer

The basic function of a power system stabilizer is to extend stability limits by modulating generator excitation to provide damping to the oscillations of synchronous machine rotors relative to one another. Insufficient damping of these oscillations may limit the ability to transmit power [47]. To provide damping, the stabilizer must produce an electrical torque in phase with the rotor speed deviations [8].

The general block diagram of the PSS is presented in Fig. II.11.

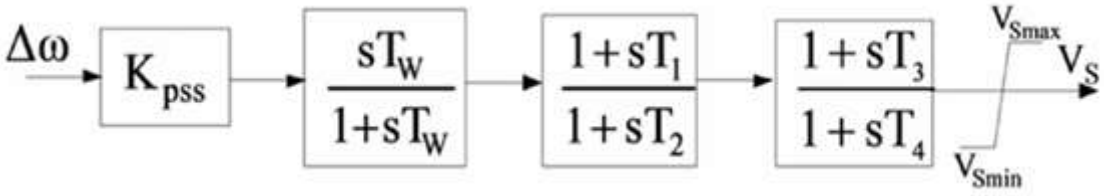

Figure II-9: Block diagram of PSS

II.7 DFIG model

Doubly fed induction generator model which is divided into six for modeling purposes, there include the Turbine, the generator itself, the LCL filter, back-to-back capacitor (B2BC), the rotor/machine side converter, and the grid side converter.[36]

II.7.1 Wind turbine modelling

Wind speed is fed to the wind turbine and electrical torque inputs; in turn, it provides generator speed as output. The turbine relates wind speed to the induction generator rotor speed.

It is divided into two subsystems.

(i) An aerodynamic model: it converts the wind speed in the turbine to mechanical output. The mechanical output of the turbine can be represented in Equation (II.105).

$$\boldsymbol{P_t = 0.5\rho\pi R^2 C_p(\beta,\lambda)v_\omega^3[W]} \qquad (\boldsymbol{II.105})$$

Where the air density is given as ρ, the wind speed is given by $\boldsymbol{v_\omega}$, R is the turbine blade length, $p(\beta,\lambda)$ represent the blade's power coefficient which is part of wind power that can be extracted by the turbine, and it depends on the functions β,λ. In a practical setup, the performance curve of the turbine is specified through the tested field data. However, for simulation purpose, Equations representing numerical approximations adopted from the study [48] is given in Equation (II.106)

$$\boldsymbol{C_p(\beta,\lambda) = 0.5176\left(\frac{116}{\lambda+0.8\beta} - \frac{4.06}{1+\beta^3} - 0.4\beta 5\right)e^{\left(\frac{-21}{\lambda+0.08\beta}+\frac{0.735}{1+\beta^3}\right)} + 0.0068\lambda} \qquad (\boldsymbol{II.106})$$

Where the blade pitch angle is β , λ is the tip turbine speed ratio;

(ii) The drive train model uses the mechanical power output to drive the induction generator. The drive train model uses two masses attached to the shaft adopted from the study [49] shown in Equation (II.107 –II.110).

$$\frac{d}{dt}\omega_g = \frac{1}{2H_g}\left(T_s - T_g\right) \qquad (\boldsymbol{II.107})$$

$$T_s = k_{tg}\theta_{tg} + c_{tg}\frac{d}{dt}\theta_{tg} \qquad (\boldsymbol{II.108})$$

$$\frac{d}{dt}\theta_{tg} = w_{elB}\left(\omega_t - \omega_g\right) \qquad (\boldsymbol{II.109})$$

$$\frac{d}{dt}\omega_t = \frac{1}{2H_t}(T_t - T_s) \qquad (\boldsymbol{II.110})$$

II.7.2 Doubly fed induction generator

the generator takes the rotor speed from the generator (ω_g), the bus voltage of the generator (Vg) from the network model as inputs and in turn, generate the output current (ig) and electrical torque (Tg). The name DFIG means it has two feeds the stationary part stator and the rotating part rotor. The stator windings are arranged such that the output stator currents produce a magnetic field that is rotating at angular speed in the air gap. The stator currents (isd,isq) in dq reference (same as the SMIB conversion process) produced in the generator can be represented by Equations (II.111 –II.112).

$$\frac{L'_s}{\omega_{elB}}\frac{d}{dt}i_{sd} = -\omega_s L'_s i_{sq} - R_1 i_{sd} + \frac{e'_{sq}}{\omega_s T_r} + \frac{\omega_g e'_{sd}}{\omega_s} - v_{sd} + K_{mrr}v_{rd} \qquad (\boldsymbol{II.111})$$

$$\frac{L'_s}{\omega_{elB}}\frac{d}{dt}i_{sq} = -R_1 i_{sq} + \omega_s L'_s i_{sd} + \frac{\omega_g e'_{sq}}{\omega_s} - \frac{e'_{sd}}{\omega_s T_r} - v_{sq} + K_{mrr}v_{rq} \qquad (\boldsymbol{II.112})$$

Voltages behind transient impedances (esq' ,esd') are represented in Equations (II.113 – II.114).

$$\frac{1}{\omega_s\omega_{elB}}\frac{d}{dt}e'_{sd} = -R_2 i_{sq} - \left(1 - \frac{\omega_g}{\omega_s}\right)e'_{sq} - \frac{e'_{sd}}{\omega_s T_r} + K_{mrr}v_{rq} \qquad (\boldsymbol{II.113})$$

$$\frac{1}{\omega_s\omega_{elB}}\frac{d}{dt}e'_{sq} = R_2 i_{sd} - \frac{e'_{sq}}{\omega_s T_r} + \left(1 - \frac{\omega_g}{\omega_s}\right)e'_{sd} + K_{mrr}v_{rd} \qquad (\boldsymbol{II.114})$$

Rotor currents irq and ird are given by Equation (II.115 –II.116). and shown

$$i_{rq} = -\left(\frac{e'_{sd}}{X_m}\right) - K_{mrr} i_{sq} \quad (\boldsymbol{II.115})$$

$$i_{rd} = -\left(\frac{e'_{sq}}{X_m}\right) - K_{mrr} i_{sd} \quad (\boldsymbol{II.116})$$

Rotor active power Pr, stator reactive power Qs and electrical torque Tg are given as Equations (II.118–II.119) and (II.121)..

$$P_S = v_{sq} i_{sq} + v_{sd} i_{sd} \quad (\boldsymbol{II.117})$$

$$P_r = v_{rq} i_{rq} + v_{rd} i_{rd} \quad (\boldsymbol{II.118})$$

$$Q_S = -v_{sq} i_{sq} + v_{sd} i_{sd} \quad (\boldsymbol{II.119})$$

$$Q_r = -v_{rq} i_{rq} + v_{rd} i_{rd} \quad (\boldsymbol{II.120})$$

$$T_g = L_m\left(i_{sq} i_{rd} - i_{sd} i_{rq}\right) \quad (\boldsymbol{II.121})$$

II.7.3 LCL filter

To complete the DFIG, the power grid system is linked to the rotor winding, the rotor winding consists of a back-to-back capacitor, filter, and converters. An inductor-capacitor inductor (LCL) type of filter is used in this study. It is made of two inductors (Li,Lg), a damping resistor (Rc) and a capacitor (Cf). The LCL model takes inverter voltage (viq,vid) and stator voltage (vsq,vsd) as inputs and provides the current injected into the grid through the filter (igq, igd) as outputs. The filter Equations are shown from (II.126 –II.127).

$$\frac{L_i}{\omega_b}\frac{d}{dt} i_{iq} = v_{iq} - v_{cq} - (R_i + R_c) i_{iq} + \omega L_i i_{id} + R_c i_{gq} \quad (\boldsymbol{II.122})$$

$$\frac{L_i}{\omega_b}\frac{d}{dt} i_{id} = v_{id} - v_{cd} - (R_i + R_c) i_{id} - \omega L_i i_{iq} + R_c i_{gd} \quad (\boldsymbol{II.123})$$

$$\frac{L_g}{\omega_b}\frac{d}{dt} I_{gq} = v_{cq} - v_{gq} - \left(R_g + R_c\right) I_{gq} + \omega L_g I_{gd} + R_c I_{iq} \quad (\boldsymbol{II.124})$$

$$\frac{L_g}{\omega_b}\frac{d}{dt} I_{gd} = v_{cd} - v_{gd} - \left(R_g + R_c\right) I_{gd} - \omega L_g I_{gq} + R_c I_{id} \quad (\boldsymbol{II.125})$$

$$\frac{C_f}{\omega_b}\frac{d}{dt} v_{cq} = I_{iq} - I_{gq} - \omega C_f V_{cd} \quad (\boldsymbol{II.126})$$

$$\frac{C_f}{\omega_b}\frac{d}{dt} v_{cd} = I_{id} - I_{gd} + \omega C_f V_{cq} \quad (\boldsymbol{II.127})$$

Measure P and measure Q represent the converter terminal active power output and output reactive power at the filter terminal. It is modeled as seen in Equations (II.128 –II.129).

$$P_{gsc} = v_{iq} i_{iq} + v_{id} i_{id} \quad (\boldsymbol{II.128})$$

$$Q_{gsc} = -v_{iq} i_{gd} + v_{sd} i_{gq} \quad (\boldsymbol{II.129})$$

II.7.4 Back-to-back capacitor

This B2BC connects the rotor windings to the power grid system through the LCL filter. The capacitor has a dc link, the capacitor voltage can be represented by Equation (II-130)

$$\frac{1}{C_{dc}} p V_{dc} = \frac{1}{V_{dc}} \left(P_{msc} - P_{gsc} \right) \quad (\boldsymbol{II.130})$$

Where $Pmsc$ is the machine side converter active power, $Pgsc$ is the grid-side converter active power. The capacitor voltage Vdc , the capacitance is Cdc .

II.7.5 Machine-side converter controller

The converter or controller model receives voltages, generator rotor speed and current in the form of electrical signals and produces corresponding switching signals for the converter. The vector control method through which independent control of active and reactive power, torque, and voltage control is achieved is adopted in this study. However, this vector control is possible only when one of the dq axes is aligned to the stator voltage. The DFIG power test system developed so far has the q-axis aligned to the infinite bus voltage. The measurements of the voltage and current must be aligned to a new reference frame which is inside the power test system controllers. The controllers adopted in this study have a simple model of two cascaded proportional-integral (PI).

II.7.6 Grid-side converter controller

Like the machine side converter/controller, it also has two cascaded proportional-integral (PI) controllers regulating the voltage capacitor and reactive power flow from the grid side controller at the wind turbine generator bus. Rotor power is transferred to the grid ($Pr = Pgsc$), by regulating the capacitor voltage reference value.

II.8 Conclusion

In this chapter, a comprehensive dynamic modeling of critical power system components has been developed, laying the groundwork for in-depth stability and performance analysis. By representing the synchronous generator, excitation system, loads, transmission lines, power system stabilizers, and double-fed induction motors, the intricate interactions within the power system are captured. These models are essential for understanding system dynamics, designing effective control strategies, and ensuring reliable operation under both normal and fault conditions. The insights gained here will be instrumental in subsequent chapters, which focus on system stability and controller optimization.

Chapter three

Design of PSS for conventional power system

CHAPTER THREE

III.1 Introduction

This study proposes a Marine Predator Algorithm (MPA) approach to optimize PSS parameters to enhance small signal stability in power systems. The MPA stands out for its robustness and adaptability across a range of optimization problems. MPA has demonstrated its success in various domains, including blade shape optimization of Savonius wind turbines [48], parameter estimation of photovoltaic systems, and energy efficiency optimization in buildings with solar panel systems[49]. Furthermore, it has been effectively applied to pavement maintenance and rehabilitation planning [50] and optimal allocation of active and reactive power resources in power distribution networks [51]. These diverse applications highlight the versatility of the MPA in addressing both engineering challenges and resource optimization problems, establishing its potential for broader applications. This chapter provides a comprehensive analysis of the application of the Marine Predator Algorithm (MPA) in optimizing power system stabilizers (PSS). It begins with an introduction to the system tests, detailing the power systems under study, their configurations, and the parameters used for analysis. An overview of the MPA and its cost function is presented, highlighting the optimization mechanism and objectives. The simulation results demonstrate the application of MPA and other metaheuristic algorithms for PSS parameter optimization, discussing the performance improvements achieved. Experimental validation of the MPA-optimized PSS is conducted to emphasize its practical applicability. The chapter concludes by summarizing the key findings from both simulation and experimental results, underscoring the contributions of the MPA-optimized PSS to enhancing power system stability.

III.2 Power System Tests

The effectiveness of the proposed Algorithm was tested on three different power systems, The SMIB, the Western Systems Coordinating Council (WSCC) 3-machine and 9-bus power system and 10-machine 39-bus New England power system.

III.2.1 Test system 1: SMIB

In this system, the synchronous machine is connected via a line to an infinite bus, as shown in Figure III.1. An infinite bus is a bus, which has a fixed voltage (both magnitude and angle) and frequency. The infinite bus can be used to represent the connection to a strong grid, which will absorb the injected power at the infinite bus connection point, without a noticeable change in the voltage or frequency. While the voltage angle and magnitude at Bus 2 is fixed, the voltage magnitude and angle at Bus 1 varies according to the current injected at Bus 1. The system's parameters used in the simulation are given in Table A.1 in Appendix A.

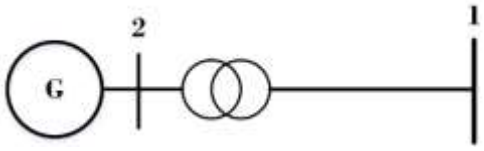

Figure III-1:Schematic of SMIB system.

III.2.2 Test system 2: Three-Machine Power System

In the second test system, a widely used Western Systems Coordinating Council (WSCC) 3-machine, 9-bus power system is considered [3]. Line diagram of the WSCC power system is shown in Figure III_2 . The G1 is the slack bus generator and its rotor angle (δ1) is selected as the reference angle. The generators are represented as fourth-order models. All dynamic parameters of the WSCC power system are given in Table A.2 in Appendix A.

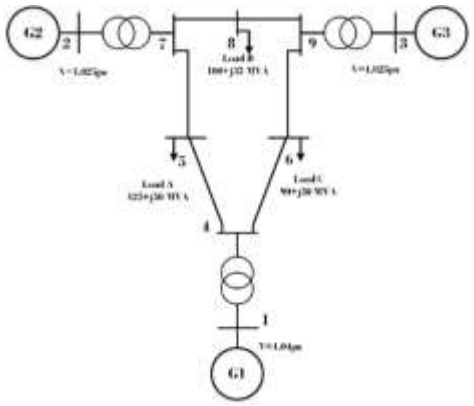

Figure III-2: WSCC power test system.

III.2.3 Test system 2: Ten-Machine Power System

The second test system is a complex inter-area power system, comprising 10 generators and 39 buses as shown in Figure III , commonly known as the New England Power System. Generator G2 serves as the slack bus, with its rotor angle (δ2) designated as the reference angle. The generators are modeled using fourth-order representations to accurately capture dynamic behavior. All relevant dynamic parameters for this system are detailed in Tables A.3 in Appendix A.

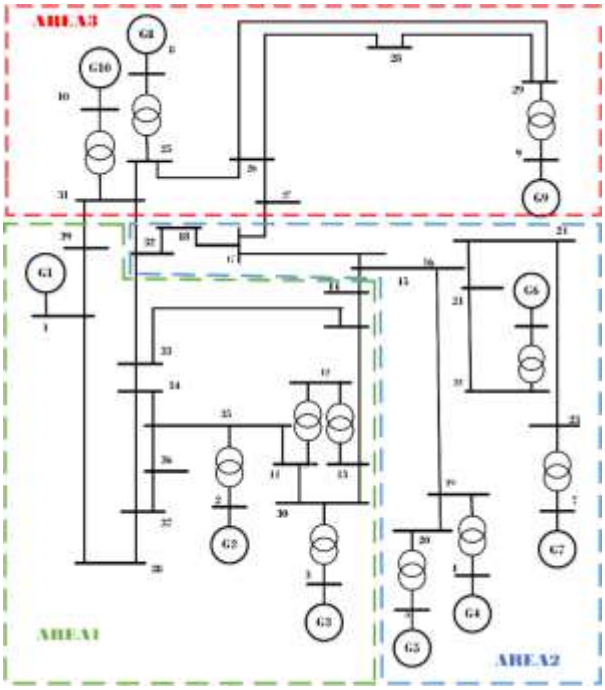

Figure III-3: the New England power system

III.3 Problem Optimization

In this study, we suggest an optimal tuning approach for power system stabilizers (PSSs) to enhance LFO damping. The goal is to achieve coordinated tuning of the PSS parameters using a robust and effective optimization technique. Tuning PSSs can be challenging due to the numerous parameters involved, especially in MMPS. Since power systems exhibit non-linear behavior and have a high number of optimization parameters, we employ the MPA in this study. The MPA algorithm, as an evolutionary technique, is known for finding optimal solutions even in non-linear and high-dimensional problems. Further, the tuning process of

PSS parameters using metaheuristic optimization is presented in Figure III_4 and the MPA parameters are given in Tables A.4 in Appendix A.

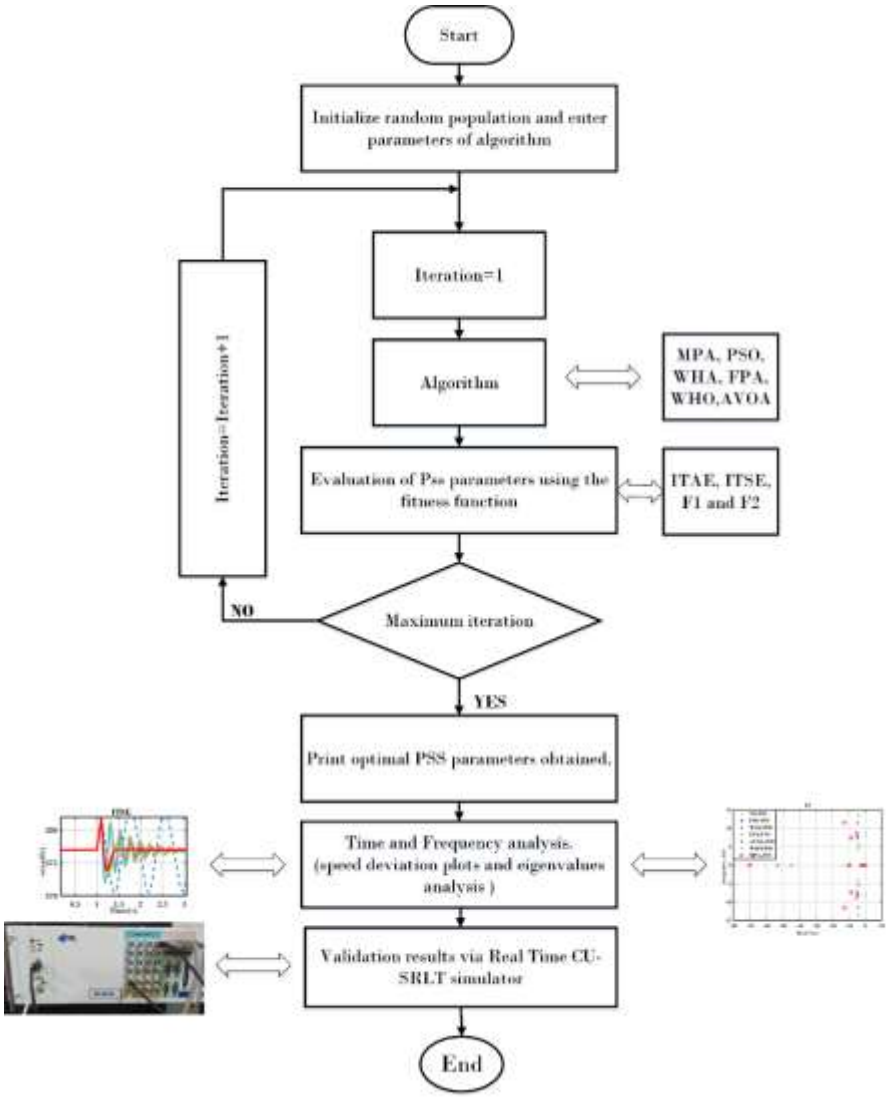

Figure III-4: Tuning process of PSS parameters using metaheuristic optimization.

III.3.1 Marine Predator Algorithm (MPA)

The foraging movements of marine predators' act as an inspiration for MPA. Predators frequently alternate between two motion patterns: Brownian motion, which is continuous steps in the same vacancy that enhances exploitation, and Levy motion, which includes brief movements followed by high jumps that boosts exploration. Figure (III-5) illustrates the vital phases of the MPA and can be summarized as follows; see [52] for more details.

[1] Initialization: the search space is first filled with a uniformly and randomly distributed initial solution.

[2] The Prey matrices are updated in Phase (1), the first third of iterations.

$$\overrightarrow{Step_\iota} = \overrightarrow{Step_\iota} \otimes \left(\overrightarrow{Elite_\iota} - \left(\overrightarrow{R_B} \otimes \overrightarrow{Prey_\iota}\right)\right) \quad (III.1)$$

$$\overrightarrow{Prey_\iota} = \overrightarrow{Prey_\iota} + \left(P.\vec{R} - \left(\overrightarrow{R_B} \otimes \overrightarrow{Step_\iota}\right)\right) \quad (III.2)$$

where RB is a vector of arbitrary numbers based on the normal distribution of Brownian motion, P = 0.5, and R is a vector of uniform random integers between [0,1]. The prey uses Brownian motion to move. (Note: The Prey matrix is multiplied by RB.)

[3] Phase (2), or the second third of the iterations, is characterized by the following equation updating the first half of the population: the predator moves in Brownian motion while the prey moves by Levy motion.

$$\overrightarrow{Step_\iota} = \overrightarrow{R_L} \otimes \left(\overrightarrow{Elite_\iota} - \left(\overrightarrow{R_L} \otimes \overrightarrow{Prey_\iota}\right)\right) \quad (III.3)$$

$$\overrightarrow{Prey_\iota} = \overrightarrow{Prey_\iota} + \left(P.\vec{R} \otimes \overrightarrow{Step_\iota}\right) \quad (III.4)$$

where RL, a vector of values that are random based on Levy's motion normal distribution, is multiplied by the Prey in the step equation. As the remaining 50% of the population is up

$$\overrightarrow{Step_\iota} = \overrightarrow{R_B} \otimes \left(\left(\overrightarrow{R_B} \otimes \overrightarrow{Elite_\iota}\right) - \overrightarrow{Prey_\iota}\right) \quad (III.5)$$

$$\overrightarrow{Prey_\iota} = \overrightarrow{Elite_\iota} + \left(P.CF \otimes \overrightarrow{Step_\iota}\right) \quad (III.6)$$

Where RB and CF multiply the Elite matrix to get the following result:

$$CF = [1 - (1./MaxIter)]^{\left(\frac{2Iter}{MaxIter}\right)} \quad (III.7)$$

[4] Phase 3, the final third of iterations: The Prey matrix is updated as follows, and the predator moves using Levy motion, which is calculated by multiplying the Elite matrix by RL:

$$\overrightarrow{Step_\iota} = \overrightarrow{R_L} \otimes \left(\left(\overrightarrow{R_L} \otimes \overrightarrow{Elite_\iota}\right) - \overrightarrow{Prey_\iota}\right) \quad (III.8)$$

$$\overrightarrow{Prey_\iota} = \overrightarrow{Elite_\iota} + \left(P.CF \otimes \overrightarrow{Step_\iota}\right) \quad (III.9)$$

[5] Finalizing: The best solutions are constantly added to the Elite matrix following each iteration. Once the maximum number of iterations is reached, the final solution with the best fitness function will become apparent.

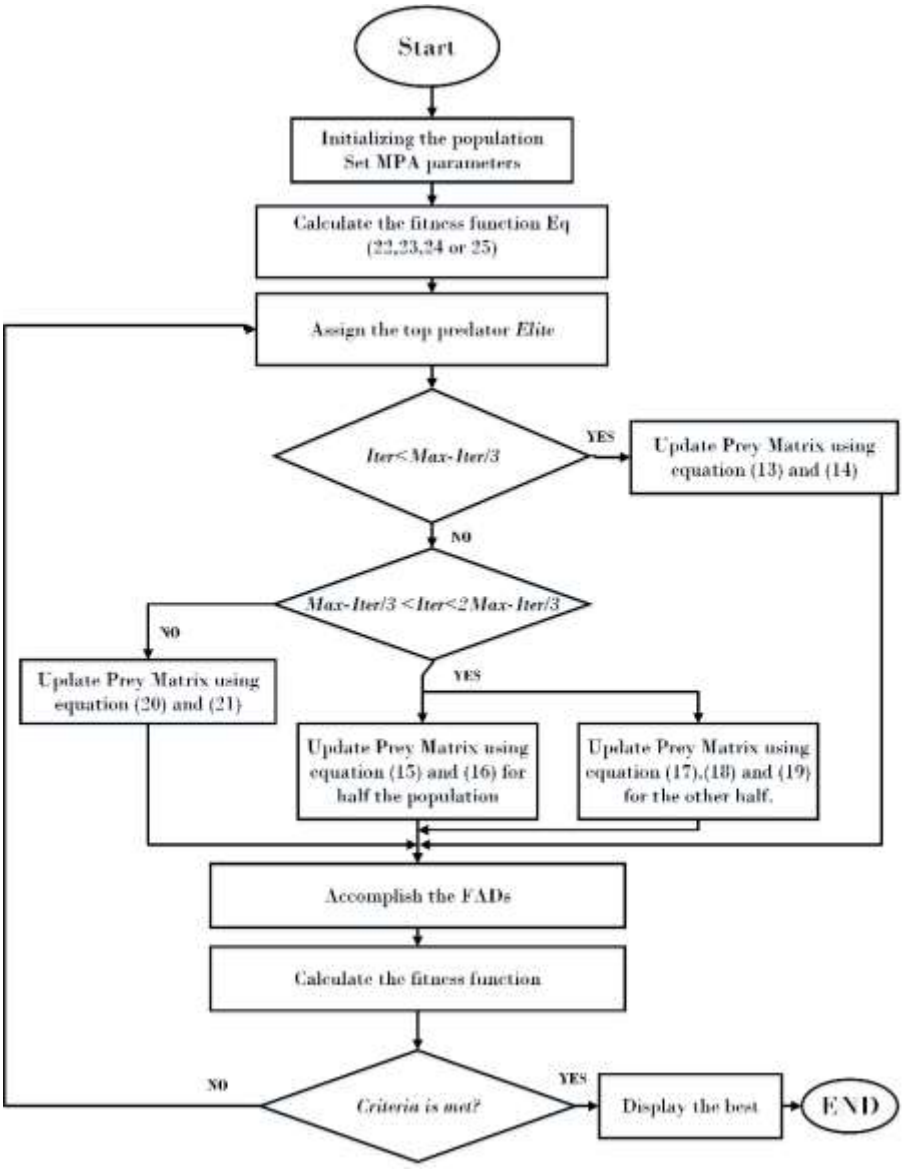

Figure III-5: MPA flow chart.

III.3.2 Fitness function

In order to reduce the error signal, specifically low-frequency oscillations (LFOs), a distinct cost function has been adopted for comprehensive analysis. The integral of time-weighted absolute error (ITAE) and the integral time square error (ITSE) are utilized as time domain cost functions to gauge performance. Additionally, two other cost functions, denoted as F1 and F2, are employed.

$$ITAE = \int_0^{Ts} t \times |e(t)dt| \qquad (III.10)$$

$$ITSE = \int_0^{Ts} t \times e(t)^2 dt \qquad (III.11)$$

F1 and F2 are two cost functions that have been adapted from [5] and [13] respectively. Both of these formulations involve considering the eigenvalues of the system, which are essentially the "natural frequencies" of its dynamic response. By adjusting crucial parameters such as damping ratios, damping factors, and frequency parameters, these cost functions aim to achieve a specific outcome: As illustrated in Figure III_6, the eigenvalues are moved to the left half of the complex s-plane. Complex numbers in the left half plane decay over time, with time, indicating a damped and steady system response, and this displacement indicates increased stability.

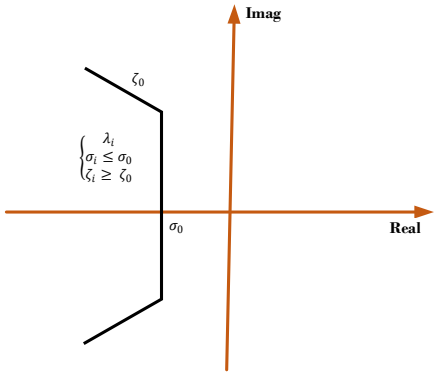

Figure III-6: D-shape schema.

$$F1 = \sum_{i=1}^{N} (\sigma_0 - \sigma_i)^2 + \sum_{i=1}^{N} (\xi_0 - \xi_i)^2$$
$$with\ \ \sigma_i \geq \sigma_0\ and\ \xi_i \leq \xi_0 \qquad (III.12)$$

N is the number of eigenvalues. ξi represents the damping ratio of the ith Eigen value, while σi represents the real part/damping factor of the ith Eigen value. ξ0 and σ0 represent the desired damping ratio and damping factor, respectively Set ξ0=-2 and σ0=0.5.

In the case of F1, the first part of this objective function focuses on maximizing the real part of the eigenvalue, while the second part aims to maximize the damping ratio. This strategy shifts the eigenvalues towards the left half of the S-plane, enhancing stability by ensuring larger negative real parts with higher damping ratios.

$$F2 = max\{|\lambda_i|, \lambda_i \in EMs\} + P_c \sum \{real(\lambda_j) | \lambda_j > 0\}$$
$$EMs = \left\{\lambda_k \middle| 0 < f = \frac{im(\lambda_k)}{2\pi} < 3\right\} \qquad (III.13)$$

λi represent the eigenvalues and P_c penalty constant.

For F2, its primary objective is to maximize the eigenvalues within the frequency range of 0 to 3. The first part of the objective function specifically targets the enhancement of the real part of eigenvalues falling within this frequency band. The second part applies a penalty to any positive eigenvalues, which indicate instability, ensuring these solutions are avoided during the optimization process.

Finally, the optimal tuning of the PSS parameters can be formulated on an optimization problem as follows:

$$\min \text{ [ITAE, ITSE, F1 or F2 } (K_{pssi}, T_{1i}, T_{2i}, T_{3i}, \text{ and } T_{4i})] \qquad (III.14)$$

Subject to:

$$\begin{cases} 0.01 \leq K_{pssi} \leq 50 \\ 0.001 \leq T_{1i} \leq 1 \text{ and } 0.001 \leq T_{3i} \leq 1. \\ 0.02 \leq T_{2i} \leq 1 \text{ and } 0.001 \leq T_{4i} \leq 1. \end{cases} [41]$$

III.4 Simulation and Results

The MATPOWER toolbox was utilized in this study to calculate the system's power flow and beginning conditions. However, MATLAB/SIMULINK was used for performing out the model's dynamic simulation. The parameters of the PSS are tuned using PSO, WOA, WHO, FPA, AVOA and MPA optimization algorithms to enhance the stability quality under three phase symmetrical fault condition. The transient performance of the PSS is evaluated based on indices such as settling time, Eigenvalues, damping ratios and Eigen plots.

III.4.1 Test System 1

Figure III_8 displays the simulation results of the stability analysis that was done on the SMIB system. The enhancement in stability that were achieved by applying several objective functions (F1, F2, ITAE, and ITSE) for MPA, PSO, WOA, FPA, AVOA, and WHO optimizers. Table III_1 presented the PSS's optimal parameter values on the SMIB system.

The simulation results for the rotor speed subjected to four objective function tuning (ITAE, ITSE, F1 and F2) are shown in Figure III.8 (a)–(d), respectively.

Figure III_9's bar chart is used to offer a quantitative analysis based on the settling times of the various controllers examined in this article.

Table III_2 presents the stability analysis using Eigenvalues and the damping of the electromechanical modes based the four objective function tuning (ITAE, ITSE, F1 and F2).

Table III-1: PSS's optimal parameter values on the SMIB system.

		PSS PARAMETERS				
Cost fun	Controller	KG	T1	T2	T3	T4
F1	MPA-PSS	33.570	0.123	0.020	0.083	0.02
	PSO-PSS	3.186	0.653	0.02	0.641	0.448
	WOA-PSS	7.471	0.0924	0.020	0.406	0.0740
	FPA-PSS	24.031	0.433	0.999	0.503	0.020
	AVOA-PSS	5.706	0.467	0.0245	0.527	0.360
	WHO-PSS	3.170	0.477	0.020	0.940	0.480
F2	MPA-PSS	50	0.094	0.02	0.098	0.02
	PSO-PSS	6.549	0.497	0.02	0.4612	0.419
	WOA-PSS	6.352	0.099	0.054	0.418	0.048
	FPA-PSS	3.611	0.865	0.02	0.949	0.946
	AVOA-PSS	40.783	0.088	0.02	0.104	0.02
	WHO-PSS	5.048	0.321	0.229	0.438	0.02
ITAE	MPA-PSS	49.915	0.083	0.02	0.084	0.02
	PSO-PSS	16.798	0.466	0.556	0.436	0.02
	WOA-PSS	15.0120	0.322	0.02	0.042	0.02
	FPA-PSS	47.541	0.207	0.02	0.038	0.02
	AVOA-PSS	32.315	0.151	0.02	0.048	0.020
	WHO-PSS	23.110	0.538	0.999	0.522	,0.020
ITSE	MPA-PSS	49.999	0.083	0.020	0.111	0.020
	PSO-PSS	45.840	0.382	0.020	0.653	0.490
	WOA-PSS	50	1	0.020	0.539	1
	FPA-PSS	50	0.0510	0.020	0.110	0.020
	AVOA-PSS	50	0.723	0.527	0.369	0.020
	WHO-PSS	50	0.495	0.020	0.520	0.507

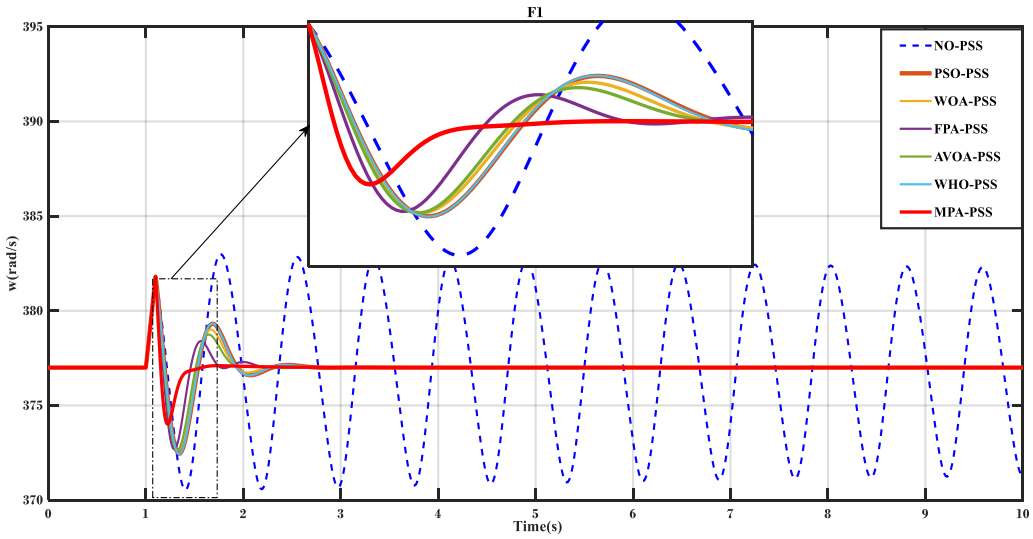
F1
NO-PSS
PSO-PSS
WOA-PSS
FPA-PSS
AVOA-PSS
WHO-PSS
MPA-PSS
w(rad/s)
Time(s)

(a)

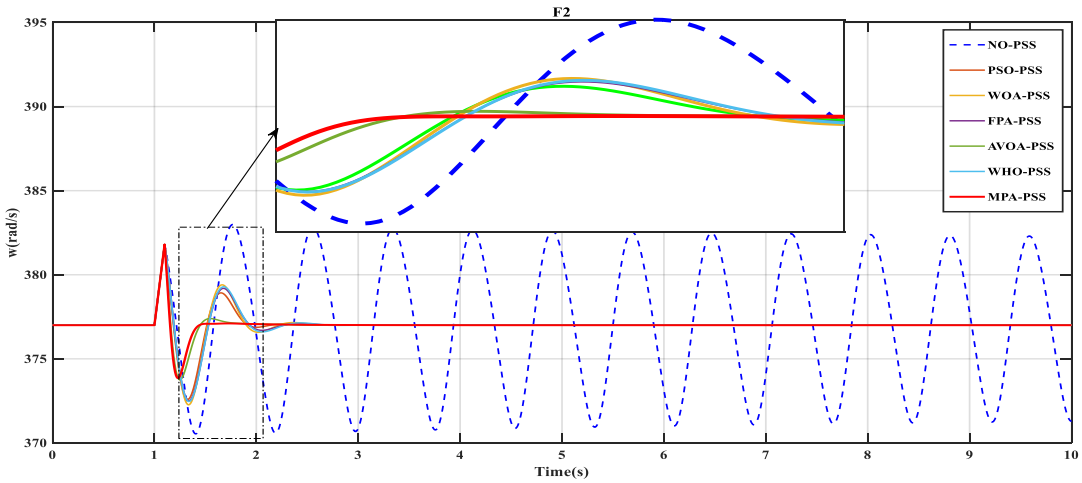
F2
NO-PSS
PSO-PSS
WOA-PSS
FPA-PSS
AVOA-PSS
WHO-PSS
MPA-PSS
w(rad/s)
Time(s)

(b)

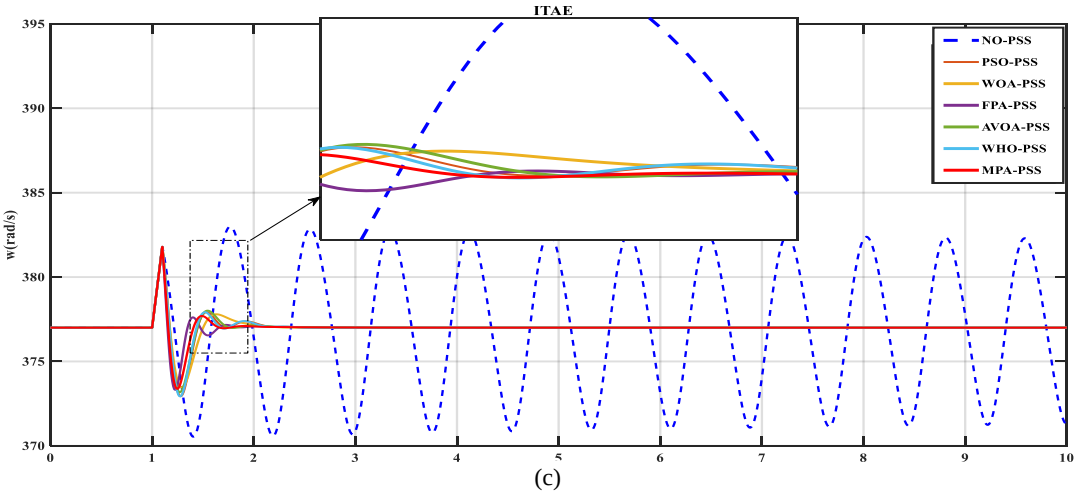
ITAE
NO-PSS
PSO-PSS
WOA-PSS
FPA-PSS
AVOA-PSS
WHO-PSS
MPA-PSS
w(rad/s)

(c)

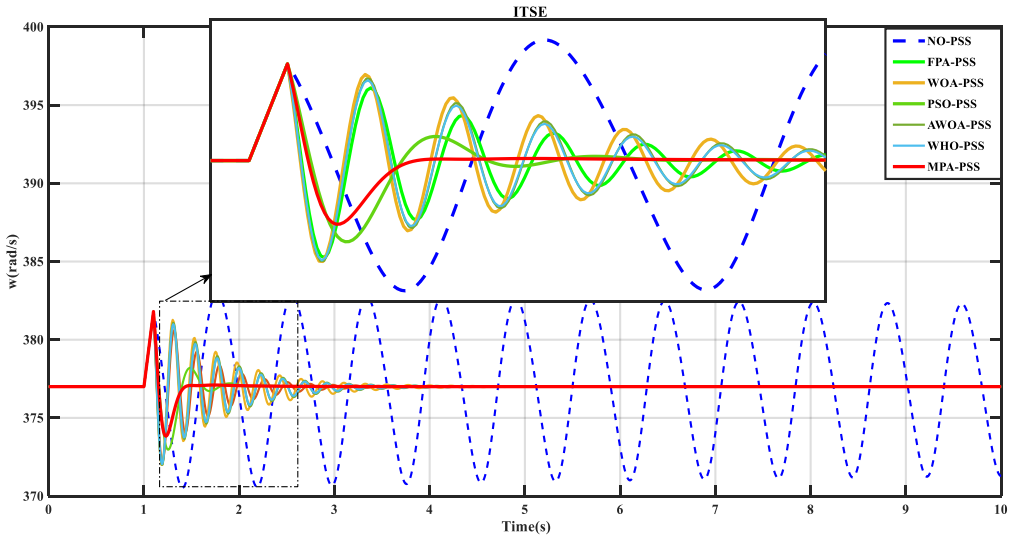

(d)

Figure III-8: Simulation results of rotor speed in SMIB for different cost function and their zoom. (a): F1, (b): F2, (c): ITAE, (d): ITSE.

Figure III_8 illustrates that without PSS, the system lacks adequate damping, which hinders its ability to settle. However, the incorporation of PSS enhances the system's damping. The performance of the MPA-PSS, as demonstrated in Figure III_8 (a)-(d), is noteworthy. It maintains satisfactory performance indices even when the fitness function changes. In comparison to the PSS optimized by PSO/WOA/FPA/AVOA/WHO, the MPA-PSS minimizes the minimum undershoot, and settling time, thereby showcasing its superior performance.

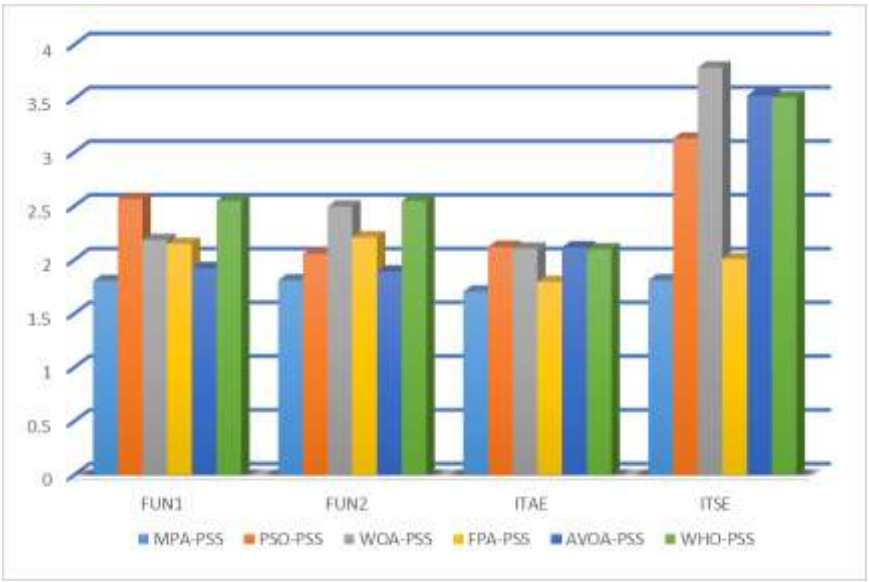

Figure III-9: Statistical comparison of performance settling time for different controllers subjected to different cost function.

Table III_2 shows that a single pair of eigenvalues without PSS has a negative damping ratio and falls in the unstable area of the s-plane. It is clear that PSS causes the electromechanical modes to move to the left of the S-plane and greatly increases the damping factor values. In comparison to PSS optimized PSO/WOA/FPA/AVOA and WHO approaches, MPA-PSS moves the eigenvalues further from the selected D-shape stable area in the s-plane with superior damping performance.

The eigenvalues plot analysis of the SMIB system with No-PSS, MPA-PSS, PSO-PSS, WOA-PSS, FPA-PSS, AVOA-PSS, and WHO-PSS subjected to the F1, F2, ITAE, and ITSE objective functions is depicted in Figure III_10. The MPA demonstrates its performance across all four cost function tests, with the most significant shifts in eigenvalues observed with the ITSE and F2 objective functions.

Table III-2: Eigen values and damping ratio comparison for various controllers and cost functions

Controllers	**(**Eig, Damping ratio**)**	**F1**	**F2**	**ITAE**	**ITSE**
NO-PSS	*Eig*		0.0588 ±8.3601i		
	Damping ratio		*-0.0070*		
MPA-PSS	*Eig*	*-12.8827* *±11.629i* *-8.5675 ± 7.4138i*	*-11.2513 ±* *18.096i* *-9.9918 ± 4.5219i*	-7.1754 ±14.5639i	-10.9665 ±18.1205i -9.9436 ± 3.4524i
	Damping ratio	*0.7423* *0.7562*	*0.5280* *0.9110*	0.4420	0.5178 0.9447
PSO-PSS	*Eig*	-4.7732±7.9261i -4.7926 ± 7.8676i	*-4.6874 ±* *10.6114i* *-4.7045 ± 5.6666i*	-4.6652 ± 14.677i -3.8899 ± 3.8955i	-2.0239 -26.3537i -1.8283±1.6911
	Damping ratio	*0.5159* *0.5202*	*0.4041* *0.6388*	0.3029 0.7066	0.0766 0.7341
WOA-PSS	*Eig*	-5.9803±8.9791i -4.7710 ± 7.7116i	*-4.9472 ± 9.2219i* *-4.9472 ± 8.1246i*	-7.3356 ± 12.466i -4.5116 ± 4.9554i	-1.5437 ± 27.8950i -1.6764 ± 1.7424i
	Damping ratio	*0.5543* *0.5261*	*0.4727* *0.5201*	0.5072 0.6732	0.0553 0.6933
FPA-PSS	*Eig*	-4.3271±13.4399i -4.5978 ±4.2302i	*-4.7429 ± 9.2850i* *-4.7761 ± 6.6103i*	-6.1136 ± 19.507i -4.8103 ± 2.563i	-5.0878 ± 14.9303i
	Damping ratio	*0.3065* *0.7359*	*0.4549* *0.5857*	0.2991 0.8825	0.3226
AVOA-PSS	*Eig*	-4.7952±11.4727i -4.0076 ±5.3550i	*-10.9568±13.546i* *-10.9568 ± 6.314i*	-5.6822 ± 13.051i -7.2047 ± 3.2506i	-1.6638 ± 27.2003i -1.7388 ± 1.5019i
	Damping ratio	*0.3856* *0.5992*	*0.6289* *0.8664*	0.3991 0.9115	0.0611 0.7568
WHO-PSS	*Eig*	*-4.2128±8.6271i* *-5.3744± 7.0621i*	*-4.8126 ± 8.4689i* *-4.8023 ± 7.6017i*	-4.5859 ±15.0672i -3.8534 ± 3.8221i	-1.7446 ± 27.2493i -1.7832 ± 1.7505i
	Damping ratio	*0.4388* *0.6056*	*0.4941* *0.5341*	0.2912 0.7100	0.0639 0.7136

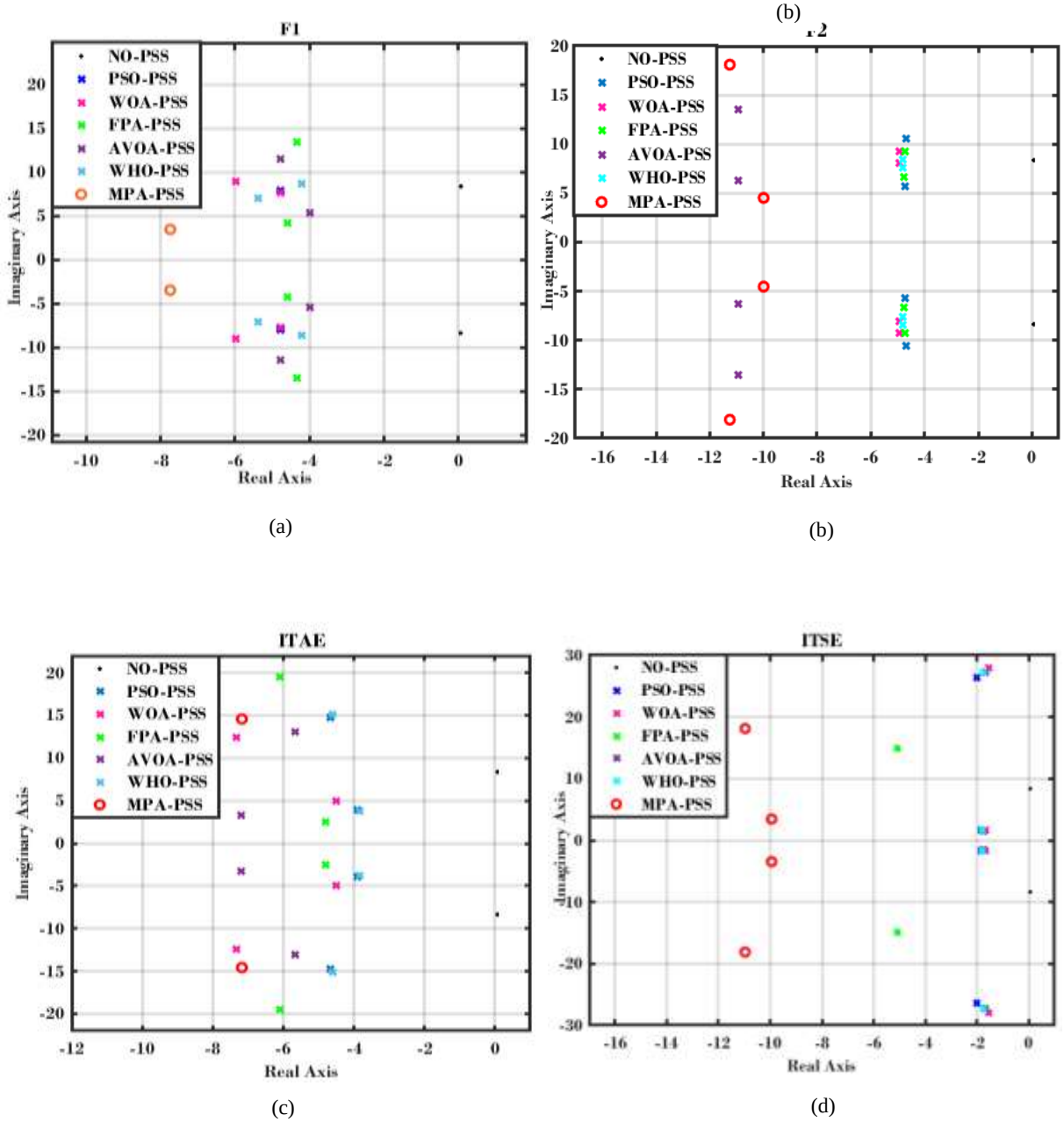

Figure III-8: Simulation results of Eigen plots for different cost function. (a): F1, (b): F2, (c): ITAE, (d): ITSE.

III.4.2 Test system 2

Table III_3 illustrates the various operating conditions under which the study was carried out using a base value of 100 MVA per unit. The optimal PSS values were found utilizing earlier metaheuristic optimizers for generators (G2 and G3). The corresponding rotor speed of generators G1, G2, and G3 for normal loading, heavy loading and light loading are shown in Figure III.12(a)–(c), Figure III. 13(a)–(c) and Figure III. 14 (a)–(c), respectively.

Eigenvalues analysis simulation was run under symmetrical three-phase fault at bus 9 at the end of line 8–9 observed at t = 1 s for different operating conditions.

Figure III. 12(a)-(c) illustrates the rotor speed of generators G1, G2, and G3 respectively for normal loading. It is noteworthy that G3 experiences more pronounced oscillations in rotor speed compared to G1 and G2, which can be attributed to the influence of the fault. However, it is crucial to acknowledge that the fault also impacts G1 and G2. This demonstrates the effect of a fault in one region on the others, indicative of interarea oscillations.

Table III-3: Operating conditions for the WSCC test system

Normal Loading		Heavy Loading		Light Loading	
P_L(pu)	Q_L(pu)	P_L(pu)	Q_L(pu)	P_L(pu)	Q_L(pu)
1.25	0.5	2	0.8	0.65	0.55
0.90	0.3	1.8	0.6	0.45	0.35
1.00	0.35	1.5	0.6	0.50	0.25

On the comparison of metaheuristic techniques, it's noticeable that that rotor speed for all generators with MPA-PSS show fast decaying of oscillations, settling fast therefore better stability response. To further substantiate the stability of the MPA-based PSS, we modified the operating conditions from those specified in Table III.3.

From figure.III 13(a)-(c), it's observable that with an increase in load (heavy loading), there's a corresponding increase in both the amplitude and duration of oscillations in all three generators, thereby making the attainment of a stable state more challenging. Furthermore, it is noticed that rotor speed for all generators with MPA-PSS performs better results in term of damping and return to reverting to a stable state. The system responses under Light loading condition are shown in figure III. 14(a)-(c),. The superiority of the MPA-PSS in reducing the settling time and suppressing power system oscillations is verified.

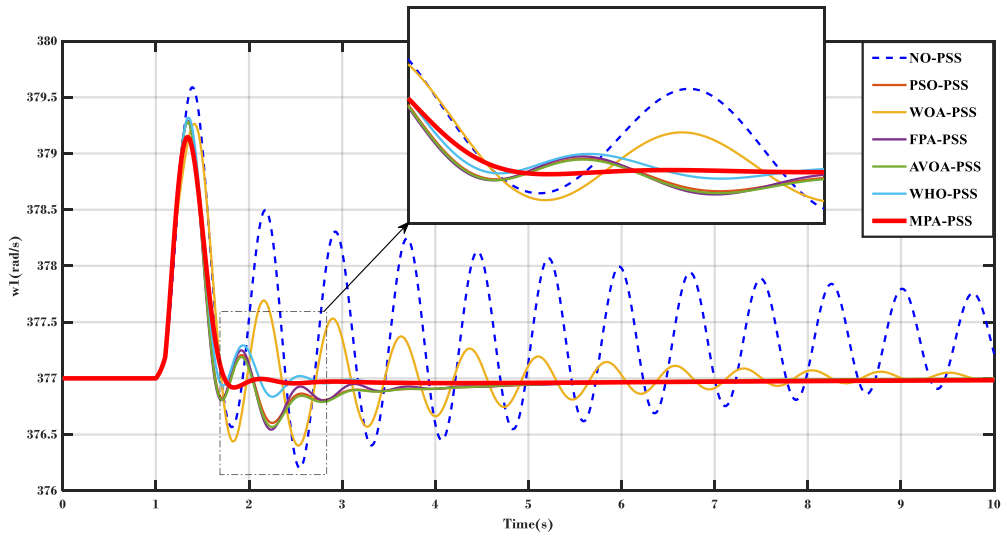

(a)

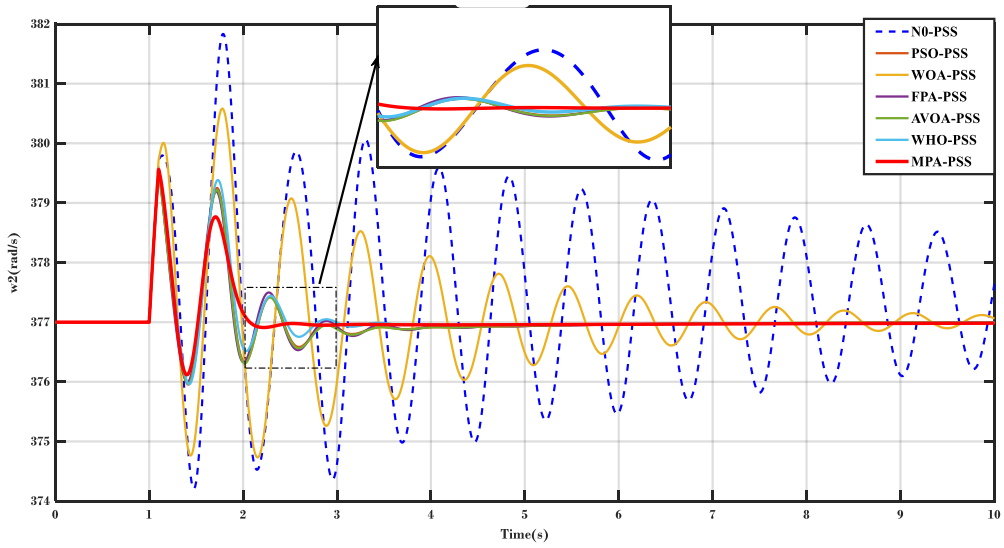

(b)

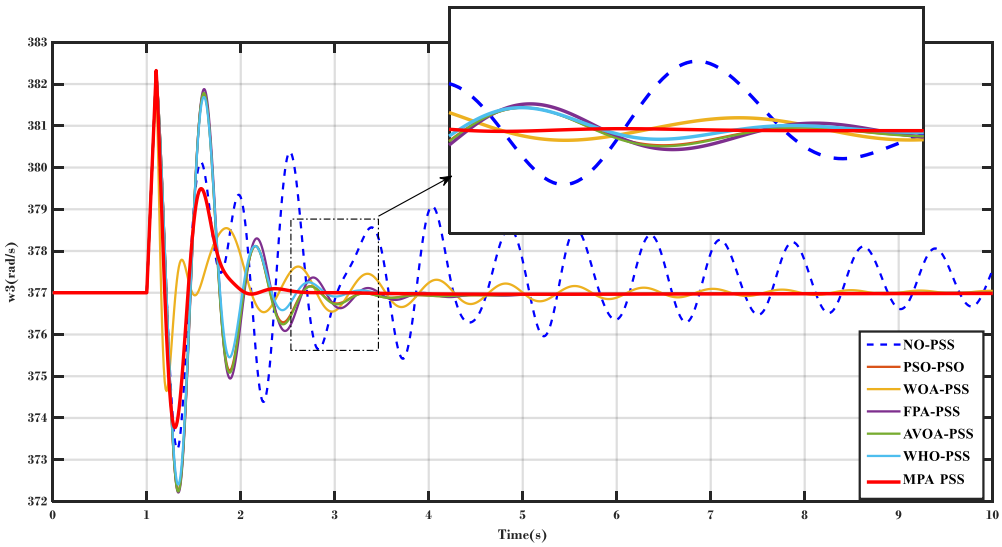

(c)

Figure III-9: Normal loading, time domain simulation for rotor speed of generators G1, G2, and G3. (a): w1, (b): w2, (c): w3.

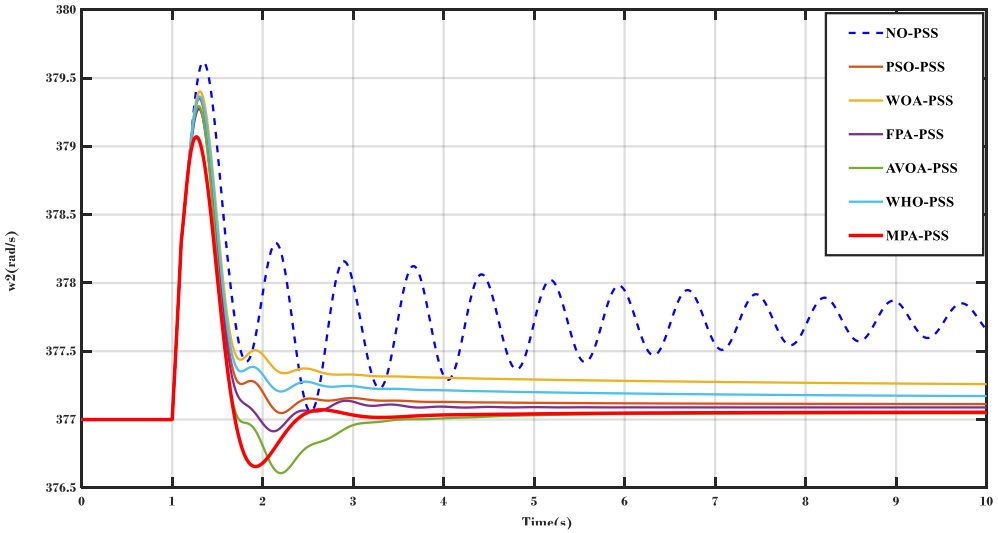

(a)

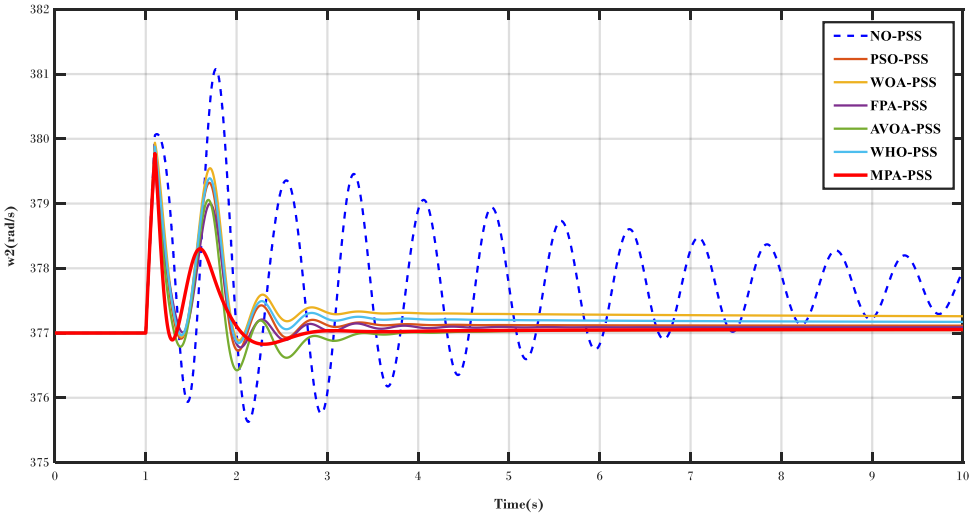

(b)

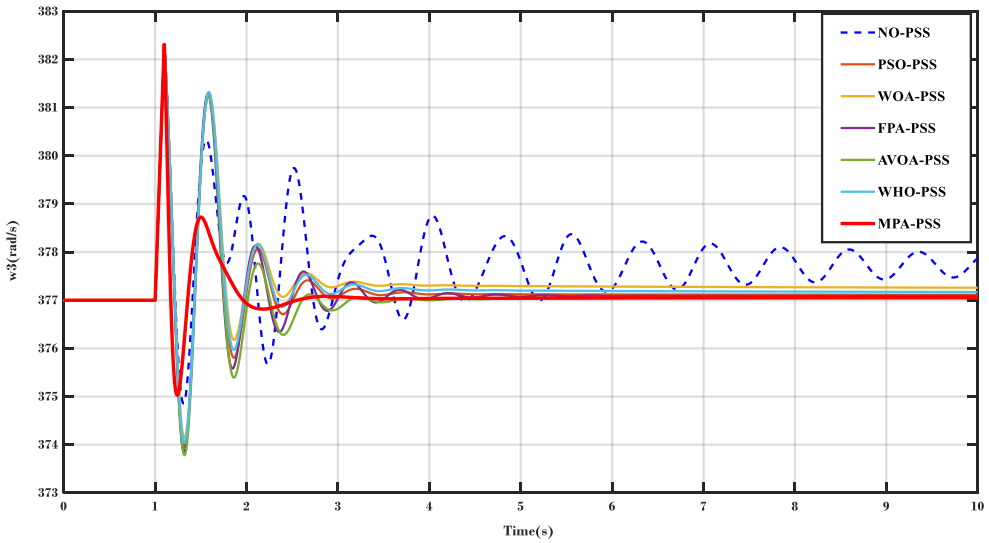

(c)

Figure III-10: Heavy loading, time domain simulation for rotor speed of generators G1, G2, and G3. (a): w1, (b): w2, (c): w3.

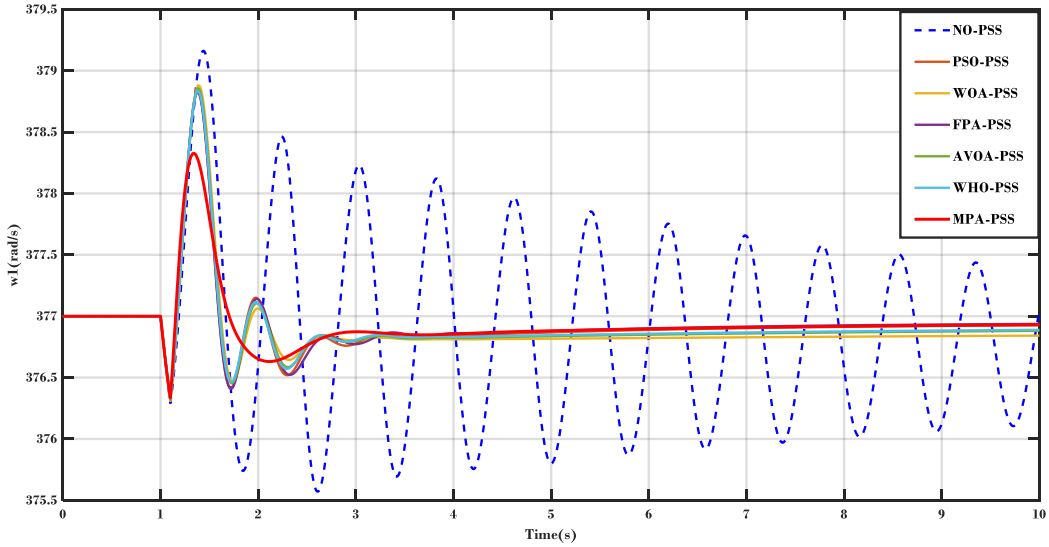

(a)

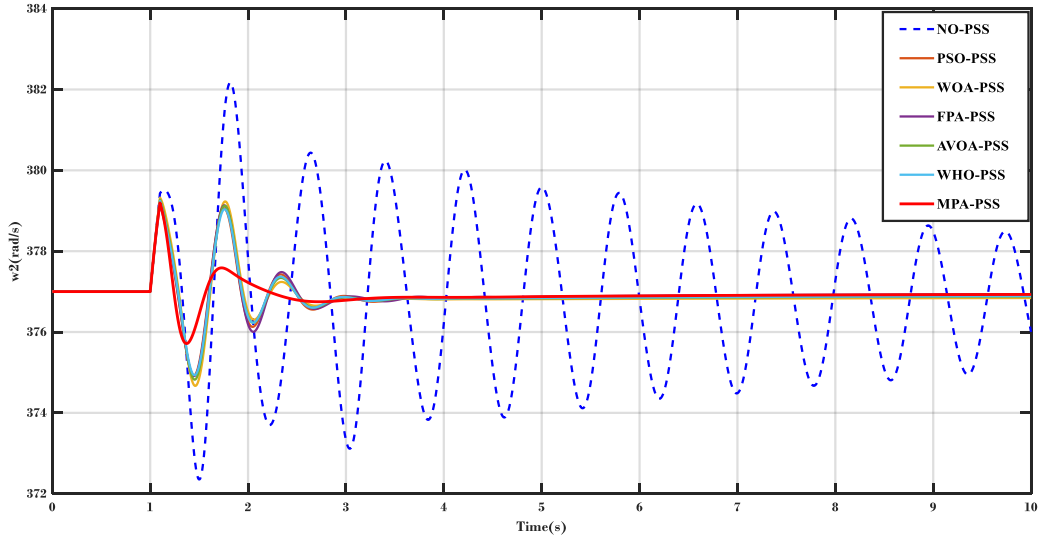

(b)

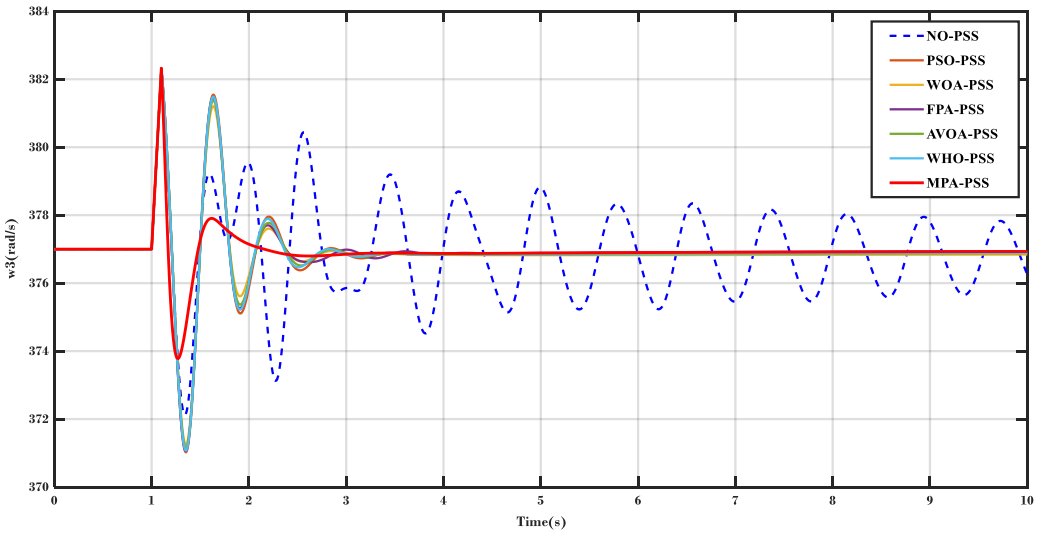

(c)

Figure III-11: Light loading, time domain simulation for rotor speed of generators G1, G2, and G3. (a): w1, (b): w2, (c): w3.

Figure III.15(a)-(c) presents bar charts comparing the performance index settling time of various stabilizers, PSO, WOA, FPA, AVOA, WHO, and MPA-PSS, under three different load conditions. The charts almost demonstrate that the MPA-PSS outperforms the other stabilizers across various operating points. The bar chart evidently shows that the system requires a longer duration to return to a stable state under heavy and light load conditions, as compared to normal load conditions.

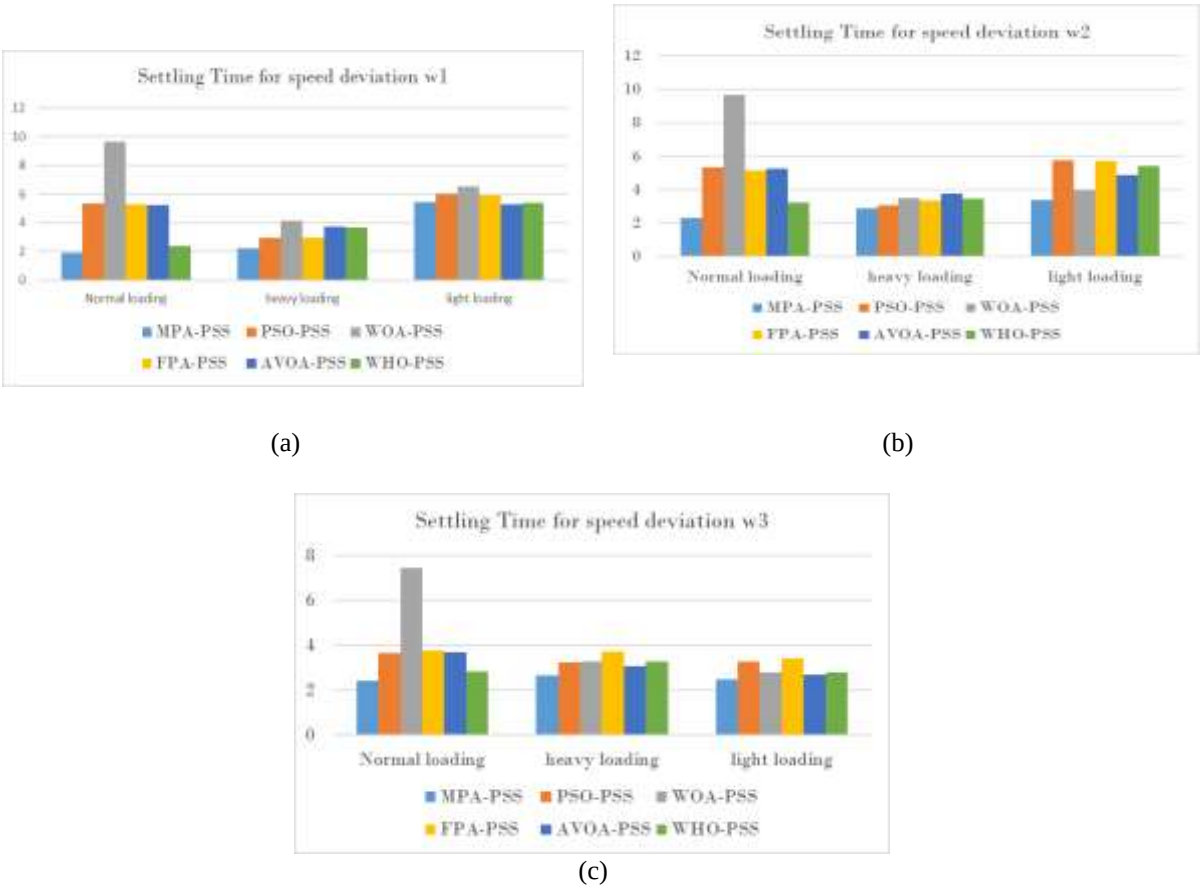

Figure III-12 : Comparison of performance indices settling time for rotor speed of generators G1, G2, and G3. (a): w1, (b): w2, (c): w3 under three different operating point.

Table III.4 shows the eigenvalues analysis of the WSCC System. It has two local area eigenvalues and three interarea eigenvalues. Without a PSS, the system is close to becoming unstable. This is shown by the interarea eigenvalues, which are near zero in normal, heavy, and light load conditions. This makes the system likely to become unstable if there are disturbances. The introduction of a PSS, however, significantly alters the system dynamics. It effectively shifts both local and interarea electromechanical modes to the left of the S-

plane, thereby enhancing system stability. Among the various PSS optimization techniques, the MPA stands out. It relocates the eigenvalues far from the selected D-shape stable region in the s-plane, thereby demonstrating superior damping performance. This improvement is notably superior when compared to other PSS tuned other optimization techniques such as PSO, WOA, FPA, AVOA, and WHO.

Table III-4: Eigenvalues Analysis of the PSS based PSO, WOA, WHO, FPA, AVOA and MPA optimization techniques for Three Loading Cases of WSCC System

	Eigenvalues					
	Normal Loading		Heavy Loading		Light Loading	
Contro-llers	Local area	Inter area	Local area	Inter area	Local area	Inter area
NO-PSS	-0.6856±12.775i 0.1229±8.2867i	-2.3791±2.617i -4.6706±1.375i -3.5199±1.015i	-0.8948 ±12.5987i -0.2046 ± 8.3076i	-2.5388 ±2.411i -4.2545±1.432i -3.0828 ±1.26i	-0.6708±12.77i -0.0936±8.011i	-2.3685 ±2.793i -4.6969 ± 1.361i -3.5279 ±1.018i 3.63e-16±3.4e8i
MPA-PSS	-5.0969±13.76i -3.9664 ±7.697i	-3.9450±2.487i -3.9126±2.336i -3.9048±2.310i	-4.6491±13.5438i -8.6557 ± 9.2369i	-2.8956 ± 4.129i -3.9238 ± 1.810i -2.8630±1.5121i	-7.2260±9.214i	-1.9968 ±3.5767i -4.3064±2.0697i -3.2997 ±1.3202i
PSO-PSS	-2.6645 ±11.28i -2.9276 ±11.24i	-2.3169 ±3.04i -4.616 ±1.557i -3.421 ± 1.123i	-2.0665 ±11.8134i -4.0967±10.5081i	-3.0071 ± 3.420i -4.0495 ± 1.697i -2.9072 ± 1.516i -0.0001±0.0001i	-2.8603±12.18i -2.3506±10.02i	-2.1069±3.0319i -4.6487± 1.4224i -3.3475± 0.9302i -0.0001±0.0001i
WOA-PSS	-0.4066±8.5526i -0.4066±8.5526i	-2.7810 ±3.00i -3.5935±2.390i -3.696 ± 1.029i	-2.2939 ±12.0427i -3.9926 ±10.7250i	-3.6344±4.6774i -3.755 ± 1.5608i -2.7876 ± 1.797i -0.0001±0.0001i	-2.921±12.355i -3.1032±10.00i	-2.5761±3.3218i -4.5059 ±2.0462i -3.5818 ±1.3878i
FPA-PSS	-3.6646±13.081i -1.7314±10.782i	-2.1782± 3.17i -4.5407 ±1.49i -3.1835±1.020i	-1.4247 ±11.9148i -3.8398 ±8.1194i	-2.4936 ± 3.311i -4.1246 ± 1.477i -2.7360±1.3661i	-2.0259±12.44i -1.9895±9.455i	-1.9812 ±2.9539i -4.5364 ±1.2891i -2.7351 ±0.5555i
AVOA-PSS	-2.7512+11.236i -2.7476±11.236i	-2.2379±3.029i -4.6044±1.489i -3.3727±1.040i	-2.0077 ±11.7191i -3.5466±10.3067i	-2.2895 ± 2.963i -4.1855 ± 1.489i -2.9137±1.2023i	-2.8809±12.35i -2.615±10.04i	-2.2700 ±3.2151i -4.6045±1.6524i -3.4066 ±1.1928i -0.0001 ±0.0001i
WHO-PSS	*-2.5634±11.733i* *-3.3037±11.123i*	*-3.0399±3.483i* *-3.9230±1.613i* *-3.5689 ±2.00i*	*-2.0373 ±11.8982i* *-4.2707 ±10.5681i*	*-3.3588 ± 4.179i* *-3.7982 ± 1.632i* *-2.8560±1.7190i*	*-2.7379±12.01i* *-2.6995±10.06i*	*-2.1177± 3.1599i* *-4.5879± 1.4480i* *-3.1944± 0.9426i* *-0.0001±0.0001i*

An in-depth analysis of the participation factors (Pf) of the state variables (Sv) for the WSCC power system in two different configurations—one without a power system stabilizer (NO-PSS) and the other with a number of optimized PSS algorithms, including MPA-PSS, PSO-PSS, WOA-PSS, FPA-PSS, AVOA-PSS, and WHO-PSS—is given by the results in Tables III. 5 and III.6. A comprehensive examination of the impact of every state variable on the critical modes of the system is made possible by this comparative analysis of participation factors. Analyzing these variables makes it possible to evaluate how well each PSS technique enhances system stability.

Comparing the MPA-PSS to other algorithms and the no-PSS configuration, the analysis of the participation factors (Pf) in both local-area and inter-area modes shows that the MPA-PSS performs better at improving system stability.

In the local-area mode, without a PSS, critical state variables such as rotor speeds and rotor angles for the generators (e.g., $\omega 3$ and Delta3) exhibit high participation factors (e.g., 0.36547 for both $\omega 3$ and Delta3), indicating poor control over local oscillations. However, with the implementation of the MPA-PSS, the participation factors for these variables are drastically reduced to as low as 0.0146 and 0.0069, respectively. This sharp reduction demonstrates the MPA-PSS's superior ability to damp local oscillations, significantly improving stability compared to other algorithms such as PSO-PSS, which still shows higher Pf values (e.g., 0.25828 for $\omega 3$), indicating less effective control.

In the inter-area mode, the no-PSS scenario again exhibits high participation factors, particularly for variables such as the transient EMF (e.g., $\boldsymbol{E'_{q1}}$ with a Pf of 0.17103). The MPA-PSS, however, reduces these factors considerably (e.g., Pf of 0.0449 for Delta2 and 0.0438 for $\boldsymbol{E'_{q2}}$), highlighting its effectiveness in mitigating inter-area oscillations. In contrast, other PSS algorithms like PSO-PSS and WOA-PSS display higher participation factors, indicating less damping of critical inter-area modes.

Table III-5: Table 6: State Variables of the WSCC Power System.

1	Rotor angle for G1 “Delta1”
2	Rotor angle for G2 “Delta2”
3	Rotor angle for G3 “Delta3”
4	Rotor speed for G1 “$\omega 1$”

5	Rotor speed for G2 "$\omega 2$"
6	Rotor speed for G3 "$\omega 3$"
7	the transient EMF of the d-axis for G1 E'_{d1}
8	the transient EMF of the d-axis for G2 E'_{d2}
9	the transient EMF of the d-axis for G3 E'_{d3}
10	the transient EMF of the q-axis for G1 E'_{q1}
11	the transient EMF of the q-axis for G2 E'_{q2}
12	the transient EMF of the q-axis for G3 E'_{q3}
13	the excitation field voltage of G1 "Efd1"
14	the excitation field voltage of G2 "Efd2"
15	the excitation field voltage of G3 "Efd3"

Table III-6 : "Comparative Analysis of Participation Factors for Different PSS Configurations

NO-PSS						
LOCAL-AREA	-0.6856±12.77i	Sv	6	3	5	2
		Pf	0.36547	0.36547	0.079926	0.079926
	0.1229±8.2867i	Sv	5	2	1	4
		Pf	0.26659	0.26659	0.13424	0.13424
INTER-AREA	-2.3791±2.617i	Sv	10	13	11	12
		Pf	0.17103	0.14145	0.088681	0.076538
	-4.6706±1.375i	Sv	15	9	8	14
		Pf	0.22621	0.22396	0.13762	0.093983
	-3.5199±1.015i	Sv	13	8	14	10
		Pf	0.23974	0.22262	0.20474	0.14064
MPA-PSS						
LOCAL-AREA	-5.0969±13.76i	Sv	3	6	21	20
		Pf	0.014616	0.0068611	0.002413	0.0023936
	-3.9664±7.697i	Sv	3	6	5	1
		Pf	0.0080086	0.0033814	0.0021951	0.0019524
I N	-3.9450±2.487i	Sv	2	11	18	14

		Pf	0.044947	0.044758	0.043803	0.043775
	-3.9126±2.336i	Sv	8	15	9	14
		Pf	0.24979	0.24908	0.24905	0.24851
	-3.9048±2.310i	Sv	13	10	15	21
		Pf	0.21795	0.21679	0.21576	0.21445

PSO-PSS

LOCAL-AREA	-2.6645±11.28i	Sv	6	3	5	2
		Pf	0.25828	0.25815	0.22484	0.20993
	-2.9276±11.24i	Sv	5	6	3	2
		Pf	0.25426	0.23682	0.23672	0.2345
INTER-AREA	-2.3169 ±3.04i	Sv	10	13	12	15
		Pf	0.10857	0.09082	0.069078	0.061447
	-4.616 ±1.557i	Sv	15	8	9	12
		Pf	0.17296	0.091454	0.091435	0.06104
	-3.421 ± 1.123i	Sv	13	10	8	15
		Pf	0.27642	0.17536	0.16566	0.1012

WOA-PSS

LOCAL-AREA	-0.4066±8.5526i	Sv	2	5	4	1
		Pf	0.28328	0.28276	0.08463	0.08463
	-0.4066±8.5526i	Sv	2	5	4	1
		Pf	0.28328	0.28276	0.08463	0.08463
INTER-AREA	-2.7810 ±3.00i	Sv	10	13	12	15
		Pf	0.15093	0.13319	0.10784	0.09852
	-3.5935±2.390i	Sv	9	15	20	21
		Pf	0.20386	0.17263	0.14889	0.13537
	-3.696 ± 1.029i	Sv	8	14	13	11
		Pf	0.27598	0.24613	0.1758	0.13591

FPA-PSS

LOCAL-AREA	-3.6646±13.08i	Sv	5	6	3	18
		Pf	0.24456	0.17094	0.15765	0.10887
	-1.7314±10.78i	Sv	6	3	5	4
		Pf	0.27777	0.25621	0.11437	0.084419
I N	-2.1782± 3.17i	Sv	1	14	12	15

		Pf	0.10185	0.10185	0.074203	0.067821
	-4.5407 ±1.49i	Sv	15	9	12	8
		Pf	0.26594	0.20307	0.086975	0.061329
	-3.1835±1.020i	Sv	13	10	8	14
		Pf	0.28482	0.22479	0.22118	0.12025

AVOA-PSS

LOCAL-AREA	-2.7512+11.23i	Sv	5	6	3	2
		Pf	0.25006	0.24982	0.24982	0.24972
	-2.7476±11.23i	Sv	6	2	5	3
		Pf	0.2501	0.2501	0.24965	0.24936
INTER-AREA	-2.2379±3.029i	Sv	10	13	12	15
		Pf	0.047692	0.042377	0.0047149	0.0038438
	-4.6044±1.489i	Sv	15	8	12	9
		Pf	0.012413	0.0047105	0.0044985	0.0025798
	-3.3727±1.040i	Sv	13	10	8	15
		Pf	0.14223	0.084382	0.010832	0.0060458

WHO-PSS

LOCAL-AREA	*-2.5634±11.73i*	Sv	3	6	5	2
		Pf	0.26106	0.26099	0.16107	0.10966
	-3.3037±11.12i	Sv	5	3	6	2
		Pf	0.23569	0.1973	0.19725	0.15531
INTER-AREA	*-3.0399±3.483i*	Sv	4	1	11	14
		Pf	0.096741	0.096741	0.092384	0.0833
	-3.9230±1.613i	Sv	15	9	12	13
		Pf	0.25778	0.21735	0.16025	0.13395
	-3.5689 ±2.00i	Sv	13	8	10	15
		Pf	0.24339	0.22081	0.21198	0.15588

III.4.3 Test system 3

The study is carried out under symmetrical three-phase fault at bus 39 in area-1 of the MMPS at t=1sec. The optimal PSS parameters obtained for all generators except G2 is an equivalent power source.

The corresponding rotor speed in areas 1, 2 and 3 for generators G1, G4, and G10 are shown in Figure. III_16(a)–(c), respectively. Notably, area 1 experiences higher oscillations in rotor speed compared to areas 2 and 3 due to the fault's impact. However, it's essential to

recognize that the fault also affects areas 1 and 2, They represent the interarea oscillations, or how a fault in one area affects the other areas.

These results demonstrate the superior transient performance of the proposed MPA-PSS when compared with the PSO/WOA/FPA/AVOA/WHO/ optimized PSS

The eigenvalues plot illustrates in Figure III_ 17 demonstrates the instability of the system without a PSS. The eigenvalues are situated in the right half of the D shape, the instable area. However, when we integrate the PSS with an optimized metaheuristic algorithm, we observe a shift in the eigenvalues to the left side. This shift is noticeable with PSO, WOA, FPA, AVOA, and WHO. Despite this shift, the eigenvalues remain in the positive region. This suggests that these algorithms may need more than 25 population and 100 iterations to achieve a complete shift of all eigenvalues to the left side.

On the other hand, when the PSS is optimized with the Marine Predator Algorithm (MPA), all the eigenvalues, including both local and inter-area eigenvalues, are shifted to the negative part, thereby enhancing stability and demonstrating the robustness of the MPA-PSS

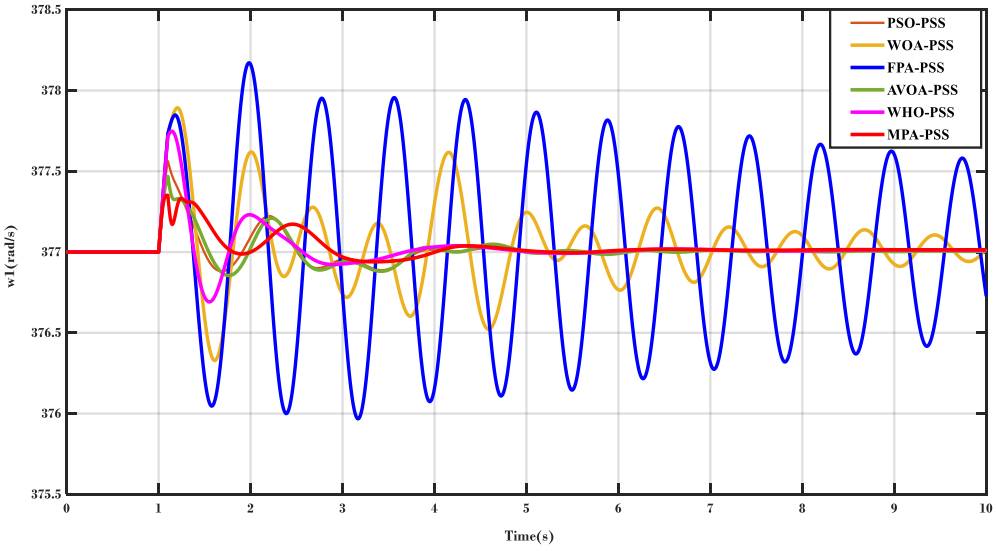

(a)

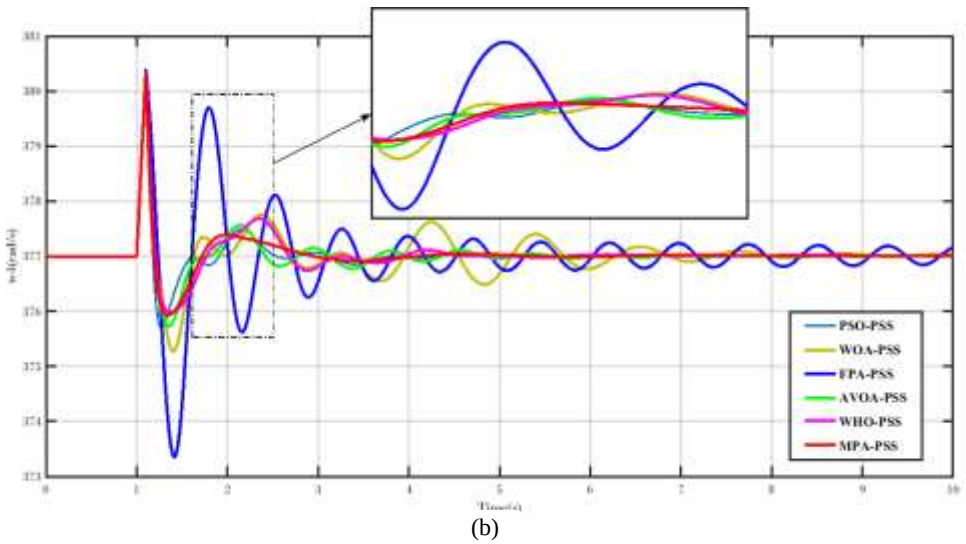

(b)

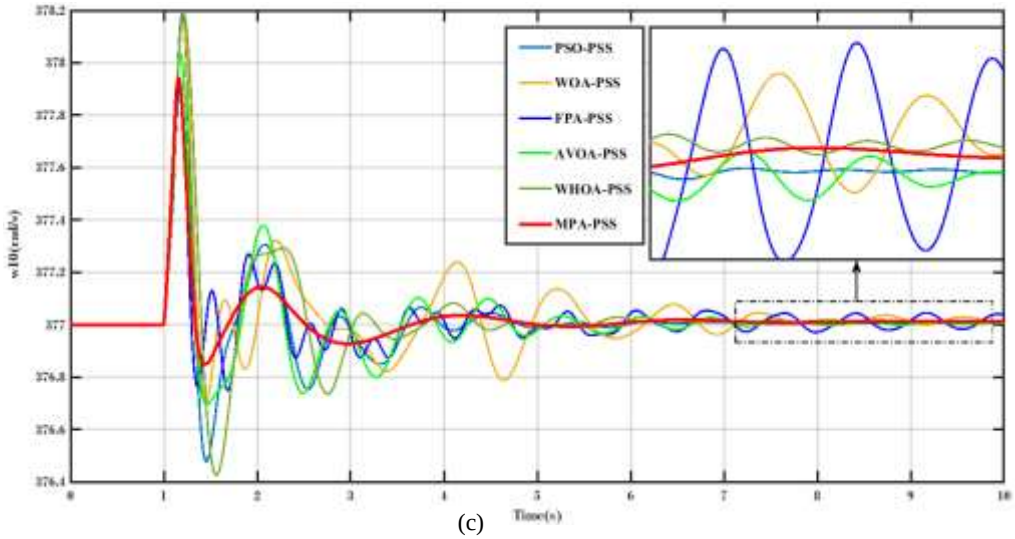

(c)

Figure III-13: Time domain simulation for rotor speed in areas 1, 2 and 3 for generators G1, G4, and G10. (a): w1, (b): w4, (c): w10.

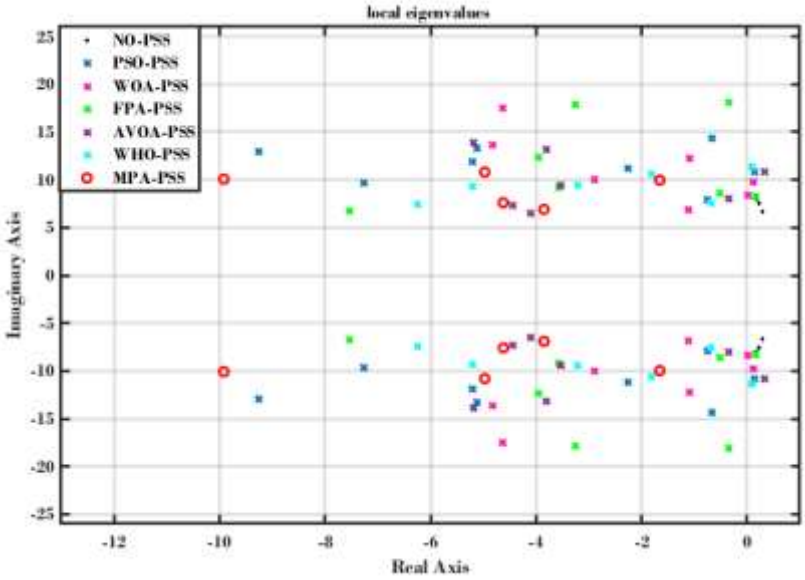

(a)

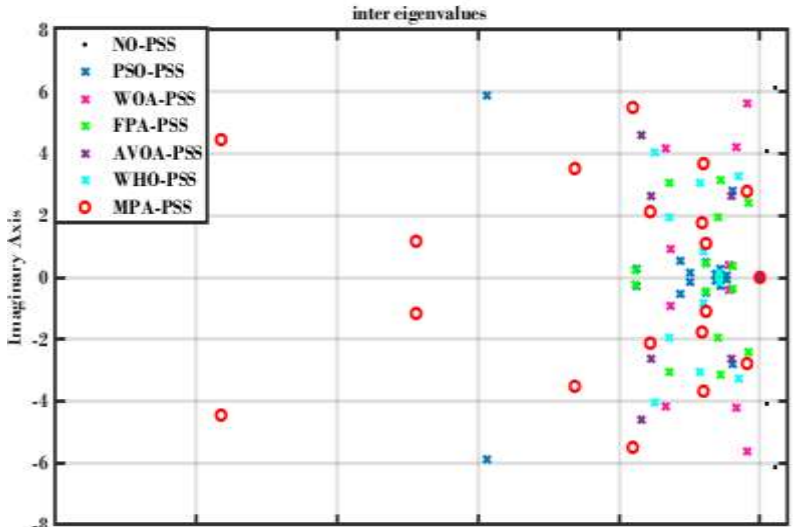

Figure III-14: Simulation results of Eigen plots for different controllers.

The results in Table III_7 and Table III_8 provide a comprehensive comparison of the participation factors (Pf) of the state variables (Sv) for the New England Power System across different configurations: without a PSS and with the MPA-PSS. The analysis highlights the influence of key state variables on local and inter-area modes in both cases.

In the NO-PSS configuration, the participation factors (Pf) show that some state variables have a significant impact on both local and inter-area modes. For example, rotor angles (Sv 10 and Sv 20) show the highest participation factor of 0.38809 in the local-area mode with an eigenvalue of 0.0689±11.48i, indicating significant contributions to system instability. On the other hand, inter-area modes show weaker participation; for instance, the mode 0.5437±6.13i highlights Sv 19 (transient EMF of d-axis) with a Pf of 0.35494, and Sv 9 with a much lower Pf of 0.06225, indicating lower participation. These results suggest that in the absence of a PSS, rotor angles dominate local modes, while the transient EMF is more important in inter-area modes.

In case of MPA-PSS integration, the system demonstrates improved stability, as indicated by significantly more negative eigenvalues. For instance, in the local-area mode of −9.9167±10.07i, the highest participation factors (Pf) are associated with state variables Sv 20 and Sv 50, with values of 0.21765 and 0.20337, respectively. In the inter-area mode of −19.1284±4.45i, the highest Pf is observed for Sv 45 at 0.24856. Overall, these results highlight the MPA's effectiveness in reducing participation factors across multiple state variables, which contributes to enhanced stability in both local and inter-area modes.

Table III-7: State Variables of the New England Power System.

1:10	Rotor angle “Delta1- Delta10”
11:20	Rotor speed “ω1- ω10”
21:30	the transient EMF of the d-axis "E'_{d1}-E'_{d10}"
31:40	the transient EMF of the q-axis "$E'_{q1} - E'_{q10}$”
41:50	the excitation field voltage “Efd1- Efd10”

Table III-8: Comparative Analysis of Participation Factors for Different PSS Configurations.

NO-PSS

LOCAL-AREA	0.0689428+11.4789i	Sv	10	20	18	8
		Pf	0.38809	0.38809	0.094414	0.094414
	0.14294+9.634i	Sv	5	15	14	4
		Pf	0.30735	0.30735	0.15354	0.15354
	0.12795+9.7149i	Sv	7	17	16	6
		Pf	0.29611	0.29611	0.17349	0.17349
	0.17229+8.378i	Sv	8	18	10	20
		Pf	0.36476	0.36476	0.069302	0.069302
	0.18726+7.9624i	Sv	1	11	13	3
		Pf	0.27277	0.27277	0.22127	0.22127
	0.22607+7.5138i	Sv	4	14	16	6
		Pf	0.179	0.179	0.15751	0.15751
	0.29278-6.6646i	Sv	13	3	11	1
		Pf	0.19364	0.19364	0.15998	0.15998
INTER-AREA	0.54368+6.1262i	Sv	19	9	39	4
		Pf	0.35494	0.35494	0.06225	0.026741
	0.2357+4.0777i	Sv	12	2	6	16
		Pf	0.1811	0.1811	0.053892	0.053892

MPA-PSS

LOCAL-AREA	-9.91671+10.0706i	Sv	20	50	46	40
		Pf	0.21765	0.20337	0.1689	0.15499
	-4.97196+10.807i	Sv	20	19	10	49
		Pf	0.10194	0.10165	0.08498	0.060078
	-1.65452+9.96676i	Sv	11	1	31	41
		Pf	0.21161	0.13561	0.049554	0.041917
	-4.6198+7.5987i	Sv	19	5	15	39

		Pf	0.11239	0.088979	0.073151	0.061498
	-3.8484+6.9004i	Sv	13	3	45	33
		Pf	0.24162	0.22618	0.19841	0.19121
	-19.1284+4.45292i	Sv	45	15	35	31
		Pf	0.24856	0.15429	0.12936	0.12117
	-12.2041+1.1675i	Sv	49	58	44	14
		Pf	0.41238	0.40565	0.39296	0.37756
	-4.5112+5.4946i	Sv	56	50	33	47
		Pf	0.2316	0.22127	0.19022	0.18898
	-6.5706+3.519i	Sv	40	10	46	50
		Pf	0.16992	0.14406	0.13184	0.10963
	-2.0003+3.6783i	Sv	6	46	42	36
		Pf	0.17572	0.11945	0.094745	0.068793
	-0.45834+2.7834i	Sv	12	2	6	44
		Pf	0.22427	0.22427	0.14663	0.084232
	-3.8929+2.1257i	Sv	47	39	9	49
		Pf	0.23118	0.22215	0.19578	0.089836
	-2.0528+1.7668i	Sv	7	37	47	6
		Pf	0.29629	0.204	0.17832	0.06057
	-1.9135+1.0967i	Sv	8	38	49	50
		Pf	0.28553	0.27508	0.24946	0.10532

III.4.4 Hardware in the loop validation

The simulation results of the proposed controllers are tested in this section using real-time digital simulator CU-SLRT Std (DS1104 Equivalent interface+ features) More precisely, a Hardware-in-the-Loop (HIL) simulator was used to verify and validate the previous study about small signal stability analysis for the SMIB system using the proposed PSS controller. The Real-time CU-SLRT board offers the same features as those provided by the DS1104 while the computation capabilities are better and more functions are integrated as it includes 6-core 2.6 GHz processor, FPGA-based I/Os, 16 analog inputs, 8 analog outputs, 16 digital I/O ports, and 16 PWM outputs. Additionally, it has two encoders and

communication interfaces such as Ethernet and RS232 connectors. Figure 17 shows a photograph of the real-time experimental set-up.

Figure III-15: Experimental set-up in Real-time CU-SLRT

Where:

1- Power system model using MATLAB 2018
2- Host real Time CU-SLRT.
3- Second real Time CU-SLRT
4- AVR+PSS Controller model using MATLAB 2020.

Two real-time with same characterization are employed in this setup. The power system, encompassing the generator and network, is first modeled on a personal computer via MATLAB as depicted in Figure III_19 (a). This model is subsequently deployed on the Real-time CU-SLRT (or Host-real time), using Ethernet and RS232 connectors. Inputs and outputs are identified through DAC and ADC respectively, with the input being the output of controller (Vpss) and the output being the rotor speed (ω).

Simultaneously, the AVR+PSS controller is modeled on a separate computer as shown in Figure III_19 (b) and then deployed on a second real-time, also connected via Ethernet and RS232 connectors. Inputs and outputs are identified through DAC and ADC respectively, with the input being the rotor speed (ω) and the output being the output ($V_{pss+avr}$).

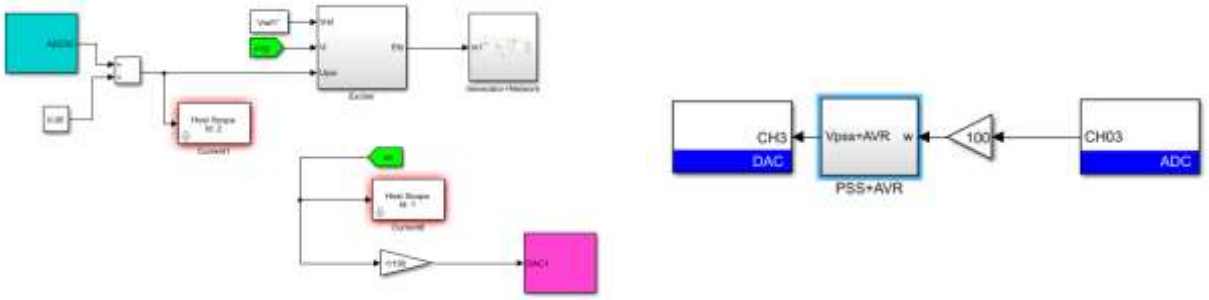

(a) (b)

Figure III-16: Identification of input/output features of: (a)Power system, (b) Power system stabilizer PSS.

In Figure III.19.a, we multiply the speed deviation by a factor of 1/100 before feeding it into the DAC of the host real-time system. This adjustment is necessary because the DAC can only process values ranging from -10 to 10. In our scenario, the rotor speed value is 377 rad/s; hence, we Subsequently, we multiply the speed by 100 before inputting it into the controller to safeguard the real value as shown in Figure III.18.b.

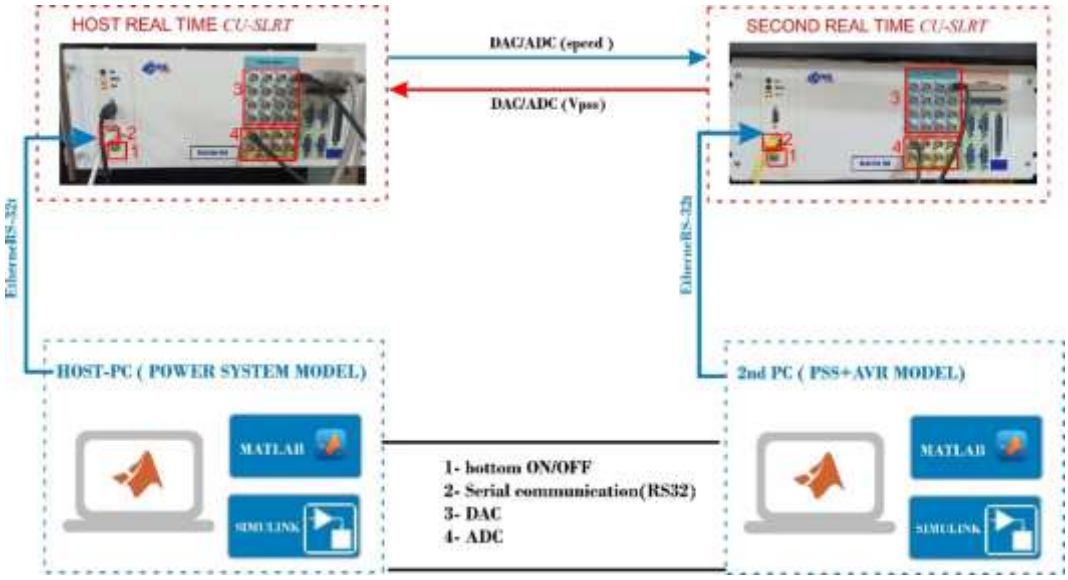

Figure III-17: Schematic diagram of the HIL simulation or the proposed system, with the main components and signals.

In essence, the two real-time systems are interconnected. The Host-real time transmits input features, such as rotor speed 'w', to the second Real-time CU-SLRT which act the controller. Upon receipt of this signal, feedback of the AVR+PSS output controller is sent back to the Host-real time. Finally, the Host-real time receives $V_{pss+avr}$. This entire cycle is

repeated at each sampling interval, Ts. Furthermore, Figure III.21 illustrates the basic components and signal flows of the HIL simulation for the proposed system.

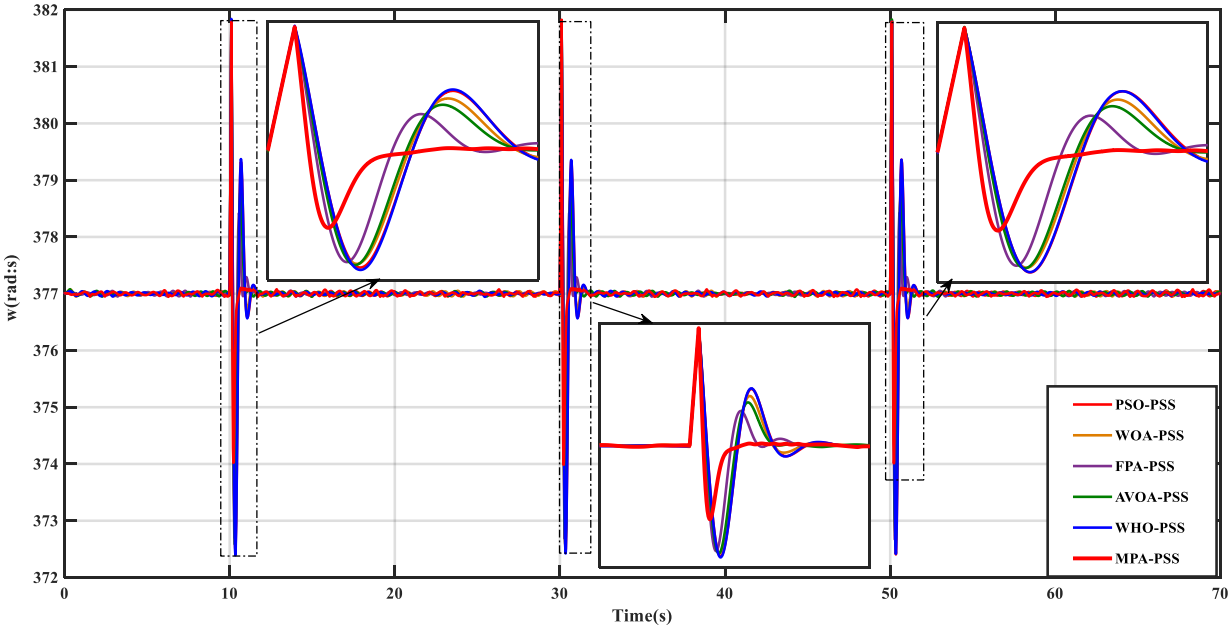

Figure III-18: The rotor Speed for SMIB and its zoom via real time.

The HIL simulation is used to assess the performance of the proposed control schemes in damping of the low frequencies oscillations (LFO). The stability analysis is carried out for the SMIB system using the PSS controller. In Figure 20 LFOs in the angular speed are observed subjected on F1 as cost function. When compared to the PSO, WOA, FPA, AVOA, and WHO-PSS, it is found that the MPA-PSS performs better in terms of reducing the LFOs during three phase symmetrical fault. This results from the PSS's parameters being optimally tuned utilizing the MPA Algorithm.

III.5 Conclusion

A damping controller design for the PSS is employed in this research so as to evaluate the transient stability and mitigate LFOs after fault effectively. Controller design problem is expressed as an optimization problem, and the MPA algorithm is successfully employed to search for the optimal solution of the design problem. The performance of the proposed controller is demonstrated in both a SMIB system and a MMPS comprising the WSCC and New England power systems. through the simulation studies. The time-domain and frequency-domain simulation results reveal the proposed controller's effectiveness and its ability to yield good damping of low frequency oscillations. The system performance

characteristics show that the MPA technique is advantageous over the PSO, WOA, FPA, AVOA and WHO, method in terms its solution quality and stability region. The system performance characteristics regarding settling time indices and eigenvalues plots show that by using the proposed MPA based PSS damping controller, the settling time and power system low frequency oscillations are immensely diminished during major severe disturbances also the eigenvalues are noticeable shifted toward left of the S-plane when compared to other stabilizers in all the cases. The MPA-optimized PSS demonstrates significant improvements, with performance enhancements of up to 98.62% compared to PSO at 69.42%, WOA at 71.79%, FPA at 72.39%, AVOA at 78.04%, and WHO at 68.57%. Validation of the optimal PSS parameters is conducted using CU-SLRT Std, a real-time digital simulator, and Hardware-in-the-loop (HIL) implementation for the SMIB test system, confirming the MPA's superiority.

The most important part in the paper was the HIL validation which the optimized PSS parameters using the MPA have been implemented in real time operation. The successful implementation and obtained performance allow to conclude that the proposed MPA-PSS can be implemented in real power system.

Chapter four

Design of PSS for power system Integrating PV and DGs

CHPITRE FOUR

IV.1 Introduction

In the recent years, the integration of renewable energy resources into the electric networks has become one of the most important and challenging subjects of the power industry. The grid interaction and impact of renewable energy sources have attracted attentions during the past few years. In a proper integration of distributed energy sources, power system stability, control, protection, and operational restrictions should be taken into account. Wind generation plants and solar cells can add a significant uncertainty in the power system load-flow affecting the stability and dynamic behavior. This chapter begins with an introduction to the power system under study, detailing its configurations and highlighting the integration of renewable energy. It then provides an overview of the TID-based PSS and its structure, followed by a brief presentation of the algorithms used in the optimization process. The simulation results are presented, showcasing the application of the TID-based PSS in enhancing power system stability and discussing the performance improvements achieved. Finally, the chapter concludes by summarizing the key findings from the simulation results, emphasizing the contributions of the ZOA-optimized TID to advancing power system stability.

IV.2 Power system tests

The IEEE benchmark power test system, originally Kundur's two-area system, comprises four synchronous generators and eleven buses, with synchronous generator 3 designated as the reference (slack) bus. In this study, the system was modified into a 14-bus network by replacing the fourth generator with a Doubly-Fed Induction Generator (DFIG) and adding a photovoltaic (PV) system at bus 14 as presented in FigureV.1. The bus and line data used for simulations were adopted from Doubly-Fed Induction Generator (DFIG) and adding a photovoltaic (PV) system at bus 14 as presented in FigureIV.1. The bus and line data used for simulations were adopted from

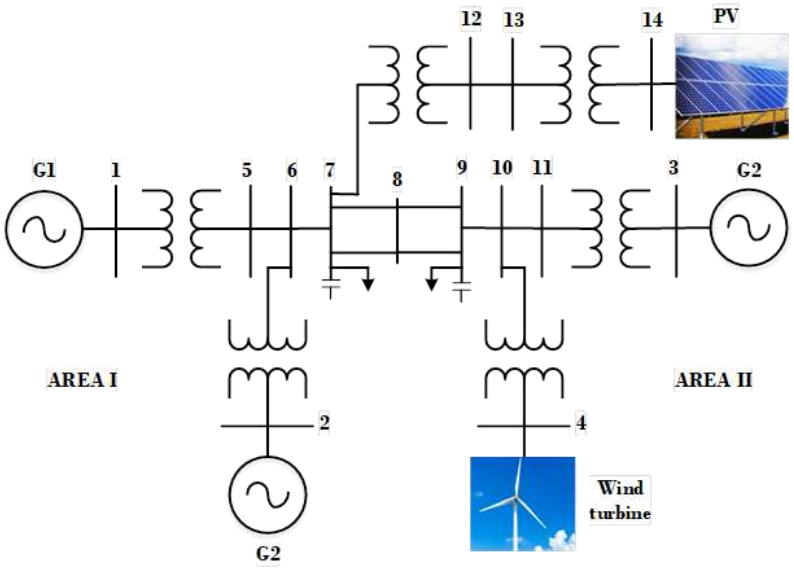

Figure IV-1: structure of modified kundur power system

IV.3 TID based PSS controller

In this study, the proposed TID controller is designed for the LFO issue of modern power systems. The proposed TID controller has the advantage of being simple, ease of use, and the ability to improve the controller's transient response, particularly the overshoot time, without influencing the other parameters. Its transfer function can be expressed as follows:

$$TID = \frac{K_t}{S^{\frac{1}{n}}} + \frac{K_I}{S} + SK_D \qquad (IV.1)$$

where K_I , K_D and K_t express the proportion, integral, and differential tilt gain of the proportional component. These gains can be tuned in the range of [0.1,50]. Whereas the fractional order operator can be tuned in the range of [0, 1].

IV.4 Problem Optimization

IV.4.1 Zebra optimization algorithm

In this study, various metaheuristic algorithms, including Particle Swarm Optimization (PSO), The GOOSE (GOOSE), and Zebra Optimization Algorithm (ZOA), have been employed for tuning system controllers. Each of these algorithms has been explored in detail in previous studies, specifically referenced in [7], [57], and [58], respectively. These

optimization techniques were chosen for their effectiveness in enhancing system stability and minimizing oscillations in renewable energy-integrated power systems.

IV.4.2 Objective function

In order to reduce the error signal, specifically Low-Frequency Oscillations (LFOs), the cost function used in this study is the same adopted in chapter III from [5].

IV.5 Simulation and results

The IEEE benchmark power test system, originally Kundur's two-area system, comprises four synchronous generators and eleven buses, with synchronous generator 3 designated as the reference (slack) bus. In this study, the system was modified into a 14-bus network by replacing the fourth generator with a DFIG and adding a PV system at bus 14. The bus and line data used for simulations were adopted from established sources.

A fault was introduced at bus 8 at 1 second by specifying a large admittance, which led to electromechanical oscillations in the system.

To highlight the influence of renewable energy integration on power system stability, a comparative simulation was performed between the classical and modified Kundur two-area power systems. FigureIV.2 demonstrates the rotor speed deviations for both systems without the incorporation of a PSS. In the classical system, rotor speed oscillations were triggered only after the fault occurred. However, in the modified system with integrated renewable energy sources, oscillations were observed both before and after the fault.

The presence of pre-fault oscillations in the modified system, though smaller than those post-faults, is attributed to the zero inertia characteristic of renewable energy sources like DFIG and PV. This lack of inertia inherently contributes to system instability even under normal, fault-free conditions. These results emphasize the challenges of incorporating renewable energy into conventional power grids, where the absence of mechanical inertia can exacerbate system oscillations, leading to potential stability issues.

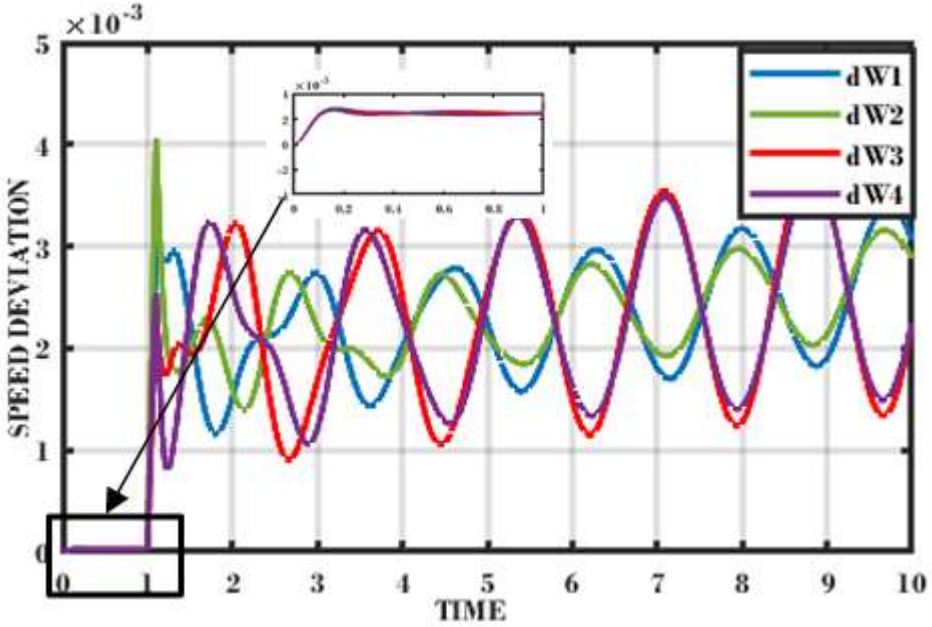

(a)

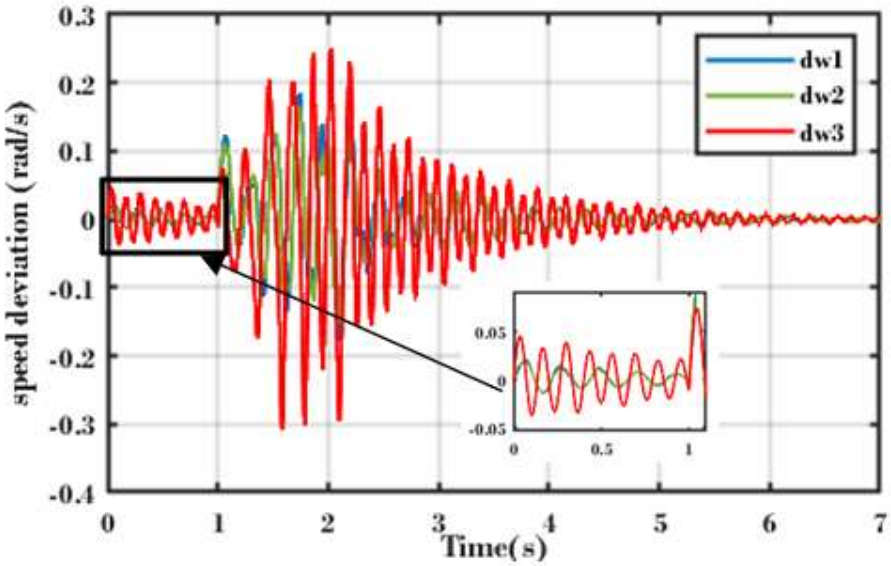

(b)

Figure IIV-2: speed deviation of generators without PSS controller for (a) classic power system, (b) modified power system.

To address the issue of low-frequency oscillations and enhance transient stability, a TID based PSS was incorporated into the system. The parameters of the TID controller were optimized using various metaheuristic algorithms, including Particle PSO, GOOSE, and ZOA. These advanced optimization techniques helped fine-tune the PSS, minimizing oscillations and improving system stability under the influence of renewable energy sources.

It is obvious from FigureIV.3 that the incorporation of TID based PSS enhances the system's damping. Also, it's clear that the TID tuned ZOA offers a minimum settling time compared with TID tuned PSO and GOOSE.

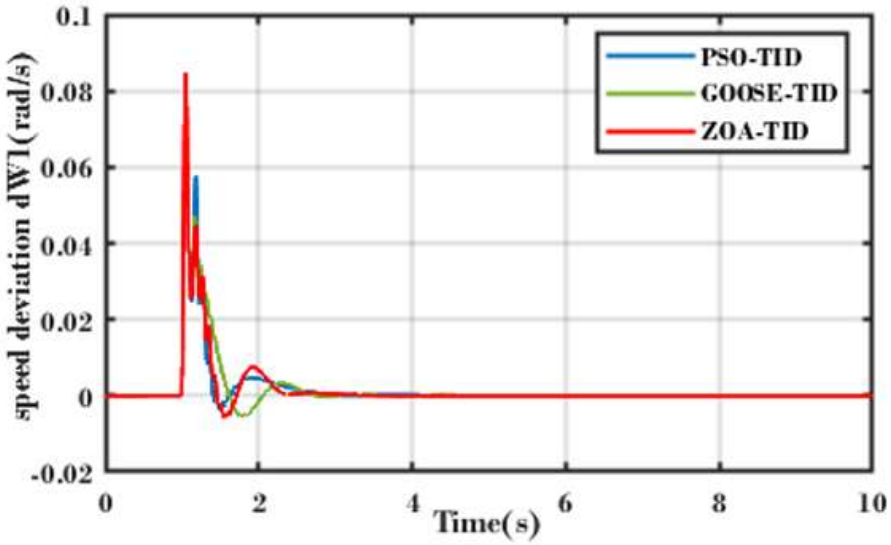

(a)

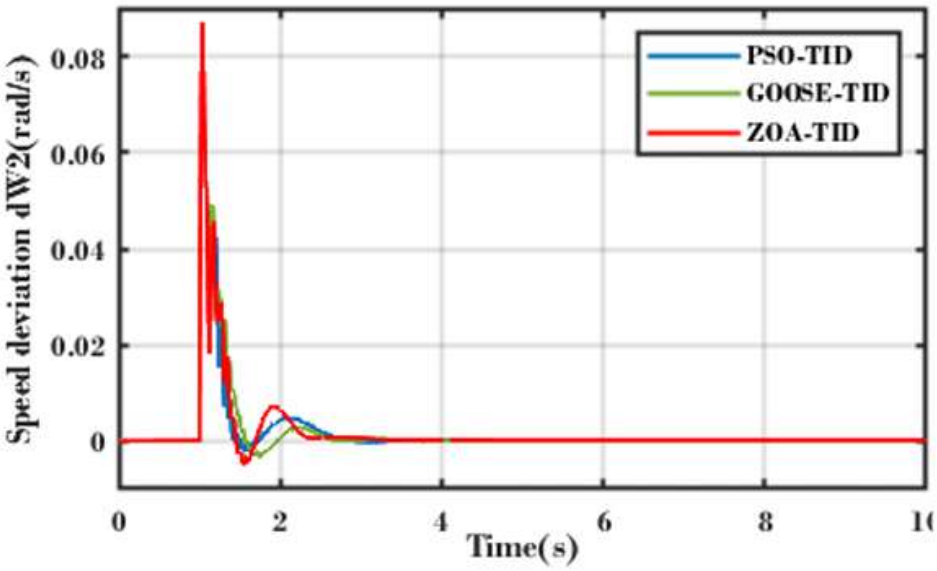

(b)

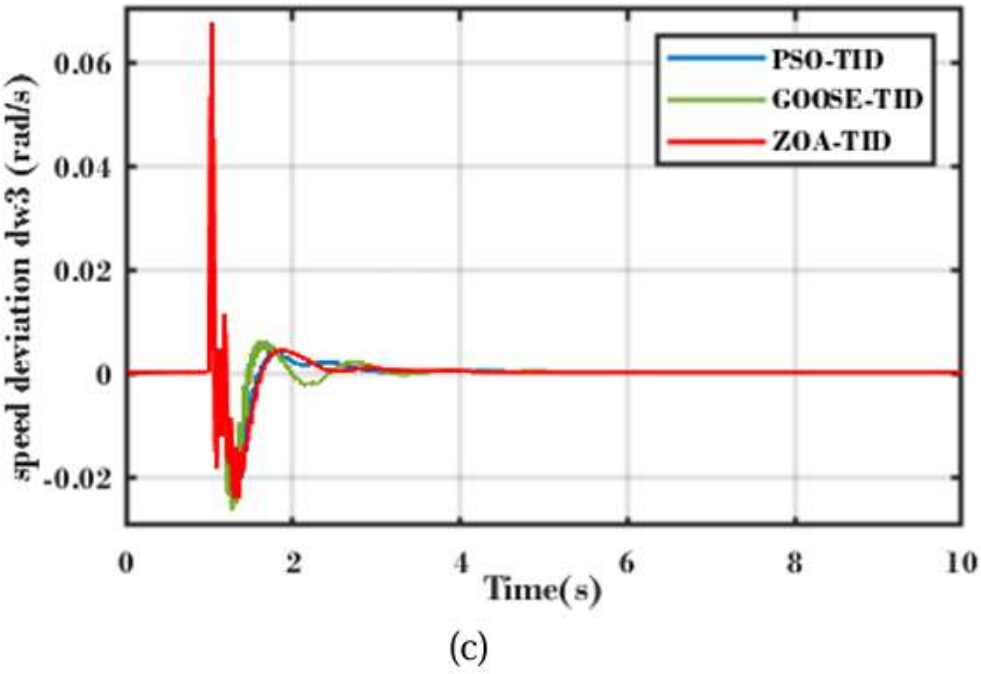

Figure IV-3: Rotor angle deviations of synchronous generators optimized by the PSO, GOOSE and ZOA (a) dw1, (b) dw2 and (c) dw3

IV.6 Conclusion

In conclusion, the integration of renewable energy sources, particularly wind and solar, introduces new challenges to power system stability due to the lack of inertia in these technologies. Through this study, the application of advanced metaheuristic algorithms, such as PSO, GOOSE, and ZOA, for the optimal tuning of TID-based Power System Stabilizers (PSS) has proven effective in damping low-frequency oscillations. Among these methods, ZOA demonstrated superior performance, significantly enhancing overall system stability across various operating conditions. These results emphasize the need for adaptive control strategies in renewable-integrated grids.

General conclusion

General Conclusion

In power systems, maintaining stability has always been a critical challenge due to the complex interactions between various components. To ensure reliable operation, a robust control system is essential. One of the main issues in power systems is stability, particularly under small perturbations. This is where small-signal stability becomes crucial, as it assesses the system's ability to maintain equilibrium under minor disturbances. However, achieving effective control in such scenarios is complicated by the inherent complexity of power systems, where multiple dynamic elements interact. To address these challenges, advanced control strategies are often required, focusing on enhancing system stability and damping oscillations to ensure steady and reliable performance.

In this work, and in order to solve the low frequency oscillation problem discussed in chapter I, an optimization of power system stabilizer and other controllers based on PSS have been applied to power system using the metaheuristic algorithm. The study was done by simulation in the MATLAB/Simulink environment.

This work is summarized in five chapter, it began with a state of art which provides a comprehensive overview of the electrical power system by discussing its various structures. It begins with a detailed explanation of the fundamental components and configurations of power systems. Following this, the concept of power system stability is introduced, along with its main classifications: rotor angle stability, frequency stability, and voltage stability. The chapter concludes with an overview of metaheuristic algorithms, emphasizing their relevance in optimizing power system operations.

In the second chapter, the dynamic modeling of power systems is thoroughly explored. Detailed models of the synchronous generator, excitation system, loads, transmission lines, power system stabilizer (PSS), and double-fed induction motor are presented. Each component's role and behavior within the power system are analyzed to provide a foundational understanding of system dynamics.

The third chapter, focuses on the optimization of PSS parameters using the Marine Predator Algorithm (MPA) in conventional power systems. The study applies the MPA scheme to tune PSS parameters for damping low-frequency oscillations. The performance is tested on the Single Machine Infinite Bus (SMIB) system, the Western System Coordinating Council (WSCC), and the New England 10-machine 39-bus power system. Comparative

analyses with other metaheuristic algorithms, such as Particle Swarm Optimization (PSO), Whale Optimization Algorithm (WOA), Flower Pollination Algorithm (FPA), African Vulture Optimization Algorithm (AVOA), and Wild Horse Optimization (WHO) algorithm, are presented. The MPA-optimized PSS demonstrates significant improvements, with performance enhancements of up to 98.62% compared to PSO at 69.42%, WOA at 71.79%, FPA at 72.39%, AVOA at 78.04%, and WHO at 68.57%. Validation of the optimal PSS parameters is conducted using CU-SLRT Std, a real-time digital simulator, and Hardware-in-the-loop (HIL) implementation for the SMIB test system, confirming the MPA's superiority.

The fourth chapter; delves into the optimization of Fractional order -Takagi-Sugeno fuzzy PID Based on PSS using the modified Dung Beetle Optimization (MDBO) algorithm in conventional power systems. It begins with a system test, followed by a detailed explanation of the proposed controller structures and algorithm. A novel Fractional Order Takagi-Sugeno Fuzzy-Proportional–Integral–Derivative (FO-TSF-PID) controller, tuned using MDBO, is developed to enhance the damping of low-frequency oscillations. The MDBO algorithm optimizes the membership functions (MFs) and gains of the FO-TSF-PID controller, offering a flexible, straightforward, and easily implementable design. The controller's performance is evaluated on a two-area power system and compared to traditional controllers like Lead-Lag PSS, PID, Fractional Order PID (FOPID), and FOFPID, as well as other optimization techniques like PSO, Equilibrium Optimizer (EO), and standard Dung Beetle Optimization (DBO). The MDBO-optimized FO-TSF-PID controller outperforms all others, particularly in reduced settling time, overshoot, and steady-state error, demonstrating its reliability and superiority in power system stabilization.

The last chapter addresses the stability analysis and simulation of power systems with renewable energy integration. The study applies three metaheuristic algorithms—Particle Swarm Optimization (PSO), GOOSE-inspired Optimization Algorithm (GOOSE), and Zebra Optimization Algorithm (ZOA)—for the optimal tuning of tilt-integral-derivative (TID) based PSS parameters in a renewable-integrated multi-machine power system. The results highlight the superior performance of ZOA in enhancing system stability under three-phase symmetrical faults, outperforming both PSO and GOOSE in maintaining system stability.

The simulation results presented in this thesis demonstrate the robust efficiency of various Power System Stabilizers (PSSs) employed in mitigating Low-Frequency Oscillations (LFOs). Additionally, they highlight the superior performance of the metaheuristic algorithms used in the optimization process.

Based on the studies conducted, the optimization techniques utilized in this thesis offer the following advantages:

- The metaheuristic algorithms used provide excellent performance in optimizing Power System Stabilizer (PSS) parameters, leading to improved system stability.
- These algorithms demonstrate robust performance even under varying and severe fault conditions, ensuring consistent damping of low-frequency oscillations.
- The optimization methods can be applied to various power system configurations, from single machine infinite bus systems to complex multi-machine systems.
- The optimized controllers significantly reduce settling time, overshoot, and steady-state error, contributing to overall system stability and reliability.

Despite these advantages, the optimization process has some limitations:

- The optimization process, particularly for large-scale systems, requires significant computational time during the offline phase, which can be resource-intensive.
- The performance of the optimization is influenced by the quality of initial parameters, necessitating careful selection and tuning.
- Implementing these advanced optimization algorithms requires a deep understanding of both the algorithmic processes and the system dynamics, which can pose challenges in practical applications.

As a continuation of this work, the following future directions are proposed:

- Efforts will be made to enhance the efficiency of the optimization algorithms, focusing on reducing the time required for the offline optimization process.
- Further research will explore the application of these optimization techniques to systems with high penetration of renewable energy sources, ensuring stability and performance under varying conditions.

- Combining metaheuristic algorithms with other optimization methods or machine learning approaches could further enhance performance and reduce computational overhead.
- The optimized control strategies will be implemented and tested on Field-Programmable Gate Array (FPGA) platforms for real-time experimental validation, ensuring practical applicability and reliability.

References

References:

[1] « Power System Stability and Control ».

[2] F. P. Demello et C. Concordia, « Concepts of synchronous machine stability as affected by excitation control », *IEEE Trans. Power Appar. Syst.*, vol. 88, nº 4, p. 316-329, 1969.

[3] P. Kundur *et al.*, « Definition and classification of power system stability IEEE/CIGRE joint task force on stability terms and definitions », *IEEE Trans. Power Syst.*, vol. 19, nº 3, p. 1387-1401, 2004.

[4] M. Ahmadi Kamarposhti, H. Shokouhandeh, Y. Gholami Omali, I. Colak, P. Thounthong, et W. Holderbaum, « Optimal Coordination of TCSC and PSS2B Controllers in Electric Power Systems Using MOPSO Multiobjective Algorithm », *Int. Trans. Electr. Energy Syst.*, vol. 2022, p. 5233620, nov. 2022, doi: 10.1155/2022/5233620.

[5] P. K. Ray *et al.*, « A Hybrid Firefly-Swarm Optimized Fractional Order Interval Type-2 Fuzzy PID-PSS for Transient Stability Improvement », *IEEE Trans. Ind. Appl.*, vol. 55, nº 6, p. 6486-6498, nov. 2019, doi: 10.1109/TIA.2019.2938473.

[6] A. Safari, « A PSO procedure for a coordinated tuning of power system stabilizers for multiple operating conditions », *J. Appl. Res. Technol.*, vol. 11, nº 5, p. 665-673, 2013.

[7] B. Dasu, M. S. Kumar, et R. S. Rao, « Design of robust modified power system stabilizer for dynamic stability improvement using Particle Swarm Optimization technique », *Ain Shams Eng. J.*, vol. 10, nº 4, p. 769-783, 2019.

[8] H. Mustapha, M. Buhari, et A. S. Ahmad, « An improved genetic algorithm based power system stabilizer for power system stabilization », in *2019 IEEE AFRICON*, IEEE, 2019, p. 1-5.

[9] T. Guesmi, A. Farah, H. H. Abdallah, et A. Ouali, « Robust design of multimachine power system stabilizers based on improved non-dominated sorting genetic algorithms », *Electr. Eng.*, vol. 100, p. 1351-1363, 2018.

[10] H. Shayeghi, H. A. Shayanfar, S. Asefi, et A. Younesi, « Optimal Tuning and comparison of different Power system stabilizers using different performance indices Via Jaya Algorithm », in *Proceedings of the International Conference on Scientific Computing (CSC)*, The Steering Committee of The World Congress in Computer Science, Computer …, 2016, p. 34.

[11] H. Shayeghi, S. Asefi, et A. Younesi, « Tuning and comparing different power system stabilizers using different performance indices applying GWO algorithm », in *Proceedings of the International Comprehensive Competition Conference on Engineering Sciences, Iran, Anzali*, 2016.

[12] S. Gurung, F. Jurado, S. Naetiladdanon, et A. Sangswang, « Comparative analysis of probabilistic and deterministic approach to tune the power system stabilizers using the directional bat algorithm to improve system small-signal stability », *Electr. Power Syst. Res.*, vol. 181, p. 106176, 2020.

[13] A. Sabo, N. I. Abdul Wahab, M. L. Othman, M. Z. A. Mohd Jaffar, et H. Beiranvand, « Optimal design of power system stabilizer for multimachine power system using farmland fertility algorithm », *Int. Trans. Electr. Energy Syst.*, vol. 30, nº 12, p. e12657, 2020.

[14] B. Abdollahzadeh, F. S. Gharehchopogh, et S. Mirjalili, « African vultures optimization algorithm: A new nature-inspired metaheuristic algorithm for global optimization problems », *Comput. Ind. Eng.*, vol. 158, p. 107408, 2021.

[15] S. Ekinci et B. Hekimoglu, « Parameter optimization of power system stabilizer via salp swarm algorithm », in *2018 5th international conference on electrical and electronic engineering (ICEEE)*, IEEE, 2018, p. 143-147.

[16] S. Ekinci, A. Demiroren, et B. Hekimoglu, « Parameter optimization of power system stabilizers via kidney-inspired algorithm », *Trans. Inst. Meas. Control*, vol. 41, nº 5, p. 1405-1417, 2019.

[17] B. Dasu, M. Sivakumar, et R. Srinivasarao, « Interconnected multi-machine power system stabilizer design using whale optimization algorithm », *Prot. Control Mod. Power Syst.*, vol. 4, p. 1-11, 2019.

[18] D. Chitara, K. R. Niazi, A. Swarnkar, et N. Gupta, « Cuckoo search optimization algorithm for designing of a multimachine power system stabilizer », *IEEE Trans. Ind. Appl.*, vol. 54, nº 4, p. 3056-3065, 2018.

[19] S. Ekinci, D. İzci, et B. Hekimoglu, « Implementing the Henry gas solubility optimization algorithm for optimal power system stabilizer design », *Electrica*, vol. 21, nº 2, p. 250-258, 2021.

[20] P. Dey, A. Bhattacharya, et P. Das, « Tuning of power system stabilizer for small signal stability improvement of interconnected power system », *Appl. Comput. Inform.*, vol. 16, nº 1/2, p. 3-28, 2017.

[21] S. Ekinci, D. Izci, H. L. Zeynelgil, et S. Orenc, « An application of slime mould algorithm for optimizing parameters of power system stabilizer », in *2020 4th international symposium on multidisciplinary studies and innovative technologies (ISMSIT)*, IEEE, 2020, p. 1-5.

[22] I. M. Alotaibi, S. Ibrir, M. A. Abido, et M. Khalid, « Nonlinear Power System Stabilizer Design for Small Signal Stability Enhancement », *Arab. J. Sci. Eng.*, vol. 47, nº 11, p. 13893-13905, 2022.

[23] H. Yokus et A. Ozturk, « A robust crow search algorithm-based power system stabilizer for the SMIB system », *Neural Comput. Appl.*, vol. 34, nº 11, p. 9161-9173, 2022.

[24] J. Ansari, A. R. Abbasi, M. H. Heydari, et Z. Avazzadeh, « Simultaneous design of fuzzy PSS and fuzzy STATCOM controllers for power system stability enhancement », *Alex. Eng. J.*, vol. 61, nº 4, p. 2841-2850, avr. 2022, doi: 10.1016/j.aej.2021.08.007.

[25] R. Hemmati, « Power system stabilizer design based on optimal model reference adaptive system », *Ain Shams Eng. J.*, vol. 9, nº 2, p. 311-318, 2018.

[26] M. A. El-Dabah, S. Kamel, M. A. Y. Abido, et B. Khan, « Optimal tuning of fractional-order proportional, integral, derivative and tilt-integral-derivative based power system stabilizers using Runge Kutta optimizer », *Eng. Rep.*, vol. 4, nº 6, p. e12492, 2022.

[27] R. Saralegui, A. Sanchez, et A. de Castro, « Modeling of deadtime events in power converters with half-bridge modules for a highly accurate hardware-in-the-loop fixed point implementation in fpga », *Appl. Sci.*, vol. 11, nº 14, p. 6490, 2021.

[28] P. Kundur, « Power system stability », *Power Syst. Stab. Control*, vol. 10, p. 7-1, 2007.

[29] J. H. Chow et J. J. Sanchez-Gasca, *Power system modeling, computation, and control*. John Wiley & Sons, 2020.

[30] M. Brucoli, F. Rossi, F. Torelli, et M. Trovato, « A generalized approach to the analysis of voltage stability in electric power systems », *Electr. Power Syst. Res.*, vol. 9, nº 1, p. 49-62, 1985.

[31] Z. Y. J. Dong *et al.*, « Assessing Short-Term Voltage Stability of Electric Power Systems by a Hierarchical Intelligent System », 2016.

[32] C. Zhao, U. Topcu, N. Li, et S. Low, « Design and stability of load-side primary frequency control in power systems », *IEEE Trans. Autom. Control*, vol. 59, nº 5, p. 1177-1189, 2014.

[33] M. Gu, L. Meegahapola, et K. L. Wong, « Review of rotor angle stability in hybrid AC/DC power systems », in *2018 IEEE PES Asia-Pacific Power and Energy Engineering Conference (APPEEC)*, IEEE, 2018, p. 7-12.

[34] N. G. Hingorani et L. Gyugyi, *Understanding FACTS: concepts and technology of flexible AC transmission systems*. Wiley-IEEE Press, 2000.

[35] Y.-H. Song et A. T. Johns, *Flexible ac transmission systems (FACTS)*, nº 30. IET, 1999.

[36] L. Kunjumuhammed, S. Kuenzel, et B. Pal, *Simulation of power system with renewables*, 1re éd. San Diego: Academic press is an imprint of Elsevier, 2019.

[37] K. Prasertwong, N. Mithulananthan, et D. Thakur, « Understanding low-frequency oscillation in power systems », *Int. J. Electr. Eng. Educ.*, vol. 47, nº 3, p. 248-262, 2010.

[38] Z. A. Obaid, L. M. Cipcigan, et M. T. Muhssin, « Power system oscillations and control: Classifications and PSSs' design methods: A review », *Renew. Sustain. Energy Rev.*, vol. 79, p. 839-849, 2017.

[39] M. A. Abido, « A novel approach to conventional power system stabilizer design using tabu search », *Int. J. Electr. Power Energy Syst.*, vol. 21, nº 6, p. 443-454, 1999.

[40] P. Hoang et K. Tomsovic, « Design and analysis of an adaptive fuzzy power system stabilizer », *IEEE Trans. Energy Convers.*, vol. 11, nº 2, p. 455-461, 1996.

[41] F. R. Schleif, H. D. Hunkins, E. E. Hattan, et W. B. Gish, « Control of rotating exciters for power system damping: Pilot applications and experience », *IEEE Trans. Power Appar. Syst.*, nº 8, p. 1259-1266, 1969.

[42] Ĭ. Eke, M. C. Taplamacıoğlu, et K. Y. Lee, « Robust tuning of power system stabilizer by using orthogonal learning artificial bee colony », *IFAC-Pap.*, vol. 48, nº 30, p. 149-154, 2015.

[43] P. W. Sauer et M. A. Pai, « POWER SYSTEM DYNAMICS AND STABILITY ».

[44] P. Kundur, « Power system stability », *Power Syst. Stab. Control*, vol. 10, p. 7-1, 2007.

[45] A. A. Sallam et O. P. Malik, « Power system stability: modelling, analysis and control », IET, 2015.
[46] A. Arif, Z. Wang, J. Wang, B. Mather, H. Bashualdo, et D. Zhao, « Load modeling—A review », *IEEE Trans. Smart Grid*, vol. 9, nº 6, p. 5986-5999, 2017.
[47] E. V. Larsen et D. A. Swann, « Applying power system stabilizers Part III: Practical considerations », *IEEE Trans. Power Appar. Syst.*, nº 6, p. 3034-3046, 1981.
[48] H. Xia, S. Zhang, R. Jia, H. Qiu, et S. Xu, « Blade shape optimization of Savonius wind turbine using radial based function model and marine predator algorithm », *Energy Rep.*, vol. 8, p. 12366-12378, nov. 2022, doi: 10.1016/j.egyr.2022.09.062.
[49] A. Jia, H. Liu, Y. Yun, R. Jiang, et S. Pouramini, « Energy efficiency measures in existing buildings by a multiple-objective optimization with a solar panel system using Marine Predators Optimization Algorithm », *Sol. Energy*, vol. 267, p. 112208, 2024.
[50] H. Naseri, A. Golroo, M. Shokoohi, et A. H. Gandomi, « Sustainable pavement maintenance and rehabilitation planning using the marine predator optimization algorithm », *Struct. Infrastruct. Eng.*, vol. 20, nº 3, p. 340-352, 2024.
[51] A. Eid, S. Kamel, et L. Abualigah, « Marine predators algorithm for optimal allocation of active and reactive power resources in distribution networks », *Neural Comput. Appl.*, vol. 33, nº 21, p. 14327-14355, 2021.
[52] A. Faramarzi, M. Heidarinejad, S. Mirjalili, et A. H. Gandomi, « Marine Predators Algorithm: A nature-inspired metaheuristic », *Expert Syst. Appl.*, vol. 152, p. 113377, 2020.
[53] H. Beiranvand et E. Rokrok, « General relativity search algorithm: a global optimization approach », *Int. J. Comput. Intell. Appl.*, vol. 14, nº 03, p. 1550017, 2015.
[54] I. Podlubny, « Fractional-order systems and fractional-order controllers », *Inst. Exp. Phys. Slovak Acad. Sci. Kosice*, vol. 12, nº 3, p. 1-18, 1994.
[55] S. Das, I. Pan, et S. Das, « Performance comparison of optimal fractional order hybrid fuzzy PID controllers for handling oscillatory fractional order processes with dead time », *ISA Trans.*, vol. 52, nº 4, p. 550-566, 2013.
[56] J. Xue et B. Shen, « Dung beetle optimizer: a new meta-heuristic algorithm for global optimization », *J. Supercomput.*, vol. 79, nº 7, p. 7305-7336, mai 2023, doi: 10.1007/s11227-022-04959-6.
[57] R. K. Hamad et T. A. Rashid, « GOOSE Algorithm: A Powerful Optimization Tool for Real-World Engineering Challenges and Beyond ».
[58] E. Trojovska, M. Dehghani, et P. Trojovsky, « Zebra Optimization Algorithm: A New Bio-Inspired Optimization Algorithm for Solving Optimization Algorithm », *IEEE Access*, vol. 10, p. 49445-49473, 2022, doi: 10.1109/access.2022.3172789.

Appendices

APPENDIX A: BENSHMARK POWER SYSTEMS'S SIMULINK MODEL AND PARAMETERS OF 3ed CHAPTER

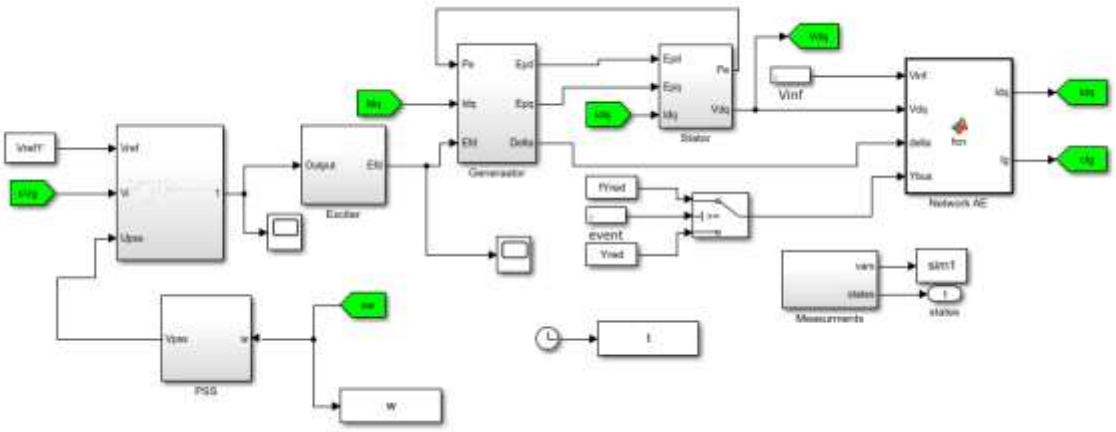

(a)

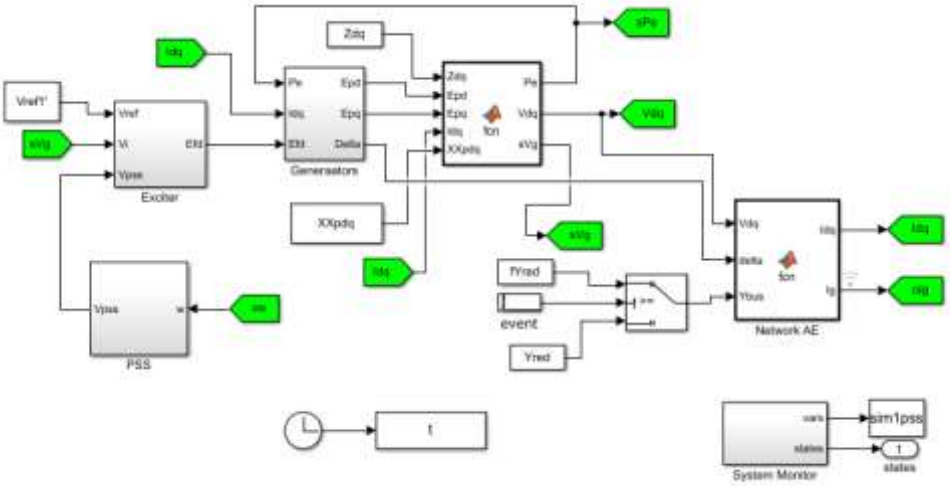

(b)

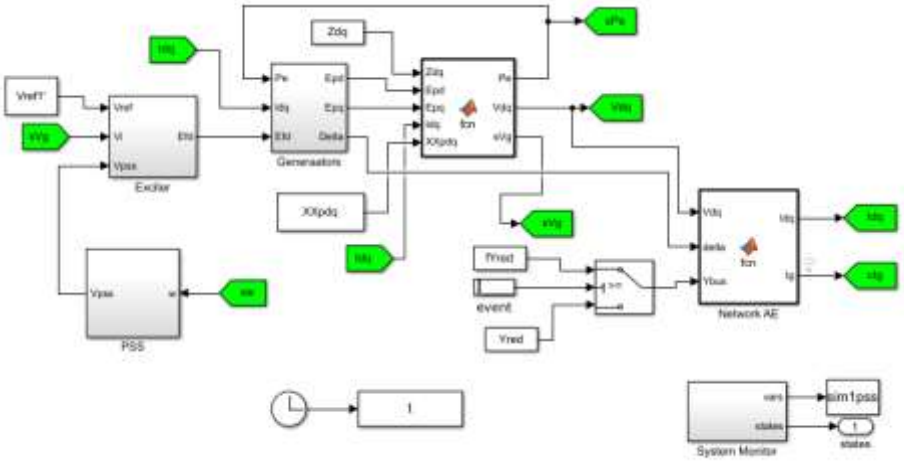

(c)

Figure A- 1 : Simulink model of (a) SMIB power system; (b) WSCC power system and (c)

Table A- 1 : Simulation parameters for (a) machine parameters (b) Excitation system (c) Transmission line for SMIB (d) operating point information

(a)

Parameter	Name	Value
H	generator inertia constant	6.4
D	damping coefficient	0.0
T'_{d0}	d-axis and q-axis open-circuit time constants	6.0
T'_{q0}		0.535s
X_d	the synchronous transient of d-axis and q-axis reactances	0.8958
X_q		0.8645
X'_d	the synchronous sub-transient of d-axis and q-axis reactances	0.1198
X'_q		0.1969

(b)

Parameter	Name	Value
K_A	excitation static gain	50.0
T_A	the regulator time constant	0.05s

(c)

Parameter	Name	Value
X_T	the transmission line reactance	0.0625
X_L	is the inductance of the transmission line	0.2pu

(d)

Parameter	Name	Value
P_g	power output	1.63pu

V_1	the terminal voltage	1.026pu
V_2	Reference voltage	1.025pu

Table A- 2 : Parameter setting for the optimization algorithms using in chapter III

Parameters	Value
Population	40
Max Iteration	100

Appendix B: Benshmark power systems's Simulink model and Matlab code of 4TH CHAPTER

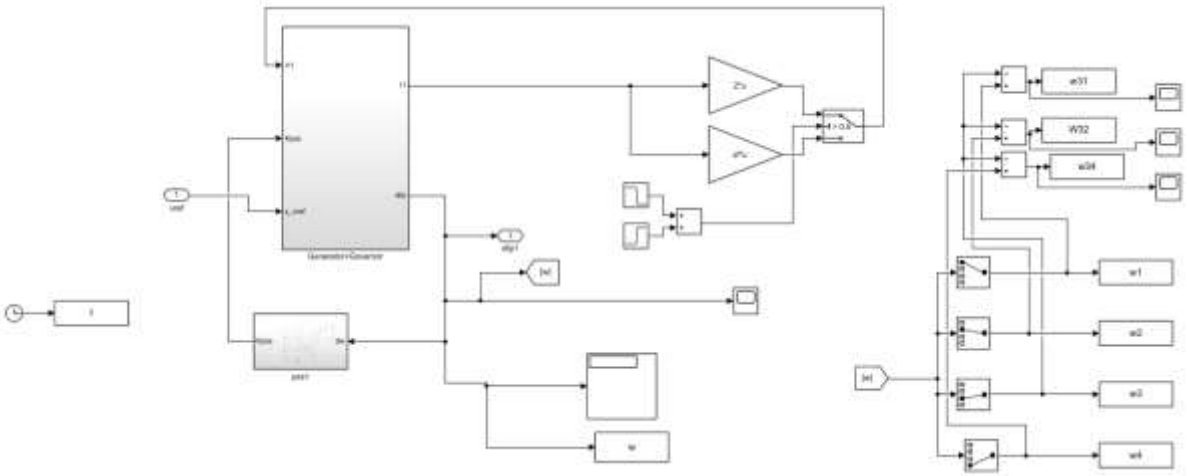

(a)

'b)

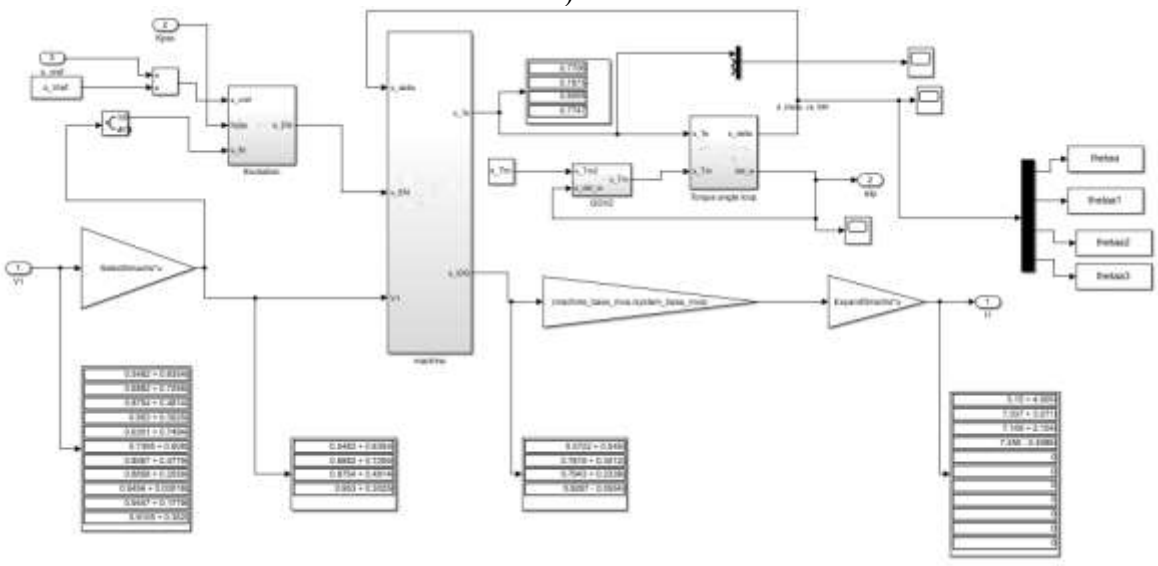

(b)

Figure B- 2 : Simulink model of (a) Two-area 4 machines power system; (b) Generator+ Governor

```
%machine_numb;machine_base_mva;Armature leakage ;reactance ARMATURE
%RESISTANCE d axis synchronous reactance; d axis transient reactance;
%d axis sub-transient reactance; d axis open circuit transient TIME
%constant;d axis open circuit sub_transient TIME constant;q axis
%synchronous reactance ;q axis transient reactance; q axis sub-transient reactance;
%q axis open circuit transient TIME constant,q axis open circuit sub_transient TIME constant;
%INERTIA CONSTANT ;Self damping
mac_con =[
1 900 0.2 0.0025 1.8 0.3 0.25 8 0.03 1.7 0.55 0.25 0.4 0.05 6.5 0;
2 900 0.2 0.0025 1.8 0.3 0.25 8 0.03 1.7 0.55 0.25 0.4 0.05 6.5 0;
3 900 0.2 0.0025 1.8 0.3 0.25 8 0.03 1.7 0.55 0.25 0.4 0.05 6.5 0;
4 900 0.2 0.0025 1.8 0.3 0.25 8 0.03 1.7 0.55 0.25 0.4 0.05 6.5 0];
```

(a)

```
%four_mac_data.m % bus No., Voltage Mag., Voltage Angle, Pgen,
Qgen, Pload, Qload, Pshunt, % Qshunt, bus type
bus = [...
1 1.00    00.0   7.000    0.00 0.0000   0.000    0.00   0.00 2;
2 1.00    00.0   7.000    0.00 0.0000   0.000    0.00   0.00 2;
3 1.00    00.0   0.0000   0.00 0.0000   0.000    0.00   0.00 1;
4 1.00    00.0   7.0000   0.00 0.0000   0.000    0.00   0.00 2;
5 1.00    00.0   0.0000   0.00 0.0000   0.000    0.00   0.00 3;
6 1.00    00.0   0.0000   0.00 0.0000   0.000    0.00   0.00 3;
7 1.00    00.0   0.0000   0.00 9.6700   1.000    0.00   2.00 3;
8 1.00    00.0   0.0000   0.00 0.0000   0.000    0.00   0.00 3;
9 1.00    00.0   0.0000   0.00 17.670   1.000    0.00   3.50 3;
10 1.00   00.0   0.0000   0.00 0.0000   0.000    0.00   0.00 3;
11 1.00   00.0   0.0000   0.00 0.0000   0.000    0.00   0.00 3];

%from bus, To bus, Resistant, Inductance, Capacitance, tap-ratio,
tap-phase
line = [01 05 0.0000 0.0167 0.00000 1.0 0.0;
        02 06 0.0000 0.0167 0.00000 1.0 0.0;
        03 11 0.0000 0.0167 0.00000 1.0 0.0;
        04 10 0.0000 0.0167 0.00000 1.0 0.0;
        05 06 0.0025 0.0250 0.04375 1.0 0.0;
        10 11 0.0025 0.0250 0.04375 1.0 0.0;
        06 07 0.0010 0.0100 0.01750 1.0 0.0;
        09 10 0.0010 0.0100 0.01750 1.0 0.0;
        07 08 0.0110 0.1100 0.19250 1.0 0.0;
        07 08 0.0110 0.1100 0.19250 1.0 0.0;
        08 09 0.0110 0.1100 0.19250 1.0 0.0;
        08 09 0.0110 0.1100 0.19250 1.0 0.0];
```

(b)

```
% ************************ EXCITATION SYSTEM DATA ******************
s_Ka=200;%Static excitation gain Padiyar p.328
s_Ta=0.02;%Static excitation time constant Padiyar p.328

% **** Governor Control SYSTEM DATA - not used *********
s_Tg=0.2;%Kundur p.598
s_Rgov=0.05;%Kundur p.598%governor control system data
```

(c)

Script B- 1 : Matlab script of (a) machine parameters ; (b) bus data (c) excitation and governor parameters

Table B- 1 : Parameter setting for the optimization algorithms using in chapter IV

Parameters	Value
Population	25
Max Iteration	100

Appendix C: Benshmark power system's Simulink model and parameters of 4th Chapter

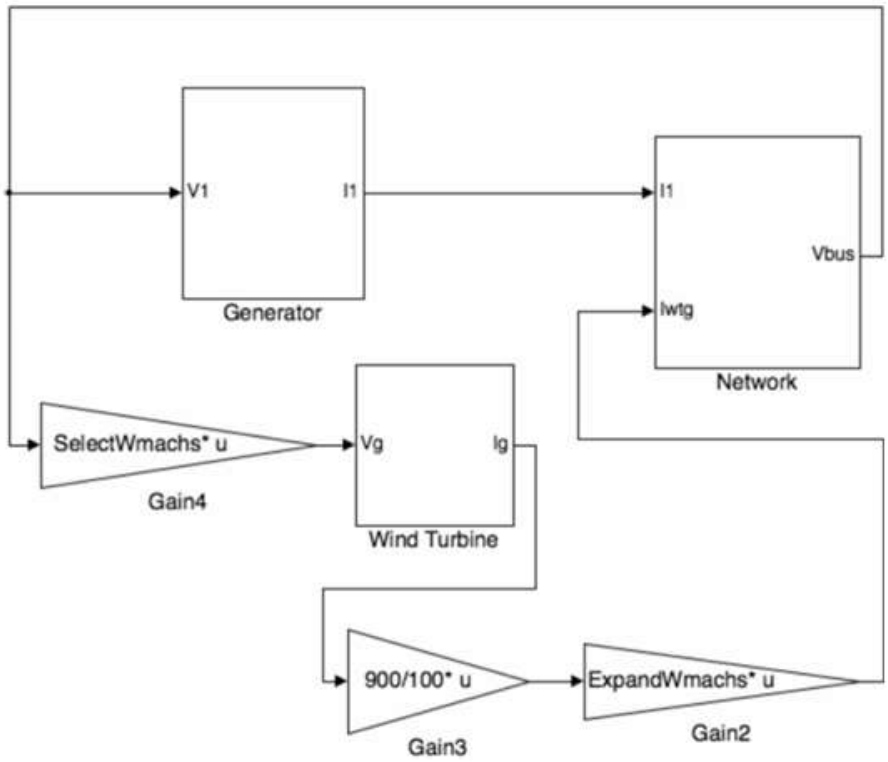

(a)

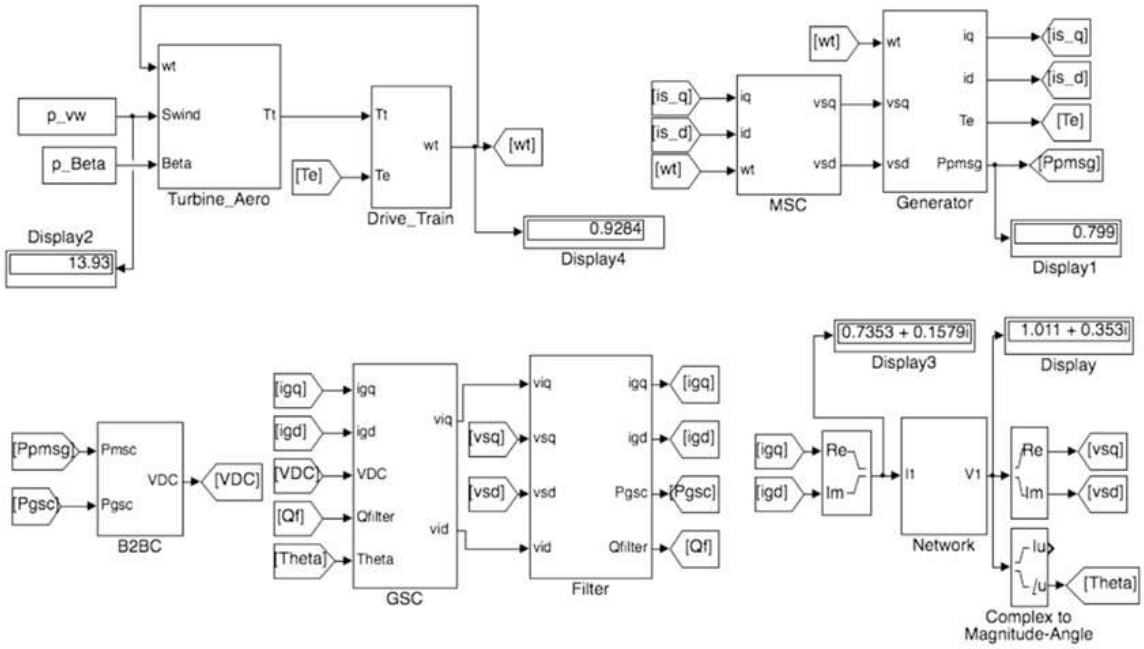

(b)

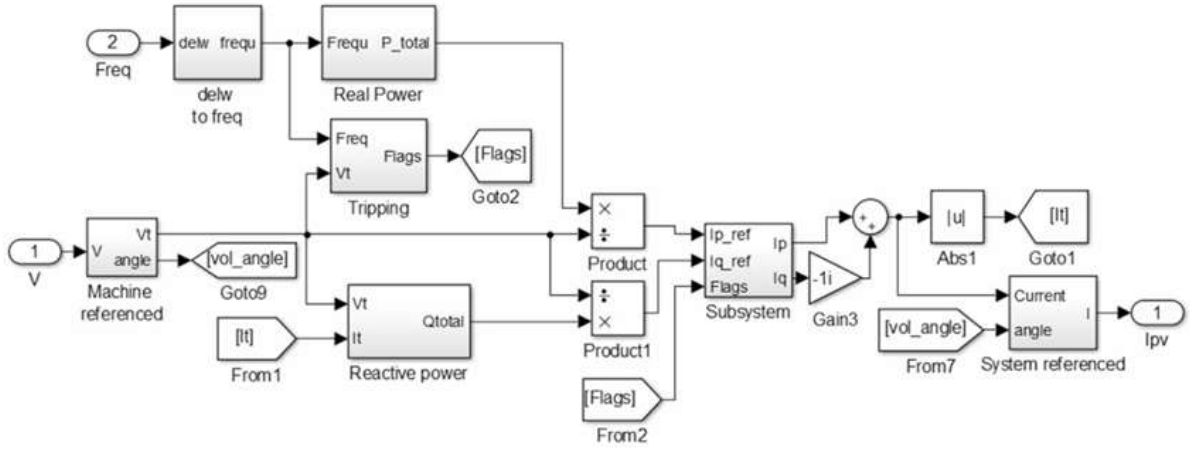

(c)

Figure C- 3 : Simulink model of (a) modified Two-area 4 machines power system; (b) DFIG (c) PV